Microgel Characterization Across Interfaces: From Adsorption on Solid Interfaces to Cellular Uptake

Mikrogel-Charakterisierung an Grenzflächen: Von der Adsorption an festen Grenzflächen zur zellulären Aufnahme

Von der Fakultät für Mathematik und Naturwissenschaften
der RWTH Aachen University zur Erlangung des akademischen Grades
eines Doktors der Naturwissenschaften genehmigte Dissertation

vorgelegt von

Andrey Babenyshev, M.Sc.

aus
Moskau, Russland

Berichter: Univ.-Prof. Dr. rer. nat. Walter Richtering
Univ.-Prof. Dr. rer. nat. Jérôme Crassous

Tag der mündlichen Prüfung: 12. Februar 2026

"Theory is a good thing but a good experiment lasts forever".

Pyotr Kapitsa

Declaration of Authorship

Some chapters in this dissertation were submitted previously. In the following, the contributions of the presented results of all chapters are listed:

Chapter 2 is adapted from three papers, where I performed the AFM experiments and the analysis. The whole chapter is written by me and mostly focuses on my contributions to these works.

Subsection 2.3.1 is based on Hazra, N., Lammertz, J., **Babenyshev, A.**, Erkes, R., Hagemans, F., Misra, C., Richtering, W., and Crassous, J. J. (2024a). Charged hollow microgel capsules. Soft Matter, 20(23):4608–4620.

The microgels were synthesized by Janik Lammertz under the supervision of Fabian Hagemans and Nabanita Hazra. I performed AFM experiments and analysis of core-shell and hollow "neutral" and "charged" microgels. I also made spinning disk microscopy measurements of core-shell microgels. I revised the manuscript together with all authors.

Subsection 2.3.2 is based on Hagemans, F., Hazra, N., Lovasz, V. D., Awad, A. J., Frenken, M., **Babenyshev, A.**, Laukkanen, O.-V., Braunmiller, D., Richtering, W., and Crassous, J. J. (2025). Soft and deformable thermoresponsive hollow rod-shaped microgels. Small, 21(1):2401376.

Synthesis of the microgels and their characterization by static and dynamic light scattering experiments were performed by Fabian Hagemans and Nabanita Hazra. I performed AFM experiments and analysis of core-shell and hollow rod-shaped microgels. I revised the manuscript together with all authors during the final submission.

Subsection 2.3.3 is based on Hazra, N., Rudov, A. A., Midya, J., **Babenyshev, A.**, Bochenek, S., Frenken, M., Richtering, W., Gompper, G., Auth, T., Potemkin, I. I., et al. (2024b). Capillary-driven self-assembly of soft ellipsoidal microgels at the air–water interface. Proceedings of the National Academy of Sciences, 121(52):e2403690121.

Nabanita Hazra performed dip-coating deposition, while I performed AFM experiments of ellipsoidal microgels and analysis of their stiffness tomography (force spectroscopy data). I revised the manuscript together with all authors.

Chapter 3 is based on the project "Contact mechanics of microgels adsorption" supervised by Prof. Crassous. Experiments are ongoing.

I continued the experiments of Katja Northdurft, she synthesized microgels by microfluidics and performed osmotic pressure experiments. Hollow microgels were synthesized by Nabanita Hazra and Fabian Hagemans. Small PNIPAM microgels were synthesized by Steffen Bochenek. I performed spinning disk and AFM microscopy experiments and the analysis of the data. The whole chapter is written by me.

Chapter 4 is based on **Babenyshev, A.**, Switacz, V. K., Spehr, M., and Richtering, W. (2025). Size and softness synergy in cellular microgel uptake: a force spectroscopy study. Nanoscale.

Prof. Walter Richtering and I designed the study. I performed all sample preparation for AFM experiments and the following force spectroscopy study and analysis. Together with Victoria Switacz, we performed cell experiments. Large ULC microgels were synthesized by Alan Francisco. I co-wrote the first draft of the manuscript.

Chapter 5 is based on Switacz, V. K., **Babenyshev, A.**, Spehr, M., and Richtering, W. Post-Endocytotic Effects of Microgel Internalization. Manuscript in preparation.

Victoria Switacz and I, with supervision from Prof. Spehr and Prof. Richtering, designed the study. Victoria Switacz and I performed cell experiments. Victoria Switacz analyzed the data. I wrote the entire chapter.

Andrey Babenyshev, M.Sc.
February 2026

Acknowledgements

The completion of this thesis would not have been possible without the invaluable support, guidance, and encouragement of many remarkable individuals. I am deeply grateful to all those who have contributed to this journey and helped shape both my research and personal growth.

First and foremost, I would like to express my sincere gratitude to Prof. Walter Richtering and Prof. Jérôme Crassous for their exceptional supervision and unwavering support throughout this work. Their profound expertise and insightful guidance have been instrumental in my development as a researcher, and I have learned immensely from their knowledge and experience in this field.

I extend my heartfelt thanks to the AFM team of our group, who welcomed me into the fascinating—albeit sometimes challenging—world of force measurements. Special appreciation goes to Friederike Schulte and Simon Schong, who patiently introduced me to AFM techniques and helped me navigate this complex but rewarding field. I am also grateful to Timon Kratzenberg for his thoughtful questions and engaging scientific discussions that enriched my understanding. Last but certainly not least, I want to acknowledge Tamás Haraszti for essential technical support and maintenance of AFM device in DWI.

My sincere appreciation extends to all members of the Richtering group, whose camaraderie and collegiality made this research journey not only productive but genuinely enjoyable. Special thanks go to Anish Gulati, Alexander Petrunin, Nabanita Hazra, Tom Höfken, Dominik Braunmiller, Evdokia Stefanopoulou, and Patrick Denk. The fun we shared together made this demanding journey significantly less stressful and far more memorable.

I am grateful to the Chemosensorik group, particularly Victoria Switacz and Prof. Marc Spehr, whose biological expertise led to a fruitful collaboration project that broadened the scope and impact of this work.

I would like to thank my SFB colleagues and all those who organized the productive workshops and retreats that enhanced my research skills and provided valuable networking opportunities.

I also want to acknowledge my football teammates, led by Bernard Häßel. These regular activities provided essential balance and stress relief throughout the research process.

I would also like to warmly acknowledge the REMED group of Jacopo di Russo, who so kindly welcomed me as an honorary member of their team. The stimulating scientific discussions, shared lunches, and many activities we enjoyed together brought a wonderful sense of belonging and made this journey all the richer.

My deepest gratitude goes to my family, who have believed in me more than I perhaps deserved. I want to give special recognition to the help of Aleksandra Kozyrina — without her unwavering support and motivation, I cannot imagine completing this work.

Finally, I want to acknowledge all other colleagues and friends who, while not mentioned specifically here, hold a special place in my mind and heart. Each interaction, conversation, and shared moment has contributed to making this journey meaningful and enriching.

Abstract

Poly(N-isopropylacrylamide) (PNIPAM) microgels represent a versatile class of soft nanocarriers with significant potential for biomedical applications, particularly in drug delivery systems. However, the fundamental relationships between microgel physicochemical properties and their behavior at different interfaces—from solid surfaces to biological membranes—remain poorly understood. This thesis systematically investigates microgel characterization across multiple interfaces, establishing crucial structure-property relationships that govern both surface adsorption and cellular interactions.

When microgels adsorb at interfaces, they undergo extensive deformation and lateral spreading to minimize unfavorable contacts while maximizing interfacial area with polymer chains. This process becomes particularly complex for microgels with sophisticated architectures, where hollow cavities, rigid cores, or anisotropic shapes introduce additional mechanical constraints and heterogeneities that fundamentally alter their interfacial behavior.

Atomic force microscopy emerges as a uniquely powerful tool for investigating these complex deformation processes, enabling nanoscale characterization of mechanical properties under physiologically relevant conditions while simultaneously mapping three-dimensional distributions of stiffness throughout individual particles. The technique's ability to probe local resistance to deformation provides unprecedented insights into how internal architecture translates into interfacial mechanical signatures. This work systematically examines how small spherical hollow microgels, large anisotropic hollow and core-shell microgels behave during adsorption. The investigations demonstrate how cavity formation, shape anisotropy, and constrained deformation combine to create unique mechanical landscapes that govern adsorption and structure properties.

Moreover, the interfacial behavior of microgels serves as a predictive tool for cellular uptake ability. AFM force spectroscopy measurements on surface-adsorbed microgels reveal a remarkable correlation between mechanical properties and cellular internalization behavior using HEK293T cells as a model system. A normalized "relative indentation" parameter successfully predicts cellular uptake across diverse microgel types, identifying three distinct groups: fast uptake (highly deformable particles), intermediate uptake (moderately deformable systems), and no uptake (rigid large microgels). Remarkably, large ultra-low cross-linked microgels (>1 μm diameter) demonstrate successful cellular internalization despite exceeding typical size thresholds, with the fastest internalization time observed across all systems. Additional Post-internalization studies reveal that small microgels progressively accumulate in lysosomes (>75% after 4 hours) without significantly disrupting actin cytoskeleton organization, though modest changes in microtubule network architecture were observed. These findings prove the perspective of usage of microgels in biomedical application especially accompanied with powerful AFM characterization.

Kurzzusammenfassung

Poly(N-Isopropylacrylamid) (PNIPAM)-Mikrogele stellen eine vielseitige Klasse weicher Nanoträger mit erheblichem Potenzial für biomedizinische Anwendungen dar, insbesondere in Wirkstofffreisetzungssystemen. Die grundlegenden Zusammenhänge zwischen den physikochemischen Eigenschaften von Mikrogelen und ihrem Verhalten an verschiedenen Grenzflächen – von festen Oberflächen bis zu biologischen Membranen – sind jedoch noch unzureichend verstanden. Diese Arbeit untersucht systematisch die Charakterisierung von Mikrogelen an mehreren Grenzflächen und etabliert entscheidende Struktur-Eigenschafts-Beziehungen, die sowohl die Oberflächenadsorption als auch zelluläre Wechselwirkungen bestimmen.

Wenn Mikrogele an Grenzflächen adsorbieren, unterliegen sie einer ausgedehnten Verformung und lateralen Spreizung, um ungünstige Kontakte zu minimieren und gleichzeitig die Grenzfläche mit Polymerketten zu maximieren. Dieser Prozess wird besonders komplex für Mikrogele mit anspruchsvollen Architekturen, bei denen hohle Hohlräume, starre Kerne oder anisotrope Formen zusätzliche mechanische Zwangsbedingungen einführen, die ihr Grenzflächenverhalten grundlegend verändern.

Die Rasterkraftmikroskopie erweist sich als leistungsfähiges Werkzeug zur Untersuchung dieser Verformungsprozesse und ermöglicht die Charakterisierung mechanischer Eigenschaften im Nanometerbereich unter physiologisch relevanten Bedingungen, während sie gleichzeitig dreidimensionale Verteilungen der Steifigkeit in einzelnen Partikeln abbildet. Diese Arbeit untersucht systematisch, wie kleine sphärische hohle Mikrogele, große anisotrope hohle und Kern-Schale-Mikrogele sich während der Adsorption verhalten und wie Hohlraumbildung, Formanisotropie und eingeschränkte Verformung einzigartige mechanische Landschaften schaffen.

Das Grenzflächenverhalten von Mikrogelen dient zudem als prädiktives Werkzeug für die zelluläre Aufnahmefähigkeit. AFM-Kraftspektroskopie-Messungen an oberflächenadsorbierten Mikrogelen zeigen eine bemerkenswerte Korrelation zwischen mechanischen Eigenschaften und zellulärem Internalisierungsverhalten unter Verwendung von HEK293T-Zellen. Ein normalisierter Parameter der „relativen Eindringtiefe" identifiziert drei Gruppen: schnelle Aufnahme (hochverformbare Partikel), mittlere Aufnahme (mäßig verformbare Systeme) und keine Aufnahme (starre große Mikrogele). Bemerkenswerterweise zeigen große, extrem schwach vernetzte Mikrogele (>1 μm Durchmesser) erfolgreiche zelluläre Internalisierung mit der schnellsten beobachteten Internalisierungszeit. Post-Internalisierungsstudien zeigen, dass sich kleine Mikrogele progressiv in Lysosomen anreichern (>75 % nach 4 Stunden), ohne die Aktin-Zytoskelett-Organisation signifikant zu stören. Diese Erkenntnisse belegen die Perspektive der Verwendung von Mikrogelen in biomedizinischen Anwendungen in Verbindung mit leistungsfähiger AFM-Charakterisierung.

Contents

Abbreviations

AFM	atomic force microscopy
BIS	N,N’-methylenebisacrylamide
DOPC	1,2-dioleoyl-sn-glycero-3-phosphocholine
FLIM	fluorescence lifetime imaging microscopy
HEK293T cells	Human Embryonic Kidney 293T cells
JKR	Johnson-Kendall-Roberts
KPS	potassium persulfate
MAA	methacrylic acid
MRB	methacryloxyethyl thiocarbamoyl rhodamine B
NPs	nanoparticles
PAH	polyallylamine hydrochloride
PNIPAM	poly(N-isopropylacrylamide)
PNIPMAM	poly(N-isopropylmethacrylamide)
SLBs	supported lipid bilayers
STED	STimulated Emission Depletion
SUVs	small unilamellar vesicles
TPM	3-(trimethoxysilyl)propyl methacrylate
ULC	ultra-low cross-linked
VPTT	volume phase transition temperature

Chapter 1

Introduction

The continuous quest for advanced materials has driven science toward responsive and multifunctional systems that can adapt dynamically to environmental changes. Microgels have emerged as particularly attractive candidates due to the unique ability to combine features of colloids, hydrogels, and surfactants within a single system [1, 2]. This convergence of properties positions microgels as versatile platforms for applications ranging from drug delivery to emulsion stabilizers .

The synthetic versatility of microgels has led to a remarkable structural diversity, including hollow architectures, anisotropic shapes, and charged systems [3]. This architectural richness translates into correspondingly wide ranges of mechanical and interfacial behaviors, creating both opportunities for materials design and challenges for characterization. The complex, responsive nature of these materials necessitates advanced techniques like atomic force microscopy (AFM) capable of probing their properties in liquid state.

This work demonstrates that microgels with different architectures exhibit fundamentally different behaviors during interfacial adsorption and deformation. Through systematic AFM investigation of hollow, anisotropic, and charged systems, we reveal how structural features translate into distinct mechanical signatures. These findings establish quantitative structure-property relationships that enable prediction of microgel behavior across different environments.

Additionally, this research reveals that AFM-definded softness serves as a powerful predictive tool for cellular interactions. The mechanical properties measured using AFM directly correlate with the efficiency of cellular uptake efficiency, providing a rational framework for designing microgel-based drug delivery systems. This connection between interfacial mechanics and biological function represents a major advance in predicting the biomedical performance of soft materials.

This thesis therefore establishes that understanding interfacial deformation and mechanical behavior is critical for translating responsive materials from laboratory to real-world applications, highlighting the importance of accurate investigation of material-interface interactions.

1.1 Scientific background

1.1.1 Microgels as versatile colloidal materials

Microgels are cross-linked polymer networks dispersed in a solvent, typically water, with particle sizes ranging from nanometers to micrometers [1, 4, 5]. These soft colloidal particles occupy a unique position in materials science, combining the properties of colloids with the properties of hydrogels and interfacially active behavior [3]. Unlike linear polymers or hard colloids, microgels possess internal network structure that enables them to undergo reversible volume transitions in response to external stimuli such as temperature, pH, or ionic strength [6]. The cross-linked nature of microgels provides structural integrity while maintaining sufficient flexibility for large deformations. This dual character - structural stability combined with responsive deformability - is the foundation for their diverse application potential. The cross-linking density, typically ranging from 1 to 20 mol%, serves as a primary control parameter for mechanical properties, with lower cross-linking resulting in softer, more deformable particles [7, 8].

PNIPAM Microgels

Poly(N-isopropylacrylamide) (PNIPAM) represents the most extensively studied thermoresponsive polymer system for microgel applications and serves as the primary system investigated in this work. The volume phase transition temperature (VPTT) represents one of the most used characteristic properties of these thermoresponsive microgels. For PNIPAM microgels, the VPTT occurs at approximately 32 °C in pure water [1, 9]. This transition involves a dramatic change in particle size and internal structure. Below the VPTT, microgels exist in a highly swollen state with water-swollen polymer chains extended throughout the particle volume [10]. The swollen microgels are soft, highly hydrated, and easily deformable, making them ideal candidates for applications requiring high flexibility and responsiveness. Above the VPTT, the polymer-water interactions become unfavorable, leading to hydrophobic polymer-polymer interactions and water expulsion. This transition is accompanied by a significant reduction in particle size and a transformation from a fuzzy, extended structure to a more compact, homogeneous and spherical conformation [10].

The unique combination of colloidal stability, hydrogel-like responsiveness, and interfacial activity makes microgels attractive for a wide variety of applications: catalysis [11, 12], tissue engineering [13, 14], drug delivery [15–18] and others [3, 19]. Their interfacial activity makes microgels excellent candidates for emulsion [20] or foam stabilization [21], offering advantages over conventional surfactants due to their ability to respond to environmental changes while maintaining stabilization. In tissue engineering applications, microgels serve as scaffolds that can provide appropriate mechanical and chemical environments for cell growth, with the ability to dynamically adjust properties as tissue develops[14]. Additionally, they find use as functional coatings, where their responsive properties can be exploited for smart surface modifications [22].

This broad application spectrum drives the need for precise control over microgel properties, particularly their mechanical characteristics and responsive behavior, which forms the central focus of this thesis. The temperature responsivity of PNIPAM-based microgels can be tuned through copolymerization with hydrophilic or hydrophobic comonomers. For example, utilizing more hydrophilic co-monomer N,N'-dimethyacryl amide (DMAA) increase the VPTT of NIPAM-based microgels [23]. Incorporation of charged monomers such as methacrylic acid not only shifts the transition temperature but also introduces pH sensitivity [24], creating multiply responsive systems that can respond to both temperature and pH changes. Another approach for varying mechanical properties and functionality is to develop microgels with complex architectures [25–28].

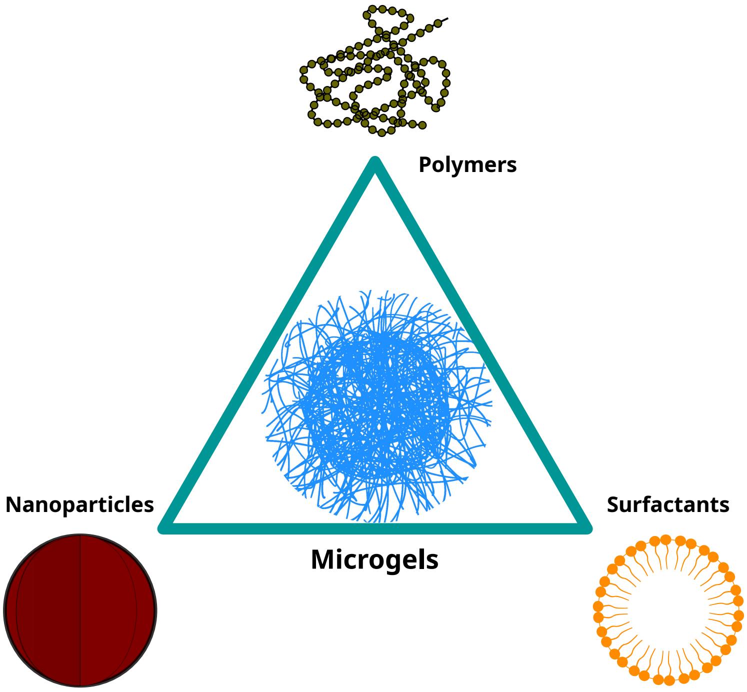

Fig. 1.1 Schematic representation of microgels as versatile colloidal materials sharing fundamental properties with nanoparticles, polymers, and surfactants, positioning them as a unique class of soft matter.

Types of Microgels

Nowadays, with different synthetic approaches, many types of microgels can be produced [3]. From different shapes like hollow [16, 29, 30] and anisotropic structures [25, 31], to multifunctional systems like Janus [32] or composite microgels incorporating gold [33], iron oxide [34], silica, and other nanoparticles. The microgel types that were investigated in this thesis will be described in more detail below.

Conventional Spherical Microgels. Conventional spherical microgels represent the most common and well-studied type of microgel architecture. The synthesis is commonly achieved through precipitation polymerization [35, 36], a versatile method that produces particles with narrow size polydispersity and allows for precise control over composition and architecture. In this process, the formation begins with the decomposition of an initiator into radicals at temperatures above the VPTT. The reaction proceeds through oligoradical chain growth, which eventually precipitates into precursor particles upon reaching a critical length, leading to final microgel formation. Due to the kinetics of radical polymerization, when synthesized using N-isopropylacrylamide (NIPAM) as the monomer and N,N'-methylenebisacrylamide (BIS) as the cross-linker, the faster consumption of the cross-linker compared to the main monomer creates a heterogeneous internal structure. This results in a cross-linker density that is highest in the center and decreases toward the particle exterior in the swollen state [37, 10]. These microgels are often described as "fuzzy spheres" as they consist of a denser, highly cross-linked core surrounded by a loosely cross-linked outer shell where the polymer density gradually decreases toward the periphery due to dangling polymer chains. While in the collapsed state, they resemble more homogeneous spheres with a box-like density profile.

Core-shell microgels. Core-shell microgels with non-polymeric cores represent a distinct class of hybrid materials where an incompressible solid core is surrounded by a polymeric shell. These structures can be synthesized using various inorganic materials as templates, including silica spheres, magnetic iron oxide nanoparticles, gold nanoparticles, and other functional materials. The resulting hybrid materials exhibit a combination of properties and the tunability of the core and shell design increases possible applications. The inorganic core provides could provide magnetic responsiveness [38], optical properties [39, 33], or enhanced mechanical stability, while the polymeric shell retains the characteristic stimuli-responsive behavior of microgels. The synthesis typically involves the coating of pre-formed inorganic nanoparticles with polymerizable monomers, followed by polymerization to form the cross-linked shell. The presence of the rigid core affects both the swelling behavior and mechanical properties of these hybrid microgels [40].

Hollow Microgels. Hollow microgels contain a solvent-filled cavity [41, 42] in their center and represent a unique architecture that offers distinct advantages for controlled release applications. These structures can be synthesized using sacrificial template methods, where a removable core material is first coated with the polymeric shell, and then the core is selectively dissolved or degraded to leave behind a hollow structure [29, 30]. Alternatively, they can be formed through using microfluidic devices, or emulsion process [43]. The hollow architecture provides several advantages, including increased loading capacity for guest molecules, reduced material usage, and unique mechanical properties. The presence of the central cavity affects both the swelling behavior and compressibility of these microgels, as polymer chains can rearrange into the empty volume during compression or deswelling.

Ultra-low cross-linked (ULC) Microgels. Ultralow cross-linked microgels represent an extreme case of soft particles that can be synthesized without the addition of any cross-linker agent. In this unique synthesis approach, the polymeric network forms exclusively through self-cross-linking of NIPAM due to transfer reactions initiated with a peroxydisulfate initiator [44–46]. Despite containing very few crosslinks, ULC microgels exhibit remarkable stability in solution, showing no indications of degradation upon heating/cooling cycles or after freeze-drying. These microgels possess a poorly cross-linked network with exceptionally low polymer density and a homogeneous distribution of crosslinks throughout their volume. SANS analysis reveals that ULC microgels have a much smaller shell compared to conventionally cross-linked microgels, with mesh sizes typically ranging from 12-25 nm compared to 7-12 nm for regular cross-linked systems. This unique architecture results in extremely soft particles with exceptional deformability, making them ideal for studying the limits of microgel softness and for applications requiring maximum particle flexibility.

1.1.2 Microgels at solid interfaces

The adsorption of colloidal objects at interfaces invariably involves specific interactions between their constituent materials and the surface [47]. These interactions are governed by the surface characteristics, including charge distribution, hydrophobic properties, and other molecular-level forces. Due to the soft and hydrated nature of microgels, their interfacial interactions exhibit significantly greater complexity compared to rigid colloidal systems.

Interfacial Interactions

For most surfaces, microgels spontaneously adsorb at the solid/fluid interface, resulting in a measurable reduction in interfacial tension [48]. To maximize this energetically favorable process, microgels undergo extensive deformation and lateral spreading to minimize unfavorable solid/fluid contacts while maximizing contact area with polymeric chains. This spreading behavior is ultimately constrained by network elasticity, which acts as the limiting factor against further deformation[49].

Additionally, electrostatic interactions play a crucial role, particularly for charged microgels interacting with oppositely charged surfaces. For instance, anionic microgels containing carboxyl groups readily adsorb onto glass surfaces functionalized with positive charged polymers like polyethylenimine, polyallylamine hydrochloride (PAH) [50]. In Chapter 4, PAH was used resulting in stable microgel-glass interaction that are well-suited for AFM characterization. While the adsorption process is driven by attractive electrostatic forces, the extent of particle deformation depends on the delicate balance between surface adhesion energy and the elastic resistance of the polymer network.

The heterogeneous internal structure of microgels introduces additional complexity to their interfacial behavior. The densely cross-linked core region provides mechanical stability and tends to maintain its structural integrity upon surface adsorption. In contrast, the loosely cross-linked corona undergoes significant spreading across the interface. For example, conventional spherical microgels that have core-corona structure in bulk solution, during adsorption onto the solid/air interface, form the so-called "fried-egg" structure due to the extremely soft corona and relatively stiffer cross-linked core [51, 52].

Deposition Methods

One of the important parameter that affects microgel interfacial interactions is the sample preparation methodology. Microgels can adsorb at solid interfaces via different pathways, with several deposition techniques available, each exerting distinct influences on the final microgel morphology. Spin-coating represents a frequently employed method wherein microgel solutions are deposited onto rotating solid substrates [53, 54]. To obtain well-separated microgels, either the spinning speed must be increased or the microgel concentration reduced. During this process, microgels adsorb at the solid/air interface and require subsequent rehydration for investigations in their native swollen environment. It should be noted that the external forces during spinning could damage the polymer network, which is especially crucial for ULC microgels [55].

Dip-coating and Langmuir-Blodgett deposition represent alternative approaches. In these methods, the solid substrate is transported through microgel-laden liquid/air or liquid/liquid interfaces [50, 52]. The Langmuir-Blodgett technique offers the particular advantage of controllable surface pressure during deposition, thereby enabling the formation of well-ordered microgel assemblies or monolayers. In contrast, in situ adsorption, also referred to as passive deposition, leads directly to microgels situated at the solid/liquid interface [55, 56]. In this approach, the solid substrate is incubated with low-concentration microgel solutions, followed by rinsing to remove unbound particles.

Implications for AFM Analysis and Material Design

Considering these factors collectively, the balance between interfacial deformation and network elasticity fundamentally dictates the final structure of microgels confined at interfaces, leading to substantial morphological changes during the adsorption process. This phenomenon must be considered from two complementary perspectives. From one standpoint, the analysis of adsorbed microgels will differ substantially from the analysis of microgels in bulk solution using conventional scattering methods, as surface-induced structural changes preclude direct correlation between interfacial and bulk properties. From the opposite perspective, this unique deformability represents a valuable functional characteristic that can be exploited to create complex surface coatings and should therefore be systematically studied at specific interfaces under controlled conditions. In this work, different types of microgels were characterized primarily on glass surfaces under various sample preparation protocols and environmental conditions.

1.1.3 Atomic Force Microscopy

The atomic force microscopy is a powerful surface imaging technique that enables detailed two- and three-dimensional visualization of material topography as well as phase maps with nanoscale resolution. The method was developed in 1986 by Binnig, Quate, and Gerber [57, 58] and has since become an indispensable tool in various scientific fields, including physics, biology, medicine.

Basic Principles

Fundamental Operating Principle. The operating principle of AFM is based on measuring the interaction forces between a probe attached to a flexible cantilever and the sample surface. The schematic image of the AFM device is illustrated on Fig. 1.2. As the probe approaches the sample, the cantilever deflection is monitored, allowing for the detection of interaction forces with piconewton sensitivity via Hooke's law. The scanning process is carried out using a piezoelectric drive that provides high-precision movement of the sample in three directions. That system must be able to perform with high-precision displacement range varies from sub-angstrom movements to several tens of micrometers [59]. A feedback-loop system is regulating the force between the sample and the probe and the piezoelectric drive [60, 61].

Detection System. Deflection registration of the cantilever is primarily performed using the optical lever method [62]. The principle of operation involves focusing a laser beam on the backside of the cantilever and detecting the reflected radiation using a quadrant photodiode. This configuration enables the detection of both normal and torsional movements of the cantilever. Design features of cantilevers play a significant role in the instrument's performance. Cantilevers are typically made of silicon or silicon nitride. To improve reflectivity, especially when working in liquid environments, the backside of the cantilever is coated with a thin metal layer, most commonly gold.

Modern Modes and Applications. The evolution of AFM technology has led to the development of specialized scanning modes tailored to specific research tasks. One significant advancement is the development of the quantitative nanomechanical Peak Force (PF-QNM) mode introduced by Bruker in 2011 [63]. This mode allows for the acquisition of nanomechanical property maps of soft samples with minimal probe-sample interaction, significantly expanding the method's capabilities with soft polymers.

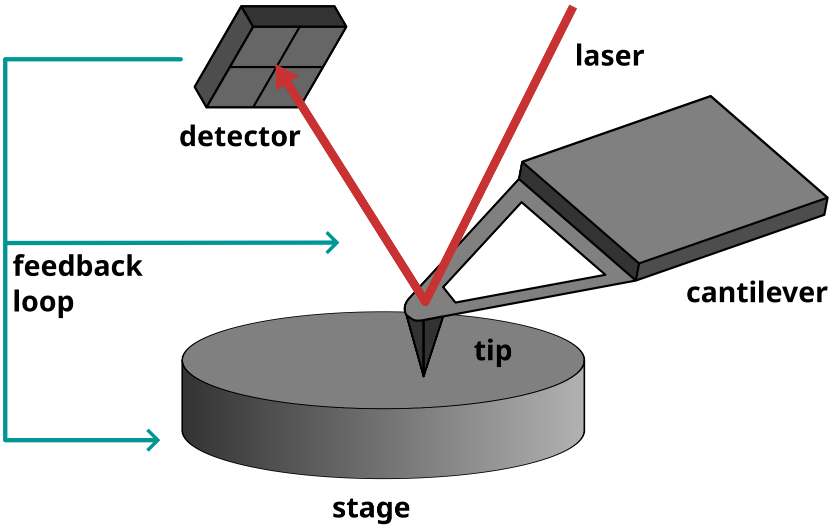

Fig. 1.2 Operating principle of atomic force microscopy: The cantilever deflection caused by tip-sample interactions is detected by the photodiode and processed through a feedback loop to maintain established settings while scanning the surface.

Force Spectroscopy

Force spectroscopy is a one of important application of atomic force microscopy [64–66]. A force-distance curve is a graph of the force experienced by the AFM cantilever versus the distance between the AFM tip and the sample surface (Fig. 1.3). During a force spectroscopy measurement, the probe is extended vertically towards the sample until a setpoint force interaction is reached and then retracted vertically from the sample.

A force-distance curve captures the relationship between applied force and tip-sample separation during a complete measurement cycle. The experimental procedure involves bringing the AFM probe into contact with the sample surface until reaching a predetermined force threshold, then withdrawing it back to the starting position. Throughout this process, the system continuously records cantilever deflection and vertical displacement, which are subsequently converted into force and distance measurements using Hooke's law.

$$F = -k_c \delta, \tag{1.1}$$

where $-k_c$ is the spring constant of the cantilever and δ the cantilever deflection.

Every force-distance measurement exhibits three characteristic phases that define the tip-sample interaction:

Non-contact baseline region: When probe and sample remain sufficiently separated, no measurable interactions occur, resulting in a flat baseline where force remains at zero (Fig. 1.3A,E).

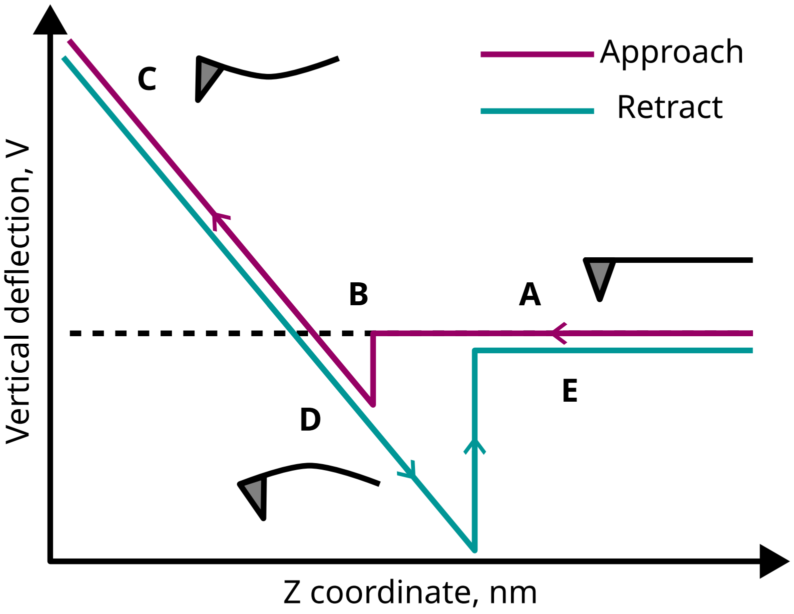

Fig. 1.3 Vertical deflection vs. distance curve. During the approaching phase (A), the cantilevers make contact with the sample surface (B) and their deflection is monitored (C). During the retraction phase (D), vertical deflection drops to negative values due to adhesion forces. After detachment, the deflection returns to zero value (E).

Transition region: As the gap narrows, attractive forces cause the tip to "jump-to-contact" with the surface during approach. Upon retraction, adhesive interactions create a "jump-off-contact" event where the tip suddenly detaches from the sample (Fig. 1.3B).

Contact region: Direct tip-sample contact leads to cantilever bending and potential sample deformation. The probe continues pressing into the material until reaching the set force limit, after which retraction begins (Fig. 1.3C,D). Due to adhesive forces, the separation process extends beyond the initial contact point before the tip completely disengages.

The shape and features of force-distance curves vary significantly depending on sample mechanical properties. Rigid materials such as glass produce steep, linear slopes in the contact region. These materials resist deformation, causing most applied force to deflect the cantilever rather than compress the sample. Soft materials like polymers, biological tissues, or microgels generate curves with initially shallow slopes that gradually steepen with increased indentation. The progressive slope change reflects the material’s compression and the nonlinear relationship between applied force and deformation depth.

Imaging modes

Contact Mode. Contact mode represents the most standard AFM operation, where the tip maintains continuous contact with the sample surface while scanning. In air measurements, the tip is dragged across the surface at constant force. Contact mode operates through continuous tip-sample contact during scanning with constant force feedback (typically 0.1-10 nN for soft samples), providing simultaneous topography and lateral force detection with high resolution imaging capabilities [67]. While the contact mode is a very simple imaging technique, it comes with disadvantages. It includes the risk of sample damage due to lateral shear forces during scanning and potential displacement or shifting of soft microgel particles across the substrate surface [67, 68].

Tapping Mode. Tapping mode AFM operates by oscillating the cantilever orthogonal to the sample surface at or near its resonance frequency (typically 50-400 kHz in air) with a defined amplitude. As the probe approaches the sample, tip-sample interactions affect the oscillation frequency and amplitude, which serve as setpoints for the feedback system [69, 70]. In addition to the topographic information, tapping mode imaging allows the detection of further sample properties. For example, this mode allows to measure phase images, that reflect energy dissipation between cantilever and sample. This phase contrast is sensitive to local sample composition and can reveal heterogeneity in samples with different physical properties [71, 72].

Tapping mode addresses the major limitations of contact mode by maintaining only periodic surface contact, greatly reducing lateral forces while increasing lateral resolution compared to contact mode. Although vertical forces are increased, this typically does not pose problems for most samples. For microgels, this gentler approach enables detection of fine structural features such as the thin corona regions that are missed in contact mode, making it particularly valuable for characterizing the fuzzy interfaces characteristic of these soft particles [51, 52].

Force spectroscopy modes

The main disadvantage of tapping and contact mode is the lack of information about force that was applied. That information is provided by force spectroscopy modes like Peak Force Tapping and Force Volume techniques. These techniques give ability to precisely control and measure the force of interaction between the tip and sample. This force control serves different but complementary purposes:

Peak Force Tapping. Peak Force Tapping is an advanced AFM technique developed by Bruker that directly measures pN-level interaction forces through cantilever deflection as the probe periodically taps the sample [63]. The technique operates through sinusoidal vertical modulation of the cantilever base relative to the sample surface, enabling relatively high scanning speeds comparable to standard tapping mode. This approach allows acquisition of thousands of force-distance ramps per second, compared to the 10 ramps per second limitation of conventional force volume [73, 74]. The sinusoidal waveform causes tip velocity to approach zero as it reaches peak force, enabling ultra-low interaction forces through continuous feedback control that benefits from results of previous taps. Each tap is processed in real-time to extract quantitative mechanical properties including modulus, adhesion, deformation, and energy dissipation.

The method offers significant advantages over conventional force-based techniques, particularly for soft materials like microgels. It prevents sample damage while the high acquisition rate enables detailed property mapping in much shorter times than force volume measurements. The technique is more stable than force volume due to reduced drift time and minimized tip wear. However, the sinusoidal oscillation creates variable tip velocities across each force curve, which may complicate analysis of viscoelastic samples where deformation rate affects measured properties.

Force volume mode. Force volume spectroscopy represents the most comprehensive AFM technique for mechanical characterization, providing detailed force-distance information at each point in a defined area [64, 66]. During the measurement the probe is moved vertically in a triangular manner. This approach enables three-dimensional mapping of mechanical properties with high spatial resolution.

Force volume measurements is a precise technique that provides comprehensive mechanical information, but requires significantly longer measurement times compared to other AFM modes. The extended acquisition periods make the technique sensitive to sample drift and other environmental artifacts that can affect data quality. However, despite these limitations, force volume provides invaluable three-dimensional information about sample softness that enables proper determination of both the size and internal softness features of soft samples like microgels, making it essential for detailed characterization of complex architectures and heterogeneous materials.

1.1.4 Fluorescence microscopy

Basic Principles

Fluorescence microscopy is based on the fundamental principle of fluorescence, where molecules called fluorophores absorb photons of light at one wavelength and subsequently emit photons at a longer wavelength [75]. This phenomenon can be understood through the Jablonski diagram (Fig. 1.4), which illustrates the electronic energy states of molecules and the transitions between them. When a fluorescent molecule (fluorophore) absorbs light, it gets instantly excited from its ground state (S_0) to higher energy levels like S_1 or S_2. This happens extremely quickly - in about 10^{-15} seconds - which is so fast that the molecule's structure does not have time to change. This instantaneous nature of light absorption is described by the Franck-Condon principle. Within each electronic state molecules can exist at different vibrational energy levels, creating a ladder-like structure of possible energy states.

After excitation, the molecule does not stay at the high energy level for long. Through a process called internal conversion, it rapidly loses excess vibrational energy and drops

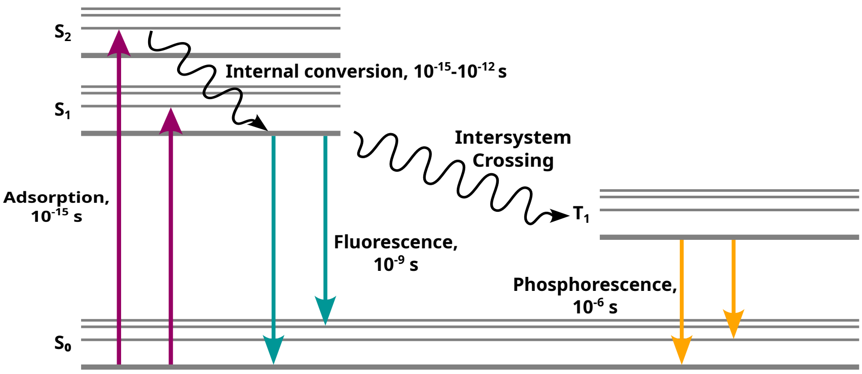

Fig. 1.4 Jablonski diagram of fluorescence. During excitation, fluorophore electrons are promoted from the ground state S_0 to higher vibrational levels of higher electronic states (S_1 or S_2). Rapid internal conversion then occurs to the lowest vibrational level of the same electronic state. Finally, fluorescence emission occurs as electrons transition back to various vibrational levels of the ground state S_0.

down to the lowest vibrational level of S_1. This happens within 10^{-12} seconds or less, which is much faster than the actual light emission process. Since fluorescence emission typically takes around 10^{-8} seconds, the internal conversion is always complete before any light is emitted. This means fluorescence always comes from molecules that have already settled into the lowest energy level of S_1 - a thermally equilibrated state. When the molecule finally returns to the ground state, it usually lands on a higher vibrational level of S_0, then quickly reaches thermal equilibrium. This pattern creates an interesting mirror-image relationship between absorption and emission spectra, since the vibrational spacing remains similar in both ground and excited states.

Some molecules can undergo intersystem crossing from S_1 to a triplet state (T_1), leading to phosphorescence. Phosphorescence emission is shifted to longer wavelengths (lower energy) and occurs much more slowly because the transition from T_1 back to S_0 is quantum mechanically "forbidden". Heavy atoms like bromine and iodine can facilitate this process, making phosphorescence more likely in molecules containing them.

The fundamental limitation of fluorescence microscopy is the diffraction limit (Eq. 1.2). When two fluorescent objects are closer than the minimum resolvable distance, their diffraction patterns overlap and merge into a single indistinguishable image, making it impossible to resolve them as separate structures.

$$r_{xy} = \frac{0.61\lambda}{n\ sin\alpha} = \frac{0.61\lambda}{NA}, \tag{1.2}$$

where, λ - wavelength of light, n - refractive index of medium, α - half-angle of maximum cone of light, NA = numerical aperture = n sin α.

Confocal microscopy

Standard fluorescence microscopy has some limitations - it collects light from a large volume along the Z direction, leading to blurred images due to out-of-focus fluorescence. To solve this, In 1957, Prof. Marvin Minsky introduced a pinhole aperture in the image plane on the detection side of the objective made the first confocal microscope [76]. This pinhole acts as a spatial filter that rejects out-of-focus light from planes above and below the focal point. That gave enormous new abilities for the measurement especially in thick samples. For example, it made possible to measure precise Z-stacks to create three-dimensional reconstructions of structures, that especially important in biology [77].

Spinning disk fluorescence microscopy

One of the disadvantages of conventional point-scanning confocal microscopy is the relatively long acquisition time required to build up an image, as each pixel must be illuminated and detected sequentially. To address these limitations, disk containing thousands of small pinholes arranged in Archimedean spirals (Nipkow disk) was implemented for fluorescence microscopy [78]. This approach addresses the temporal limitations of point-scanning confocal systems by implementing parallel confocal imaging. As the disk rotates at high speed (typically 1,800-10,000 rpm), each pinhole acts as a confocal aperture, creating multiple excitation spots that simultaneously scan across the specimen. This parallel illumination and detection dramatically increases imaging speed compared to sequential point scanning, making it ideal for live-cell imaging and dynamic processes.

STED microscopy

In the past decades, numerous techniques have been developed to overcome the fundamental diffraction limit of conventional fluorescence microscopy through controlled manipulation of fluorophore emission states [79]. Among these approaches, STimulated Emission Depletion (STED) microscopy has emerged as a particularly powerful method. The technique exploits the principle of stimulated emission, whereby photons of specific wavelength and phase force excited fluorophores to return to their ground state without fluorescence emission (Fig. 1.5A). STED microscopy operates using two synchronized laser beams: an excitation laser that promotes fluorophores to the excited state, and a depletion laser featuring a characteristic donut-shaped intensity profile that selectively suppresses fluorescence in the periphery of the excitation spot (Fig. 1.5B). The depletion laser is red-shifted relative to the fluorescence emission peak to maximize the efficiency of stimulated emission.

The efficiency of the stimulated emission process is scaled by the number of incident photons. If only enough photons are incident on the fluorophore, the S_1 state can be depleted before a fluorescence process can occur, and fluorescence is thus prevented. This optically saturable process introduces the nonlinearity that is exploited to increase the

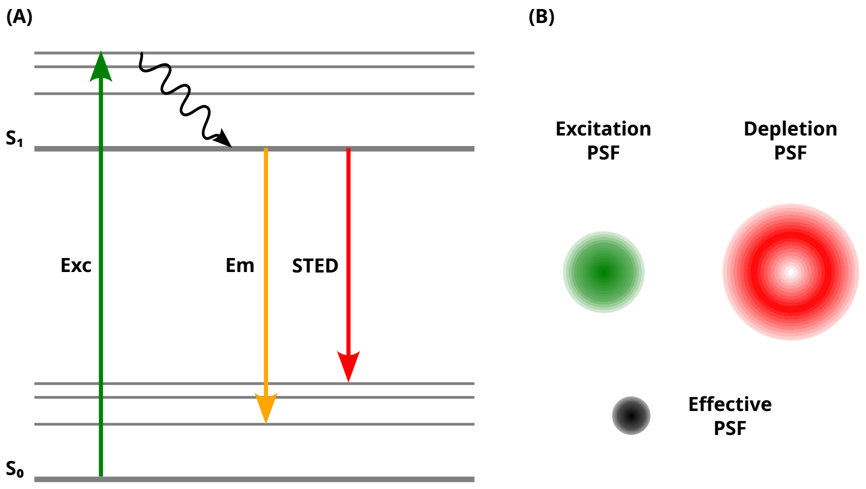

Fig. 1.5 STED microscopy Jablonski diagram showing the competition between spontaneous fluorescence emission and stimulated emission depletion (A). The characteristic donut-shaped intensity profile of the depletion laser reduce the point spread function (PSF) of the fluorescence (B).

resolution in STED microscopy by using high intensities for the depletion laser. The new STED resolution limit depends on the ratio between intensities of depletion laser and saturation of fluorophore (Eq. 1.3).

$$r_{xy(STED)} = r_{xy} \Big/ \sqrt{1 + \frac{I_{STED}}{I_{sat}}}, \tag{1.3}$$

In the experiments, practical limitations such as photobleaching and cytotoxocity constrain the achievable resolution to 30 nm lateral resolution [80]. The high laser intensities also affect the photobleaching not only in the image plane, but also in the light cone above and below the focal spot. In Chapters 4, 5 of this thesis, STED microscopy was utilized to investigate cytoskeletal structural changes during microgel uptake and to localize internalized microgels within cells, including their colocalization with lysosomes.

1.2 Thesis Structure

In this thesis, microgel interactions with solid surfaces and cells have been investigated for different types of microgels with varying architectures and mechanical properties. Chapter 1 briefly introduces the background of microgels and their interface behavior, accompanied by descriptions of the main characterization methods: atomic force microscopy and fluorescence microscopy techniques. Chapter 2 examines how hollow and anisotropic microgels behave during interfacial adsorption, establishing fundamental principles of cavity-induced softness and shape-dependent assembly. The systematic AFM investigation progresses from spherical hollow microgels through anisotropic hollow systems to anisotropic core-shell microgels, revealing how internal architecture and external geometry combine to determine mechanical properties and assembly patterns at interfaces. Chapter 3 introduces quantitative examination of microgel adhesion properties and contact mechanics for understanding deformation behavior on solid substrates. Chapter 4 introduces the biomedical aspects of microgel interface interactions, demonstrating that AFM-defined softness correlates with cellular uptake in a systematic but complex manner. Using Human Embryonic Kidney 293T cells (HEK293T cells) as a model system, the chapter establishes a "relative indentation" parameter that successfully predicts cellular internalization across several microgel types. Chapter 5 goes further into biomedical applications, investigating the post-endocytotic effects of microgel internalization on cytoskeletal structure and lysosomal processes.

Chapter 2

AFM Study of microgels with Hollow and Core-Shell Architectures

2.1 Introduction

Microgels represent a fascinating class of soft materials that combine the unique properties of polymers, colloids, and surfactants within a single system [3, 6]. These cross-linked polymer networks, typically swollen in a good solvent such as water, form three-dimensional macromolecular structures with size ranging from nanometers to micrometers. The distinctive property of microgels is their ability to deform, shrink under external force due to their soft nature [81]. The stimuli-responsive nature of microgels has positioned them as promising agents in numerous fields, from industrial catalysis [82] and to drug delivery systems [83, 84]. Their ability to undergo controlled swelling and deswelling in response to multiple external stimuli—such as temperature, pH, and ionic strength—provides unprecedented control over material properties and functionality [3].

Among the various temperature-responsive polymers, poly(N-isopropylacrylamide) (PNIPAM) and its derivative poly(N-isopropylmethacrylamide) (PNIPMAM) have emerged as standard systems for fundamental studies and applications. These polymers exhibit a lower critical solution temperature (LCST) in aqueous solutions, leading to a sharp volume phase transition that can be precisely tuned through chemical modifications and crosslinking density. The well-characterized nature of these systems, combined with their biocompatibility, has made them ideal model systems for understanding the fundamental principles governing microgel behavior.

While conventional microgels have demonstrated remarkable properties, hollow microgels represent an further advancement that offers additional degrees of freedom and enhanced functionality. These systems possess a solvent-filled cavity that provides extra space for polymer chain expansion and fundamentally alters their mechanical behavior compared to their solid counterparts [85, 29]. The hollow architecture creates unique opportunities for encapsulation and controlled release [86, 87].

Rod-shaped particles provide an alternative approach to form complex structures, offering access to rich phase behaviors that include liquid crystalline phases not accessible to spherical particles. The aspect ratio of rod-shaped particles is a critical parameter that determines the nature of the phases formed, with increasing elongation leading to the emergence of nematic and smectic phases characterized by long-range orientational and positional order.

While the phase behavior of rigid colloidal rods has been extensively studied both theoretically and experimentally, the influence of particle softness on these phase transitions remains largely unexplored due to the historical absence of appropriate model systems. Rod-shaped microgels address this gap by combining the rich phase behavior of anisotropic particles with the unique properties of soft, responsive materials. The synthesis of such systems using rod-shaped silica templates provides access to micrometric hollow rods with controlled aspect ratios and responsive properties.

Capillary interactions occur when rigid particles float at fluid interfaces. These interactions arise from interface deformations that minimize the total interfacial energy, driving particles to self-assemble in configurations that maximize the overlap of induced interfacial distortions. The surface can be disturbed by factors like particle roughness, gravity, or non-spherical shapes, leading to various organized patterns such as chains, flower-like clusters, or triangular networks depending on the particle shape. In case of ellipsoidal particles quadrupolar interaction plays dominant role in the patterns formation [88, 89]. The contact angle must satisfy the Young-Laplace equation (that connects capillary pressure with surface tension and shape curvatures) around the entire particle perimeter, which for ellipsoids requires deformation of both the contact line height and the surrounding interface. This leads to orientation-dependent capillary interactions, with ellipsoidal particles showing a transition from triangular assembly at low aspect ratios to side-by-side linear arrangements at higher aspect ratios.

When anisotropic microgels adsorb at interfaces, their soft polymeric shells undergo lateral spreading and deformation, altering the capillary interaction mechanism compared to rigid particles. This deformation creates contact line fluctuations and interface distortions that depend strongly on the particle's core aspect ratio and shell architecture. Ellipsoidal microgels, obtained through mechanical deformation of initially spherical systems, provide an excellent model system for studying these effects. The core-shell architecture, consisting of a stiff polystyrene core surrounded by a soft PNIPMAM shell, creates a system where the rigid core maintains the anisotropic shape while the soft shell can undergo significant deformation at interfaces.

Understanding how various microgels interact with interfaces requires advanced testing techniques that can provide detailed information about their structure, size and softness. Atomic force microscopy (AFM) has emerged as an indispensable tool for soft matter characterization [90, 91] including elasticity measurements [92], nanorheology [93]. The ability of AFM to operate in various environments—from air to aqueous solutions—makes it particularly well-suited for studying environmentally responsive materials. In the context of hollow microgels, measurement in dried state in combination with force spectroscopy measurements in aqueous solution with sharp tip provide valuable information about microgels' ability to deform and their internal structure. The force spectroscopy technique's high spatial resolution allows for the detection of structural heterogeneity within individual particles and can reveal details about shell thickness and cavity dimensions that are difficult to obtain through other methods [94]. For anisotropic microgels at interfaces, AFM offers the unique ability to directly visualize particle deformation and spreading behavior. Peak Force QNM (Quantitative Nanomechanical Mapping) in combination with force spectroscopy mode enables not only mapping of topography and mechanical properties of individual microgels but also provides insights about the formation of specific assembly patterns due to capillary interactions.

This chapter presents a comprehensive AFM-based characterization of three distinct microgel systems: two spherical hollow microgels systems, rod-shape hollow and core shell anisotropic microgels, capillary patterns of ellipsoidal core-shell microgels. Through detailed topographical and mechanical analysis, we aim to elucidate the relationship between particle architecture, environmental conditions, and resulting material properties. The work demonstrates how AFM can provide unique insights into the behavior of complex soft matter systems, contributing to our fundamental understanding of responsive materials and their potential applications.

2.2 Materials and Methods

Microgel Synthesis

Synthesis of Spherical Hollow Microgels. The synthesis of micro-sized responsive hollow microgel capsules was executed using a four-step sacrificial template approach as schematically depicted in Fig. 2.1. In the first step, silica templates were generated using a semi-continuous Stöber method. Fluorescently-labeled silica seeds (179 ± 10 nm radius) were prepared via the Stöber method and subsequently grown to micro-sized silica particles (538 ± 45 nm radius), with seed concentration and other factors varied to achieve the appropriate particle size and polydispersity. In the second step, the surface of the silica templates was modified with 3-(trimethoxysilyl)propyl methacrylate to introduce polymerizable double bonds. In the third step, core-shell silica/microgel particles were synthesized via precipitation polymerization. For neutral hollow microgels, NIPAM (94 mol%), BIS (5 mol%), and potassium persulfate (KPS) (1 mol%) were polymerized at 70 °C for 3 hours in the presence of surface-modified silica particles. For charged hollow microgels, NIPAM (89 mol%), DMI (5 mol%), BIS (5 mol%), and KPS (1 mol%) were used under identical conditions. The neutral monomer DMI was chosen because it does not reduce colloidal stability and can be saponified to itaconic acid (IA) in contrast to charged monomers. Both systems were fluorescently labeled with methacryloxyethyl thiocarbamoyl rhodamine B (MRB). In the fourth step, hollow microgel capsules were obtained by dissolving the silica cores in 0.05 M NaOH solution for three days, followed by extensive dialysis against NaOH and subsequently against water to remove residual silica fragments, yielding the final charged microcapsules.

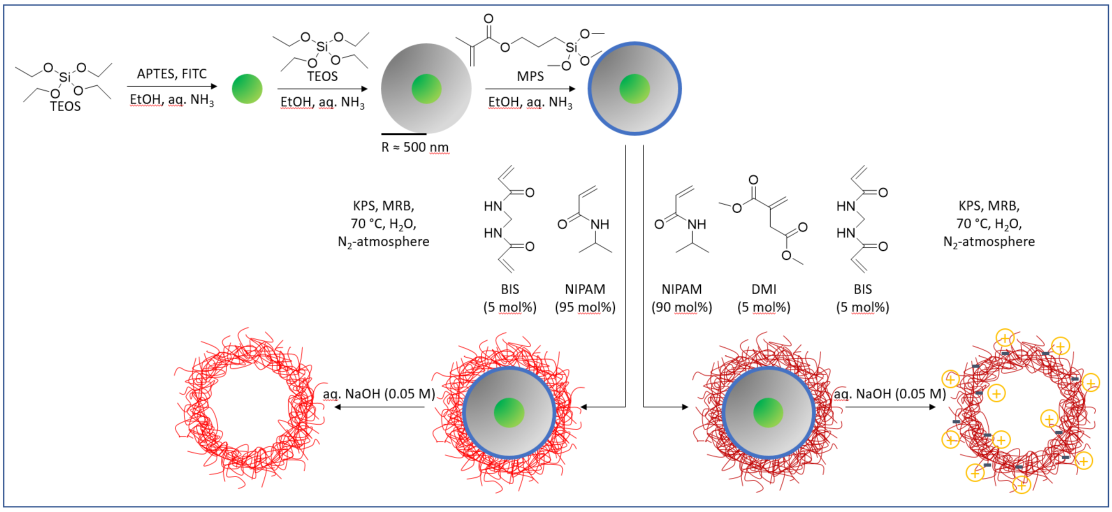

Fig. 2.1 Schematic four-step synthesis of spherical hollow microgels, including preparation of silica templates, modification of silica surface, microgel shell polymerization, and silica core dissolution.

Synthesis of Hollow Rod-Shaped PNIPAM Microgels. Anisotropic hollow microgels were synthesized using a four-step sacrificial template approach. First, fluorescently-labeled silica rods were prepared via a modified Stöber growth procedure in 1-pentanol with PVP, followed by fractionation to reduce polydispersity. The silica rods were then surface-functionalized with 3-(trimethoxysilyl)propyl methacrylate (TPM) in ethanol/ammonia solution at 75 °C to introduce polymerizable vinyl groups. Core-shell silica/microgel particles were synthesized via seeded precipitation polymerization using NIPAM (94 mol%), BIS (5 mol%), and KPS (1 mol%) at 70 °C for 3 hours in the presence of TPM-coated silica rods. The system was fluorescently labeled with rhodamine B methacrylate. Finally, hollow anisotropic microgels were obtained by dissolving the silica cores in 0.1 M NaOH for 8 days with solution refreshment, followed by extensive washing with water. Complete template removal was confirmed by transmission electron microscopy.

Synthesis of Anisotropic Core-Shell PNIPMAM Microgels. Anisotropic core-shell microgels were synthesized using a three-step approach. First, polystyrene core particles were prepared by emulsion polymerization using styrene (48.3 g), NIPMAM (2.625 g), and SDS in water at 80 °C for 8 hours with KPS initiator, yielding a 5.1 wt% stock dispersion after purification. Core-shell microgels were then synthesized by seeded emulsion polymerization using the polystyrene cores (32 g), NIPMAM (1.61 g), BIS crosslinker (0.1 g), and rhodamine B methacrylate for fluorescent labeling. The reaction was conducted at 80 °C for 8 hours under nitrogen atmosphere with KPS initiator. Finally, anisotropic particles were obtained through mechanical stretching by embedding core-shell microgels in PVA films and elongating them at 145 °C using different draw ratios (λ = 1.50-5.00) [95]. Stretching above the polystyrene glass transition temperature resulted in plastic deformation, converting spherical core-shell microgels into ellipsoidal particles with con-

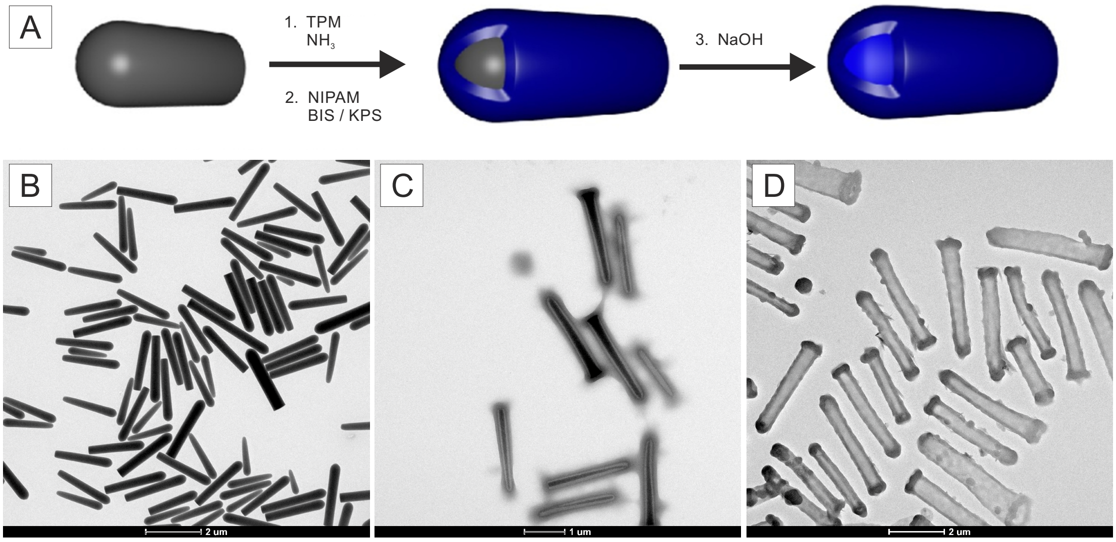

Fig. 2.2 A) Schematic representation of the synthetic procedure to obtain hollow microgel using silica rods as sacrificial template. (B-D) Transmission electron microscopy (TEM) images of (B) silica rods, (C) microgel coated silica rods and (D) etched hollow microgel rods. In respect to their anisotropy, anisotropic microgels tend to assemble side to side into short string due to capillary interactions.

trolled elongation ratios. In this study, spherical microgels without stretching ($\lambda = 1$) and ellipsoids with $\lambda = 2$ and 5 were investigated (Fig. 2.3).

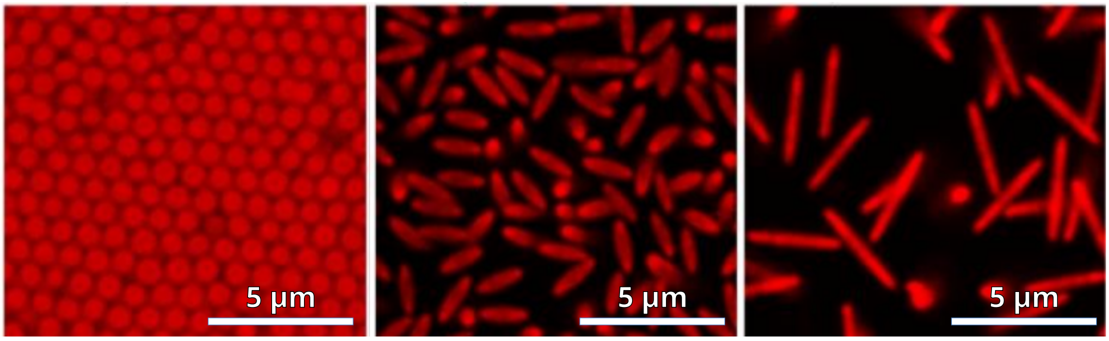

Fig. 2.3 Representative confocal images of the prolate-shaped soft microgels obtained for different draw ratio λ. From Left to Right: original $\lambda = 1.00$, 2.00, and 5.00 (Reproduced from ref [95]).

AFM Characterization

AFM measurements were performed on a Dimension Icon AFM with a closed loop (Veeco Instruments Inc., software Nanoscope 9.4 (Bruker Corporation)). Acquired data was processed using Nanoscope Analysis and Gwyddion. The sample preparation and further AFM investigation of microgels vary for each type of microgel.

In case of measurement on glass/air interface, microgels were investigated in the dried state in tapping mode using OTESPA tips with a resonance frequency of 300 kHz, a nominal cantilever spring constant of 26 Nm^1, and a nominal tip radius of < 7 nm (NanoAndMore GmbH, Germany).

In case of measurement on glass/water interface, microgels were measured in a customized liquid cell on a heating stage (Dimension Icon Electrochemistry Chuck, Bruker Corporation) with temperature control (Model 335 Cryogenic Temperature Controller, Lake Shore Cryotronics). The microgels were measured at T = 27 °C, temperature was equilibrated for 60 min before measurement. Contact stiffness measurements were carried out using the Peak Force QNM and Force Volume modes with modified MSNL-E (Bruker Corporation) tips. These E-tips have a nominal resonance frequency of 15 kHz in air and a nominal spring constant of 0.1 N/m, with a tip radius of 2 nm and a semi-angle of 23°. The AFM tip was activated by oxygen plasma treatment (PVA TePla plasma system 100) at 1.4 mbar oxygen pressure and 200W microwave power for 5 minutes immediately before measurements.

For analyzing the force volume data, firstly, the data were extracted using Nanoscope Analysis 1.9 Software (Bruker Corporation) and processed using custom-made MATLAB scripts specifically developed for microgel force-distance curve analysis and contact stiffness calculations. All force-distance curves underwent systematic baseline correction and contact point determination using established algorithms adapted for soft microgel analysis. Contact points were identified using a combination of threshold detection and curve fitting methods to account for the gradual onset of repulsive forces characteristic of soft, deformable particles. The contact stiffness parameter, defined as the local derivative of force with respect to indentation depth (dF/dδ), was calculated to provide contact stiffness microgels profiles. Based that profiles a 3D visualization of microgels was made.

Spherical hollow microgels.

Sample preparation. The core-shell silica/PNIPAM and silica/P(NIPAM-co-IA) microgels and their corresponding hollow PNIPAM and P(NIPAM-co-IA) capsules were deposited onto glass slide either by spin-coating or dropcasting. First, glass coverslips with the size of 2.2 x 2.2 cm (Menzel-Gläser, n4) were cleaned in an isopropanol chamber by sonicating it for 15 mins. After that, the air-dried glass slide was activated by placing it inside the UV Ozone cleaner (NanoBioAnalztics UVC 1014) for 15 mins. For the spin-coating approach, 120 μL of the redispersed microgel solution with concentration 0.01 wt% was dispensed onto the center of the glass slide. Then the slide was spin coated at a speed of 2500 rpm for 30 s (Convac 1001S). For the dropcasting adsorption method, 120 μL of the microgel solution was applied to the glass slide and left to the complete evaporation at room temperature.

AFM characterization. Both systems of hollow and core-shell microgels were measured in tapping mode in dried state.

Hollow rod-shaped microgels.

Sample preparation. The core-shell and hollow rod-shaped microgels were deposited onto glass slide by *in situ* adsorption method. Initially, glass coverslips with the size of 2.2 x 2.2 cm (Menzel-Gläser, n4) were cleaned in an isopropanol chamber by sonicating it for 15 mins. Then, 120 μL of the microgel solution was applied to the glass slide and allowed to adsorb for 1 hour at room temperature. Following the adsorption period, the slide was carefully rinsed several times with 2 mL aliquots of water to remove any unbound microgels. The prepared samples were measured immediately

AFM characterization. Initially, the Peak Force QNM mode was used to scan broad regions and identify areas of interest. Subsequently, areas containing one or two rods were selected for detailed measurements, with scan sizes of 5.0 x 5.0 μm^2 or 7.0 x 7.0 μm^2. Force Volume mode measurements were then performed with a 192 x 192 data point grid, a force threshold of 5 nN, a ramp size of 1.5 μm, a ramp rate of 10 Hz, and 3072 samples.

Ellipsoid core-shell microgels.

Sample preparation. A thin glass slide (24 × 50 mm) was used for the particle dip-coating deposition, which was cleaned in an isopropanol chamber by sonicating it for 15 mins. After that, the air-dried glass slide was activated by placing it inside the UV Ozone cleaner (NanoBioAnalztics UVC 1014) for 15 mins. In parallel, the glass slide holder of the custom-designed dip coater was cleaned with isopropanol 2-5 times and dried repeatedly. Then, the reservoir was also cleaned with ethanol and MilliQ water and thoroughly dried. The UV Ozone-cleaned thin glass slide was fixed with the cleaned glass holder in such a way that the glass slide makes an approx 45° angle with the interface. The reservoir was filled with 120 mL MilliQ water and the water interface was cleaned by airflow, and subsequently, the glass slide was slowly dipped inside the reservoir. Each microgel sample was prepared by adding 120 μL of the microgel (0.1 wt%) aqueous dispersion into 30 μL of isopropanol for the dip-coating experiments. Then, 130 μL of the prepared microgel dispersion was added to the water interface by using a syringe cleaned by MilliQ and isopropanol repeatedly and left for 30 mins. After the equilibration time, the immersed cover slip was retrieved, and the dip-coating technique was started with the belt position up 0.09 - 5.9 mm/min to the belt position down 0.01 - 0.65 mm/min for the next 20 mins.

AFM characterization. Initially, the configuration and patterns of adsorbed soft microgels was investigated in the dried state with wide scan areas of of 50 x 50 μm^2. Then the Peak Force QNM The distribution of PNIPMAM shell was investigated in water in the Peak Force QNM and Force Spectroscopy modes. First, mode was used to scan broad regions and identify areas of interest. Subsequently, areas containing several rods were selected for detailed measurements, with scan sizes of 4.0 x 4.0 μm^2. Force Volume mode measurements were then performed with a 192 x 192 data point grid, a force threshold of 5 nN, a ramp size of 1.5 μm, a ramp rate of 10 Hz, and 3072 samples.

2.3 Results

2.3.1 AFM analysis of Spherical Hollow Microgels

AFM measurements were performed to probe the morphology of the core-shell and hollow microgels in their dried state. First, core-shell neutral and charged microgels were measured in tapping mode (Fig. 2.4A,B). Both systems appear slightly anisotropic as a consequence of their topological interaction with the substrate and the inherent cantilever geometry effects during scanning. Notably, we did not observe any microgel shell on the glass substrate, which could be explained due to the large height of the core-shell microgels. The measured transverse and longitudinal height profiles are displayed in Fig. 2.4C,D for characteristic neutral and charged core-shell microgels. Both profiles appear almost identical, exhibiting heights on the order of the silica core diameter, which strongly suggests the presence of a very thin microgel shell surrounding the rigid core. Interestingly, the lateral diameter is approximately 200 nm larger than the particle maximal height, creating an aspect ratio that deviates from spherical geometry. This dimensional difference could be attributed to geometric factor: the pyramidal geometry of the AFM cantilever leading to tip convolution effects.

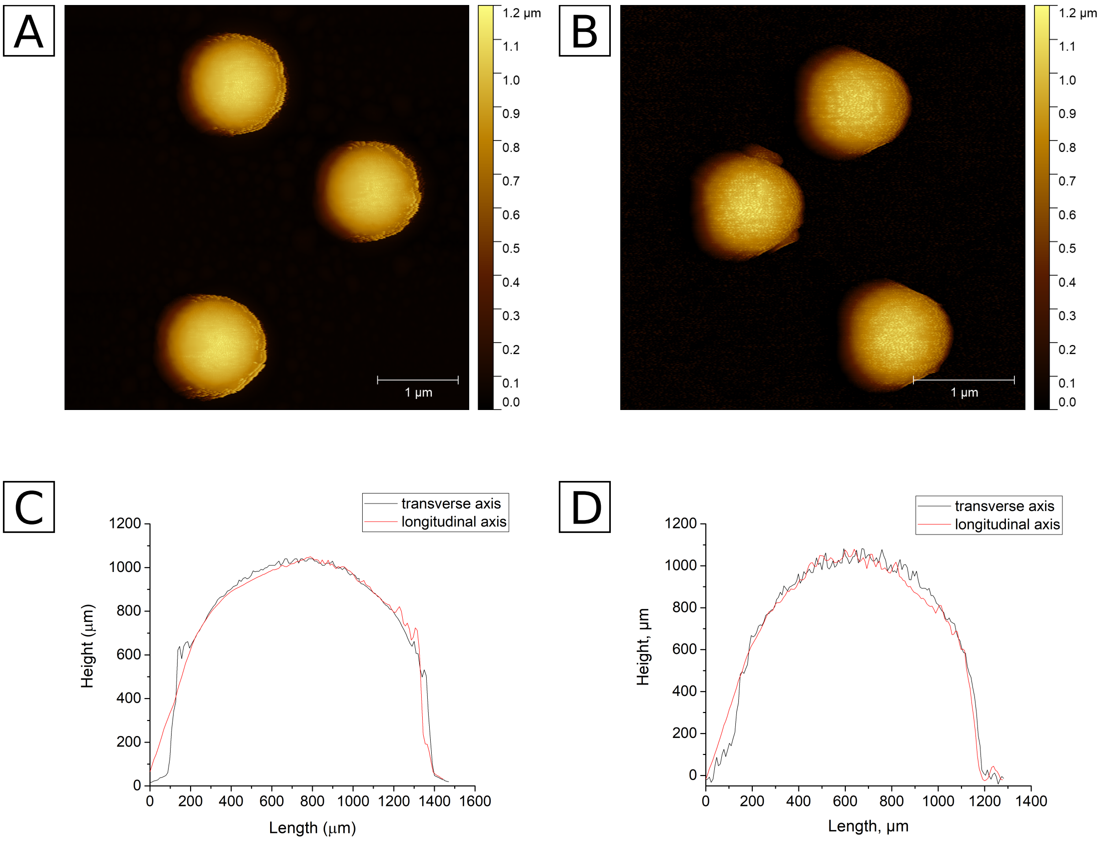

Fig. 2.4 AFM Height micrographs and characteristic transverse and longitudinal height profiles measured on core-shell microgels. (A), (C) correspond to the charged; (B), (D) to the neutral ones.

The cores of the two core-shell systems were subsequently dissolved in NaOH solution to yield hollow microgel capsules. A dramatic change in microstructure was observed in comparison to the core-shell systems, highlighting the crucial role of the rigid silica core in maintaining particle integrity. Although individual objects can still be observed, the resulting particles at the glass surface are highly deformed and present a buckled and wrinkled conformation characteristic of collapsed soft capsules, as shown from AFM height imaging in the dried state of dropcasted samples (Fig. 2.5). The microgel capsule contact areas, which maintain mostly circular symmetry despite significant deformation, exhibit large variations in diameter ranging from approximately 1 to 3.5 μm. These dimensions far exceed those of the original core-shell systems (diameter of core-shell microgel is about 1 μm), indicating substantial lateral spreading upon substrate contact. This spreading behavior shows the extreme softness of the microgel capsules.

The neutral hollow microgels spread and flatten at the substrate, adopting either a wrinkled conformation characterized by a smaller diameter but higher residual thickness, or a fully adsorbed conformation with maximum lateral extension (Fig. 2.5A-C). Their average lateral dimensions are almost two times smaller than their charged counterparts, which is also reflected in their height profiles, suggesting a more constrained spreading behavior. This difference can be attributed to the absence of long-range electrostatic repulsion in the neutral state, allowing for closer packing of polymer chains and reduced driving force for lateral expansion.

In comparison, the charged hollow microgels tended to form large, thin, and sometimes partially disrupted systems that could correspond to ruptured capsules (Fig. 2.5D-F). This rupturing phenomenon likely occurs when the electrostatic pressure within the charged polymer network exceeds the mechanical strength of the shell material, leading to material redistribution across the substrate. From the comparative analysis of height profiles, we can infer that after adsorption and drying, neutral microgels better maintain their capsular integrity. The large spreading of the charged microgel capsules can be rationalized through several contributing factors: (i) repulsive electrostatic interactions between the negatively charged polymer chains within the shell, and (ii) unfavorable electrostatic interactions with the negatively charged ozone-treated glass substrate, which promotes lateral.

For additional investigation, both hollow microgel capsules systems were also measured after spin-coating sample preparation. The choice of preparation method significantly influences the final particle morphology due to differences in drying kinetics, applied forces, and solvent evaporation rates. All glass slides were subjected to a standardized cleaning protocol involving sonication in isopropanol followed by activation in O_3/ozone plasma. This ozone treatment serves multiple purposes: (i) removal of organic contaminants, (ii) generation of surface hydroxyl groups that increase hydrophilic features.

Spin-coated samples were processed immediately after dispersion application. The additional centrifugal force makes microgel morphology more uniform with less variation in topology and dimensions compared to dropcasted samples. The rapid solvent removal

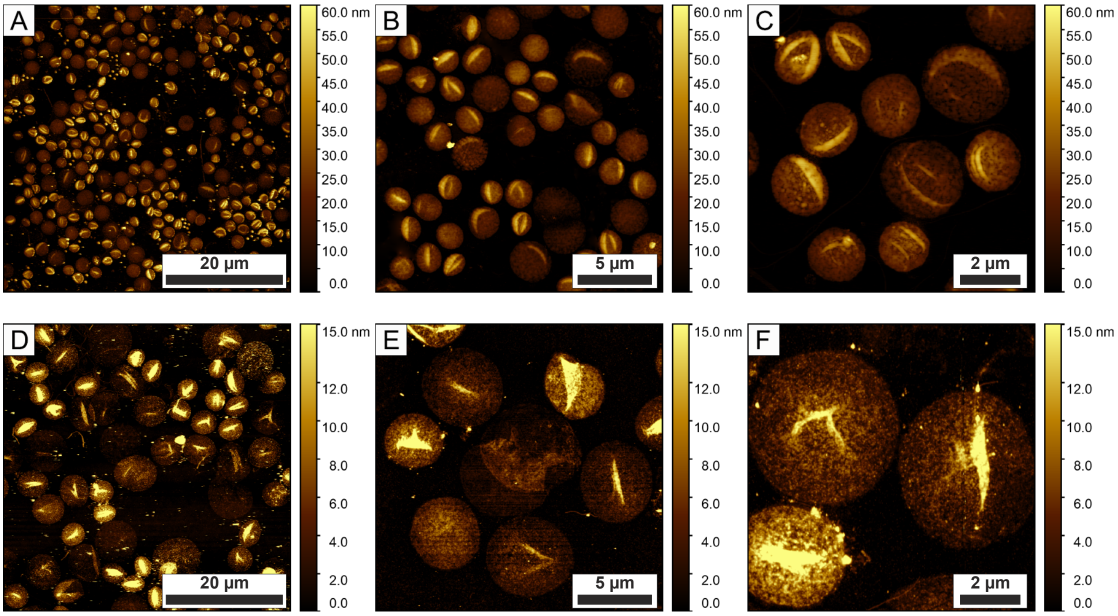

Fig. 2.5 AFM height micrographs of the neutral PNIPAM (50 x 50 μm^2, 20 x 20 μm^2, 10 x 10 μm^2) (A-C) and charged P(NIPAM-co-IA, pH = 9) (50 x 50 μm^2, 20 x 20 μm^2, 10 x 10 μm^2, zoom in) (D-F) capsules respectively. Measurements were performed under dry conditions after dropcasting using tapping mode.

and applied mechanical forces tend to "freeze" the particles in conformations that may not represent their equilibrium state, but provide better reproducibility for quantitative analysis. Only isolated microgels could be effectively probed using this method due to the lower surface coverage achieved through the spin-coating process. Height micrographs of characteristic neutral and charged hollow microgel capsules are shown in Fig. 2.6A and B, respectively. Both systems appear as circular disk-like structures, with charged capsules exhibiting much larger radii compared to neutral ones. Conversely, neutral capsules maintain significantly greater thickness than their charged counterparts, suggesting different deformation mechanisms. These observations were quantitatively supported by average radial height profiles measured on seven capsules for each system (Fig. 2.6C). The statistical analysis reveals that charged capsules spread extremely thin with an average height of approximately 7 nm, while neutral capsules maintain an average height of approximately 20 nm—nearly three times thicker.

The average height of each measured system is plotted as a function of radius for both preparation methods in Fig. 2.6D. Remarkably, the data reveals a clear scaling relationship where the height varies inversely with the square of the radius ($h \propto 1/R^2$). This scaling relationship provides compelling evidence that despite the dramatic morphological changes observed upon core dissolution and substrate adsorption, the total amount of polymer material remains constant. The relationship is consistent with the volume conservation equation for a disk-shaped object ($V = \pi R^2 h$), indicating that both neutral and charged capsules are indeed monodisperse and possess the same mass. This finding validates the core dissolution process as a successful method for creating hollow capsules without

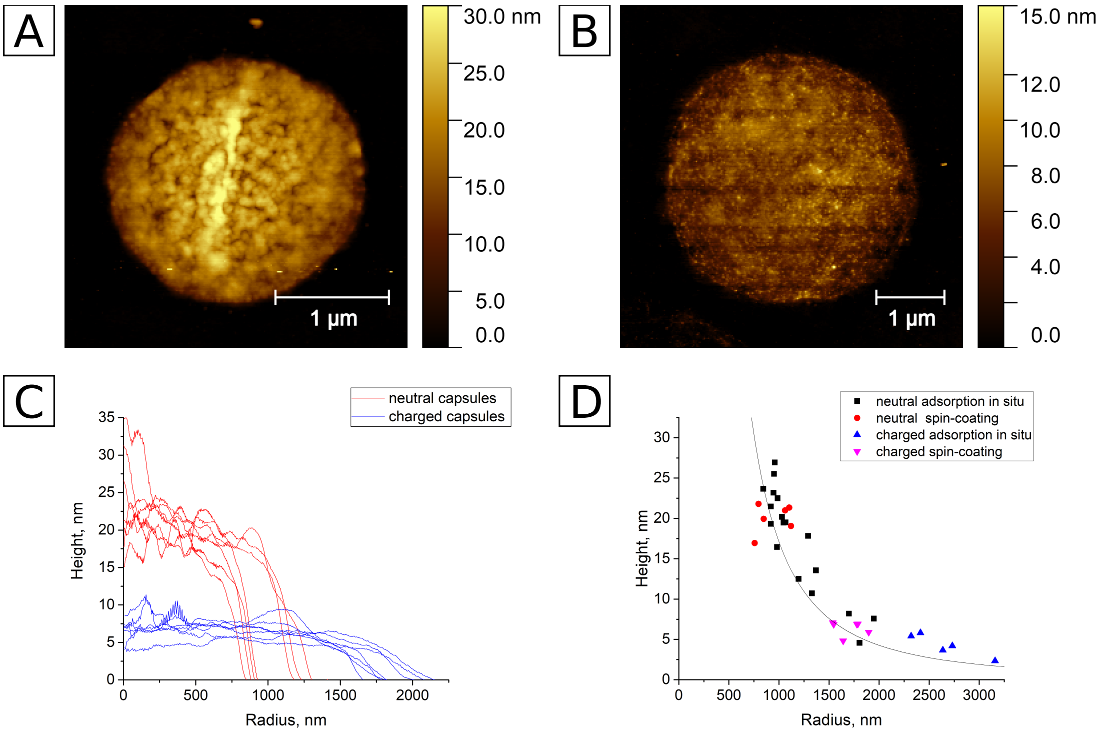

Fig. 2.6 (A) and (B) AFM Height micrographs of neutral and charged hollow capsules measured under dry conditions after spin-coating. (C) Average radial profiles of single neutral (red) and charged (blue) capsules measured under dry conditions after spin-coating. (D) Dependence of height on radius for two types of capsules prepared either by dropcasting or spin-coating.

significant material loss, while highlighting the profound influence of surface charge on the final particle morphology and interfacial behavior. Additional characterization showing the buckling behavior of both types of capsules and pH, ionic and temperature responsiveness of charged capsules were shown in the main paper [96].

2.3.2 AFM analysis of Hollow Rod-Shaped Microgels

In order to gain insights into the mechanical properties and structural characteristics of swollen rod-shaped microgels, AFM measurements were performed in water. This approach provides unprecedented spatial resolution of mechanical properties across individual particles, enabling detailed mapping of local network density and structural heterogeneities that are not accessible through standard characterization methods. The microgels were adsorbed under dilute conditions onto glass slides that had been cleaned via sonication for 15 minutes in isopropanol. This preparation methodology ensures effective immobilization of microgels on the glass surface while minimizing aggregation and maintaining their individual character for single-particle analysis.

Subsequently, comprehensive stiffness tomography measurements were performed on core-shell and hollow microgels. The measurements were conducted using Peak Force QNM and Force Volume modes with modified MSNL-E cantilevers having nominal spring constants of 0.1 N/m and tip radii of 2 nm. The AFM tip was activated by oxygen plasma treatment immediately before measurements to ensure optimal surface chemistry and minimize adhesion artifacts. Temperature control was maintained at 27 °C throughout the experiments.

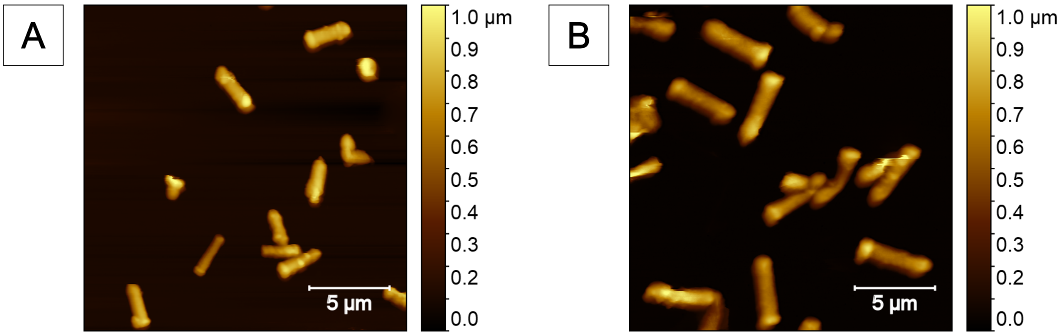

Fig. 2.7 AFM Height micrographs of microgel coated silica rods (A) and etched hollow microgel rods (B). The image size is 20 × 20 μ^2.

Initially, height images obtained by Peak Force Tapping (Fig. 2.7) show that microgels in their swollen state have a bullet shape that correlates with the TEM data (Fig. 2.2D). Then Force spectroscopy measurement of selected single microgels were done. In brief, all force-distance curves are baseline corrected. Then the contact point of each curve is defined, allowing the identification of part of the indentation and the correction of the height image. In the next step, the contact stiffness (the first derivative) of the force-indentation depth curves is determined. As sharp AFM probe is penetrating the porous polymer networks the local contact stiffness characterizes network density. Finally, the routine enables the visualization of the Force Volume data (Fig. 2.8).

These experiments revealed that both core-shell and hollow rod-shaped systems undergo substantial deformation when adsorbed at the solid substrate, fundamentally altering their morphology compared to their free-floating state in bulk solution. The extent of this deformation is evidenced by their pronounced lateral spreading on the order of 800 nm that exceeds their vertical height, which remains slightly below 600 nm at the midsection (Fig. 2.8A,C). The length of hollow rods was determined to be approximately 4 μm, significantly larger than that for core-shell structures, which measured around 3 μm (Fig. 2.8B,D). Interestingly, the rod length measured by AFM in the hydrated state remained systematically lower than the dimensions observed in TEM experiments (Fig. 2.2C,D).

Remarkably, hollow microgels display extraordinarily soft mechanical behavior due to the presence of their internal cavity, representing a striking difference from their core-shell precursors. The stiffness tomography measurements reveal that high contact stiffness values could not be achieved even with penetration depths exceeding several hundred nanometers: around 400 nm in the vertical direction for the hollow microgels in the center while less than 200 nm and stiffer profiles were measured for core-shell ones. This extreme soft behavior can be attributed to several factors: (i) the absence of the rigid silica core that

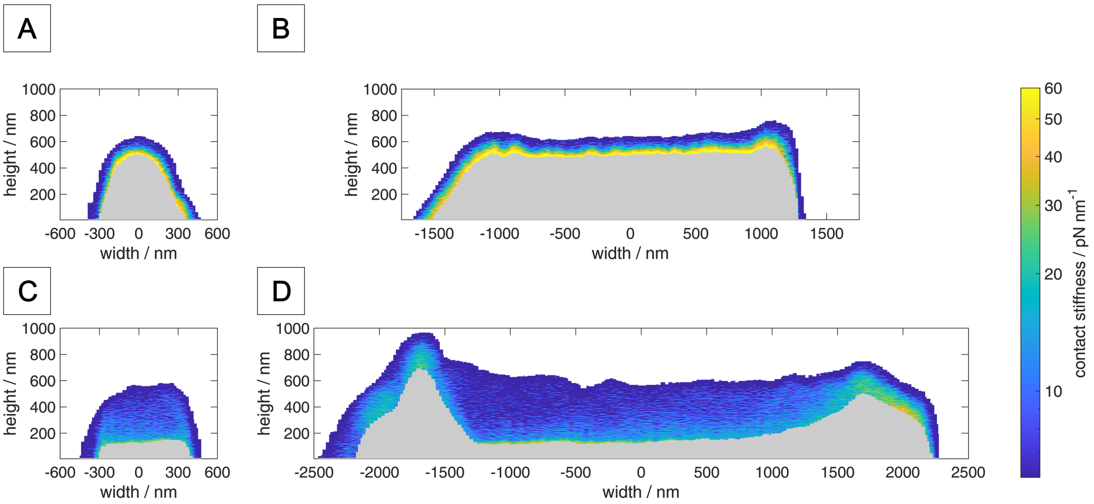

Fig. 2.8 Representative AFM stiffness tomography of microgel coated silica rods (A) and etched hollow microgel rods (B) adsorbed on a glass slide. Contact stiffness profiles along the minor and major axes. Grey areas in the images indicate regions inaccessible to the AFM tip (Force > 5 nN).

previously provided mechanical support, (ii) the hollow cavity that allows for substantial volume changes without geometric constraints.

However, as expected from the anisotropic particle geometry and synthesis history, the recorded stiffness exhibits significant spatial heterogeneity, with notably higher values observed at both particle extremities (tips) compared to the central region, while for hollow ones this effect is more prominent (Fig. 2.9A,B). This mechanical heterogeneity can be traced back to the templating synthesis process, where the growth of the microgel shell onto the silica rod surface depends critically on the local surface chemistry and geometry. During the initial coating with TPM, higher packing densities are achieved in curved areas due to decreased steric hindrance at the rounded segments of the template particles. The hemispherical tips and edges of the flat circular bases provide regions of high curvature where more TPM molecules can bind to the silica surface, resulting in locally denser microgel coatings, that is also observed by TEM experiments (Fig. 2.2D).

Additional characterization of these rod-shaped microgels that showed their potential for studying in situ phase transitions of rod-shaped model systems is described in the main paper [97].

2.3.3 AFM analysis of Capillary Self-Assembly of Anisotropic Microgels

AFM measurements were performed to directly test the mechanical properties of ellipsoidal microgels and investigate their assembly behavior after transfer from the air-water interface. This approach represents a crucial bridge between interfacial assembly studies and detailed

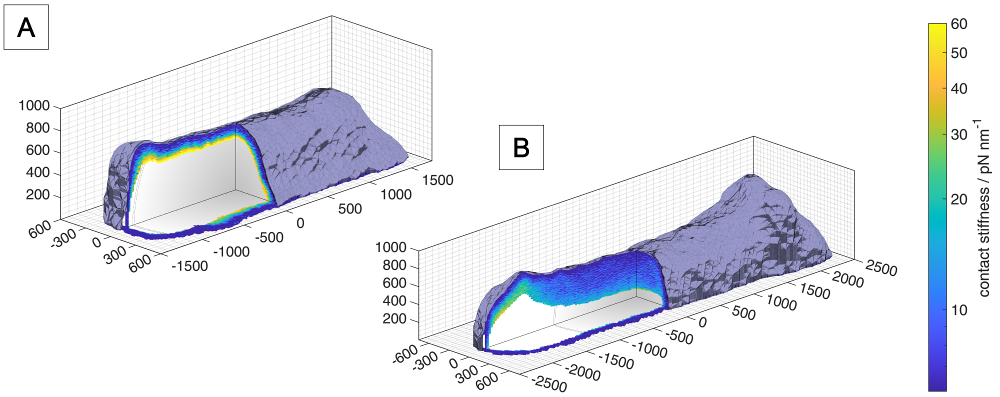

Fig. 2.9 Representative AFM stiffness tomography of microgel coated silica rods (A) and etched hollow microgel rods (B) adsorbed on a glass slide. 3*D* stiffness tomography of the two ellipsoidal systems with a cut-off of the contact stiffness map along halfs of the minor and major axes. Grey areas in the images indicate regions inaccessible to the AFM tip (Force > 5 nN).

single-particle characterization, enabling us to correlate capillary-driven organization with mechanical properties at the individual particle level.

The samples were transferred to glass slides via controlled dip-coating from the air-water interface using a custom-designed dip-coater that allowed precise control over withdrawal speed and angle. This transfer method was chosen over alternative approaches due to its ability to potentially preserve interfacial structures while enabling subsequent dry-state and aqueous AFM analysis.

Initially, broad areas illustrating the assembly patterns of microgels were measured in dried state in tapping mode. The corresponding AFM imaging results for the ellipsoids are shown in Fig. 2.10. The micrographs present completely different assembly patterns from those directly observed at the interface through fluorescence microscopy, indicating a fundamental limitation of the transfer process. When particles with $\lambda = 2.00$ showed clear side-by-side assembly with triangular junctions at the air-water interface, they now display predominantly triangular associations in the dried state (Fig. 2.10A). This represents a qualitative change in the dominant assembly motif, suggesting that the characteristic linear chains observed at the interface are not faithfully reproduced upon substrate transfer. Similarly, particles with $\lambda = 5.00$, which were characterized by long side-by-side stacks connected by occasional junctions at the interface, now appear as interconnected stacked domains where individual rods within the stacks are often tilted and misaligned (Fig. 2.10B).

This reorganization indicates that the dip-coating process cannot effectively "capture" or preserve the native interfacial structure, raising fundamental questions about the fidelity of transfer methods for soft colloidal systems. Most likely, additional immersion forces [98] are responsible for the reorganization of the ellipsoids during the dip-coating process. The discrepancy between interfacial and transferred structures is particularly spectacular

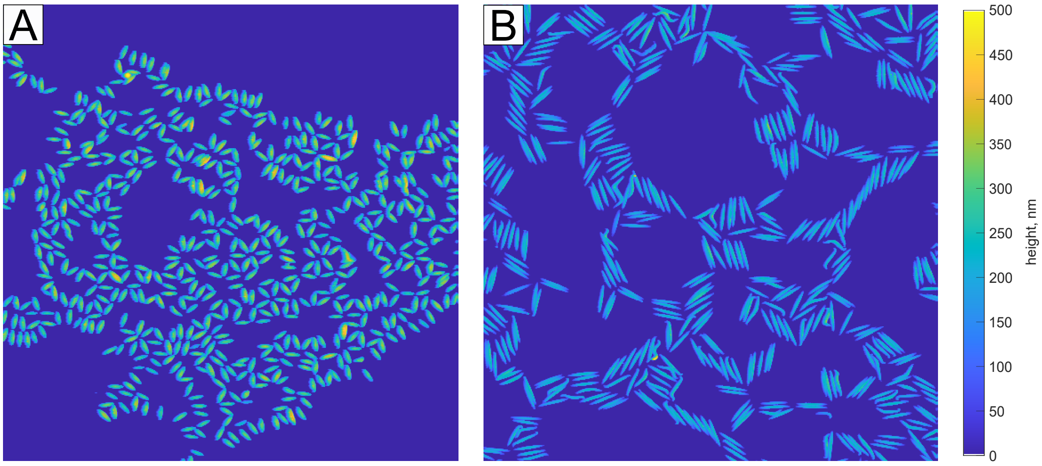

Fig. 2.10 Typical AFM micrographs of soft ellipsoidal microgels with λ = 2.00 and 5.00. (A,B) Height images in the dried state after dip-coating. Area size is 50 x 50 μm^2.

in our case because these systems already exhibit robust capillary interactions at the fluid interface, suggesting that even strongly bound assemblies may be susceptible to transfer-induced reorganization. This question should certainly be carefully addressed as it concerns many past and current studies on interfacial assembly, where it was assumed that deposited structures reflect the organization at the interface [31, 30, 81].

Despite the limitations of the transfer process for preserving assembly structure, stiffness tomography measurements were performed after re-hydration of the substrate to investigate the mechanical properties of individual microgels. Firstly, all force-distance curves are baseline corrected. Then the contact point of each curve is defined, allowing the identification of part of the indentation and the correction of the height image. In the next step, the contact stiffness (the first derivative) of the force-indentation depth curves is determined. As sharp AFM Finally, the visualization of the Force Volume data was done (Fig. 2.11).

Force spectroscopy data were extracted using Nanoscope Analysis 1.9 Software (Bruker Corporation) and processed using custom-made MATLAB scripts specifically developed for microgel force-distance curve analysis and contact stiffness calculations. All force-distance curves underwent systematic baseline correction and contact point determination using established algorithms adapted for soft microgel analysis. Contact points were identified using a combination of threshold detection and curve fitting methods to account for the gradual onset of repulsive forces characteristic of soft, deformable particles. The contact stiffness parameter, defined as the local derivative of force with respect to indentation depth (dF/dδ), was calculated to provide contact stiffness microgels profiles. The detailed data processing methodology, including contact stiffness profiles formulation, followed procedures outlined in previous publications [99].

Additionally, three-dimensional stiffness tomography of the two ellipsoidal systems (λ = 2.00 and 5.00) are shown in Fig. 2.11, providing detailed spatial maps of local

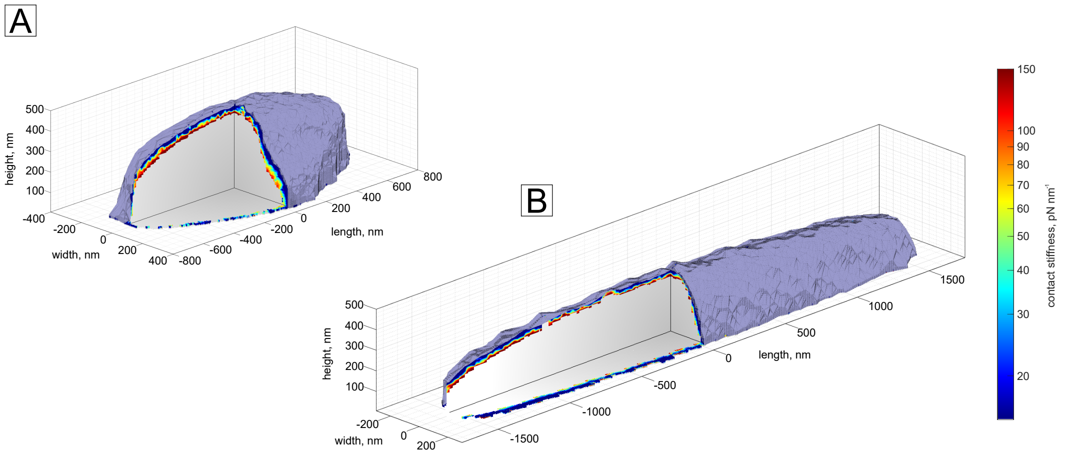

Fig. 2.11 Typical 3*D* stiffness tomography of the two ellipsoidal systems with λ = 2.00 (A) and 5.00 (B) a cut-off of the contact stiffness map. The grey color indicates an area that the cantilever tip cannot reach.

mechanical properties across individual particles. In the case of the highly elongated λ = 5.00 ellipsoids (Fig. 2.11B and Fig. 2.12C), the lateral deformation is not as evident from direct visualization of the topographical micrographs, suggesting that highly anisotropic particles may be more resistant to substrate-induced spreading. However, detailed analysis of the stiffness maps revealed that the lateral corona region appears significantly softer than the particle tips, a direct consequence of the uniaxial elongation process used to create these anisotropic particles.

This mechanical heterogeneity can be understood in terms of the synthesis history: during the uniaxial stretching process, the polymer shell experiences non-uniform deformation, with the central regions undergoing greater strain than the end caps. This differential deformation creates permanent structural changes in the polymer network, leading to regions of different density and corresponding mechanical properties.

Contact stiffness profiles following the short and long axes are provided in Fig. 2.12 for a spherical core-shell control and ellipsoids with λ = 2.00 and λ = 5.00 (Fig. 2.12A-C). The gray regions in these figures indicate areas that cannot be accessed by the AFM tip due to the 5 nN force threshold, providing insight into the local penetration depth and network density variations.

From analysis of contact stiffness profiles, the lateral deformation of the λ = 2.00 ellipsoidal microgel is clearly visible (Fig. 2.12B). The lateral spreading is evidenced by the asymmetric height profile and the corresponding changes in local mechanical properties, with softer regions appearing where the polymer shell has spread laterally. However, we observed that for some particles, such deformation was highly asymmetric, deviating from the expected symmetric spreading pattern. This asymmetry was particularly evident in some spherical particles (Fig. 2.12A). The interpretation of these results remains unclear as it is hard to separate possible local substrate heterogeneity due to sample preparation with the artifact of AFM measurement due to geometry of tip and direction of scanning. Just

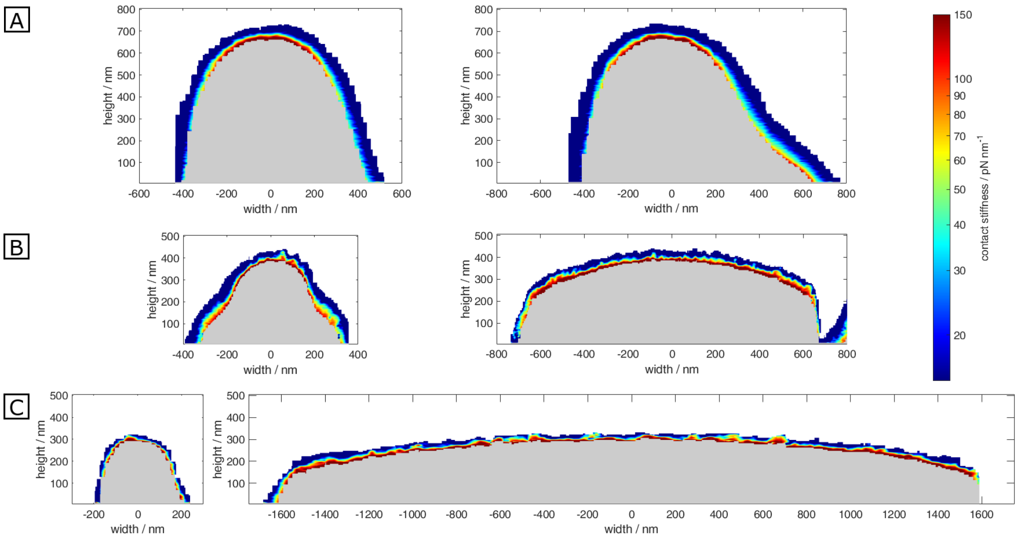

Fig. 2.12 Contact stiffness profiles of microgels after dip-coating deposition in water at 27 °C obtained by AFM along the short (left) and long (right) axis. The soft core-shell microgel (A) λ = 1.00, (B) λ = 2.00, (C) λ = 5.00.

could be notice the similar effect for spherical core-shell microgels from 2.3 Subsection. The different results are further reflected by the analysis of the contact area, which does not follow the large increase observed from the interfacial analysis.

Table 2.1 Microgel characterization results from AFM (Peak Force QNM mode): $2a$ - minor axis, $2b$ - major axis, h - height, ρ - b/a, A - contact area. The soft core-shell microgel with draw ratio of λ = 1.00, 2.00 and 5.00 are statistically analyzed of contact stiffness maps to get average values of dimensions and aspect ratios.

λ	$2a$ [nm]	$2b$ [nm]	h [nm]	ρ	A, nm^2
1.00	1200±60	960±40	720±30	1.25±0.05	847000±55000
2.00	1560±120	740±60	440±20	2.18±0.19	858000±99000
5.00	3200±120	440±30	340±20	7.23±0.50	1265000±60000

The main results of the AFM characterization are summarized in Table 2.1. The comparison of the full short axis and the height of the systems illustrates the soft character of the microgels and their flattening at the substrate. This analysis further confirms the lateral spreading of the ellipsoidal microgels. The aspect ratio of 2.18 determined for ρ = 2.00 is in line with the value of 2.04 determined from the analysis at the air-water interface. This is in stark contrast with ρ = 5.00, which appears significantly more anisotropic than at the water interface with ρ determined at 7.23 instead of 4.16. This observation indicates that such results should be handled with care as the drying and rehydration process may also influence the spreading of the microgel shell. The different results are further reflected by the analysis of the contact area, which does not follow the large increase observed from the interfacial analysis.

2.4 Discussion

This comprehensive AFM-based study of three distinct microgel architectures reveals the profound influence of internal structure on mechanical properties, deformation behavior, and interfacial assembly. The investigation demonstrates AFM's unique capabilities for characterizing soft materials across multiple environments while highlighting important methodological considerations for studying responsive colloids.

The characterization of hollow spherical microgels reveals dramatic structural transformations upon core dissolution that fundamentally alter particle behavior. The core-shell precursors maintain their structural integrity with thin polymer shells, but core removal leads to complete morphological reorganization in the dried state. The charge-dependent behavior provides crucial insights into electrostatic effects on soft particle deformation. Neutral hollow microgels maintain better structural integrity with heights around 20 nm, while charged systems spread to extreme thinness ($\approx$7 nm) due to intramolecular electrostatic repulsion and unfavorable substrate interactions.

The comparison between dropcasting and spin-coating preparation methods reveals the sensitivity of soft particles to processing conditions. Spin-coating produces more uniform morphologies by kinetically trapping non-equilibrium conformations, while dropcasting allows for quasi-equilibrium spreading. This finding correlate with observed previously behavior of the extreme soft microgels. For example, *Schulte et. al.* [55] showed that in case of ultra-low cross-linked microgels the sample preparation method could define the polymer network structure of adsorbed microgels. Spin-coated microgels remain pancake-like structure even after rehydration and cannot collapse as entire objects while *in situ* adsorbed microgels without drying proccess showed half-ellipsoidal shapes with a smooth surface similar to conventional microgels.

The investigation of rod-shaped microgels demonstrates how template geometry creates persistent mechanical heterogeneity even after template removal. The hollow rods exhibit extraordinary softness (penetration depths >400 nm) compared to their core-shell precursors (<200 nm), confirming the critical role of the rigid core in maintaining mechanical integrity. The preserved bullet shape in the swollen state indicates that the initial templating creates permanent topological constraints that survive core dissolution. The synthesis-induced mechanical heterogeneity, with stiffer tips and softer central regions, traces directly to the TPM coating process where curved template surfaces enable higher crosslink densities. This controlled heterogeneity represents an opportunity for designing particles with spatially varying properties that could influence assembly behavior or enable directional interactions.

The study of anisotropic microgel assembly reveals a critical limitation in transfer-based characterization methods. The dramatic reorganization observed between interfacial assembly patterns and substrate-bound structures questions the fundamental assumption that transfer methods faithfully preserve interfacial organization. Particles showing clear side-by-side assembly at the air-water interface reorganize into triangular associations upon dip-coating, indicating that immersion forces exceed the binding energies of capillary-assembled structures.

This finding could have broad implications for the soft matter community, where Langmuir-Blodgett and related transfer techniques are commonly assumed to preserve interfacial structures. The results suggest that even strongly bound assemblies of soft particles may be susceptible to transfer-induced reorganization, that could be especially important for anisotropic microgels .

The stiffness tomography measurements on transferred particles provide valuable single-particle mechanical data despite assembly reorganization. The aspect ratio measurements show reasonable agreement for moderately anisotropic particles (ρ = 2.00) but significant discrepancies for highly elongated systems (ρ = 5.00), suggesting that transfer artifacts become more pronounced with increasing anisotropy.

2.5 Conclusion

Throughout this study, AFM demonstrates exceptional versatility for characterizing soft materials. The ability to operate in both air and aqueous environments enables direct comparison of dried and hydrated states, providing more data for comparison. Peak Force QNM and force spectroscopy provide spatially resolved mechanical information that connects local network properties to macroscopic behavior. However, the results also highlight AFM's limitations. Tip convolution effects, substrate interactions create artifacts that must be carefully considered. The asymmetric deformation patterns observed in some particles likely result from substrate heterogeneity or measurement artifacts rather than intrinsic material properties, emphasizing the need for statistical analysis and additional characterization with other methods. As additional point, sample preparation significantly influences final particle morphology, with different methods (dropcasting, spin-coating, dip-coating) producing distinct outcomes. The choice of preparation method should align with research objectives.

Chapter 3

Adhesion Properties of Microgels at Solid Interfaces

3.1 Introduction

Microgels represent a unique class of soft colloidal particles that combine the responsiveness of hydrogels with the processability of rigid particles. Understanding microgel behavior at interfaces is critical because their deformability and stimuli-responsiveness fundamentally alter traditional particle-interface physics, enabling applications impossible with conventional rigid particles [3]. Microgel-interface interactions involve complex interplays between particle mechanics, surface chemistry, and environmental stimuli, determining performance in biomedical applications, advanced manufacturing, and smart materials systems. These findings establish that microgel deformability enables superior interface coverage compared to rigid particles, with mechanical properties remaining tunable through environmental stimuli.

The standard Hertz model effectively describes the interaction of elastic objects but assumes they do not interact with each other beyond mechanical contact. In reality, materials can exhibit attractive or repulsive surface interactions that lead to additional deformation. Several models—including Johnson-Kendall-Roberts (JKR) [100], Derjaguin-Muller-Toporov [101], and Maugis theory [102] — were developed to better describe adhesive contact mechanics. JKR theory provides a quantitative framework for understanding microgel adhesive contact behavior. The model balances elastic strain energy, surface energy, and external forces to predict equilibrium contact configurations, with particular relevance for deformable microgels where adhesive interactions dominate. For soft, compliant materials with high adhesion and large contact areas the JKR model is most appropriate [103].

Surface functionalization provides additional control over microgel-interface interactions. Hydrophobic surfaces promote stronger deformation and adhesion, while hydrophilic surfaces allow more reversible interactions [104, 105]. This tunability enables rational design of interface behavior for specific applications, from cell culture substrates requiring controlled mechanical properties to responsive coatings with switchable adhesion.

The principles governing microgel-surface interactions become particularly important when considering biological interfaces. While detailed microgel-cell interactions are covered in Chapters 4 and 5, understanding fundamental interactions with simplified biological model systems provides essential groundwork. Lipid vesicles and supported lipid bilayers (SLBs) serve as standard model systems for biological membranes.

3.2 Theoretical Background

3.2.1 Johnson-Kendall-Roberts theory and osmotic deswelling

Following the JKR framework, the adhesion of an elastic sphere on a non-deformable surface can be formulated using contact energy. For an elastic sphere with radius R interacting with a hard non-deformable substrate with adhesion energy W_{adh}, under zero load, the object adheres to the substrate and deforms, forming a neck at the contact line (Fig. 3.1). This represents the balance between the stored elastic energy limiting contact propagation and the adhesion energy favoring spreading at the substrate. The adhesion energy is given by:

$$W_{adh} = \frac{2Ea^3}{9\pi R^2(1-\nu^2)}, \tag{3.1}$$

where a is the contact radius, R is the particle radius, E is the Young's elastic modulus, F is the applied force, ν is Poisson's ratio. This equation demonstrates that the contact radius cubed is proportional to the particle radius squared when adhesion dominates.

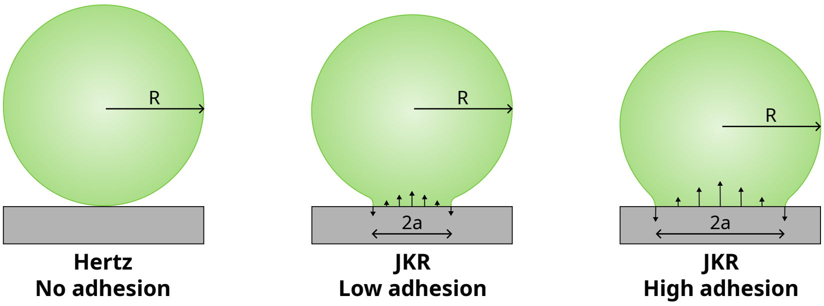

Fig. 3.1 Schematic illustration of contact mechanics for elastic spheres on rigid substrates.

Microgels bulk modulus could be determined through osmotic compressibility according to Eq. 3.2

$$K = -V \cdot dV/d\Pi, \tag{3.2}$$

where K is bulk modulus, V - volume of a microgel, Π - osmotic pressure

The osmotic pressure Π, which at the required concentrations are no longer following the Van 't Hoff law, can be calculated for dextran (150 kDa) [108] from the weight percentage β of the solution according to Eq. 3.3

$$\pi = 286\beta + 87\beta^2 + 5\beta^3, \tag{3.3}$$

Finally, the Young's modulus relates to bulk modulus via relations between moduli, according to Eq. 3.4

$$E = 3K(1 - 2\nu) \tag{3.4}$$

3.3 Materials and Methods

Synthesis of large microgels via microfluidics

pNIPAM microgels of approximate 40 μm in diameter were synthesized via droplet microfluidics. The synthesis procedure is based on the findings of Di Lorenzo and Seiffert [106]. A fluorinated oil phase (Novec 7500 and 1.8 wt% of the fluorinated surfactant Krytox) in combination with Tetramethylethylenediamine (2 vol%) was used as continuous phase. The water phase contained NIPAM (100 mg/mL), BIS (5 mol%), and APS (9 mg/mL) as the initiator. To obtain fluorescently labeled microgels, methacryloxyethyl thiocarbamoyl rhodamine B (<0.1 mol%) was added to the aqueous phase. The microgels were collected in a vial containing the oil phase plus paraffin oil and were allowed to polymerize overnight. For purification, the microgels were continuously washed with various organic solvents and finally transferred to cooled water.

Synthesis of hollow microgels

Hollow microgels were synthesized through a four-step process. First, silica template particles were grown to reach the target size of 1200 nm. Second, the silica particle surfaces were functionalized with vinyl groups. Third, these modified silica particles served as cores for the formation of core-shell microgels, where a microgel shell was polymerized around each particle. Finally, the silica cores were selectively dissolved using sodium hydroxide under mild conditions, yielding hollow microgel capsules [97].

Synthesis of hollow microgels

Small microgels were synthesized via precipitation polymerization [52]. NIPAM (5.45 g), BIS (0.34 g), and APMH (0.15 g) were dissolved in 330 mL of double-distilled water. The monomer solution was heated to 65 °C and purged with nitrogen under constant stirring (270 rpm). Simultaneously, V50 (0.2253 g) and cetrimonium bromide (CTAB) (0.0334 g) were each dissolved in 20 mL of water in separate vessels and degassed for 1 h. The surfactant was injected into the reaction vessel and stirred for 30 minutes to equilibrate before adding the initiator solution. The reaction proceeded for 4 h at 65 °CC under constant nitrogen flow and stirring. The microgels were purified by three cycles of ultracentrifugation at 30,000 rpm (70,000 RCF) with redispersion in fresh double-distilled water, then lyophilized for storage.

Substrate and sample preparation

Microgel adsorption was investigated on three different substrate types. All glass coverslips (2.2 × 2.2 cm, Menzel-Gläser, n4) were initially cleaned by sonication in isopropanol for 15 minutes. The three substrate preparations were:

- Isopropanol-cleaned glass: Coverslips were air-dried after cleaning and used directly.
- Plasma-activated glass: After isopropanol cleaning and air-drying, coverslips were surface-activated using a UV ozone cleaner (NanoBioAnalytics UVC 1014) for 15 minutes.
- Glass with supported lipid bilayers: Prepared as described in the following section.

All substrates were used immediately after preparation. For adsorption experiments, microgel solution was deposited on the glass surface and measurements were taken after 15 minutes of adsorption time.

Small unilamellar vesicles (SUVs) preparation

SUVs were prepared using a mini-extruder technique with the following steps: Lipid stock preparation: 1,2-dioleoyl-sn-glycero-3-phosphocholine (DOPC) lipid (0.0117 g, Avanti Polar Lipids) was dissolved in 3 mL of chloroform/methanol (9:1) to create a 5 mM stock solution. For fluorescent labeling, 21 μL of Lissamine Rhodamine PE dye stock (1.62 mg/mL in MilliQ water) was added to the DOPC solution. Lipid film formation: 200 μL of the lipid stock was transferred to a clean vial and solvents were evaporated under nitrogen flow. The dried lipid film was placed in a vacuum desiccator overnight to remove residual solvents. Hydration: The lipid film was hydrated with 1 mL MilliQ water and stirred for 1 hour at room temperature (25 °C), which is below the DOPC melting temperature (41 °C). Extrusion: The hydrated lipids were extruded 21-31 times through a 100 nm polycarbonate membrane using a mini-extruder to produce uniform SUVs (100 nm diameter). The resulting SUVs were stored at 4 °C for up to 3-4 days and their size was confirmed by dynamic light scattering.

Substrate and sample preparation

Adsorption of microgels were investigated on substrates with different preparation. First, all glass coverslips with the size of 2.2 x 2.2 cm (Menzel-Gläser, n4) were cleaned in an isopropanol chamber by sonicating it for 15 min. For the second surface group After that, the air-dried glass slide was activated by placing it inside the UV Ozone cleaner (NanoBioAnalztics UVC 1014) for 15 min. Glass were used immediately after preparation. for adsorption experiment microgels solution was dropped on the glass surface and measured after 15 min of adsorption.

Supported lipid bilayer formation

In the first step, coverslips were cleaned and sonicated in isopropanol for 15 min. In the second step, improvised chambers were prepared: 1) 2 mL reaction tube was cut with scissors and base of its cylindrical part was glued by the photocurable epoxy glue. After that, the glued side was placed on the previously cleaned coverslips as shown in Figure . Then, the prepared cell was placed inside a closed box under a high wavelength UV lamp for 30-40 minutes. In the last step, the prepared cell was plasma-cleaned for 3 min in a O2 plasma cleaner for glass surface activation.

SLBs formation was done via SUVs deposition. At first, x2 stock of the binding buffer solution (binding buffer: 25 mM Tris-HCl pH 7.5, 150 mM KCl, 5 mM MgCl2) was prepared. Subsequently, 40 μL of SUVs solution was mixed by adding it to 60 μL of H2O and 100 μL of binding buffer (x2) so that final concentration of SUVs becomes 1/5 of the initial concentration. Then, 100 μL of SUVs with buffer was added inside the chamber of the cell. It was rinsed with 2 ml of H2O by pipetting after the deposition time (5 min) to remove the excess vesicles. The gentle rinsing was performed several times and the final minimum volume of the solution was maintained about 200 μL inside the chamber to avoid the drying of the supported lipid bilayer [107].

Spinning disk fluorescence microscopy (SDFM)

The SDFM measurements were performed by using an inverted epifluorescence microscope (Nikon Ecplipse TI: HUBC/A). The microscope was equipped with a 100x oil immersion objective (Nikon HP Plan Apo VC, NA = 1.40) and a beam splitter (Semrock Di01-T405/488/568/647 quad-band dichroic mirror). SDFM was enabled by a spinning disk (Yokogawa CSU-X1FW) with a spinning frequency of 5000 rpm. A 561 nm laser (Toptica iBeam smart 488S-HP) with theoretical maximal power of 200 mW was used to excite FITC and a 561 nm laser (Cobolt Jive TEM) with theoretical maximal power of 500 mW was used to excite Rhodamine B. A xyz-piezo stage was used to move the measuring cells with the precision of a few nanometers. The micrographs were recorded with a EMCCD (Andor iXon Ultra) with 1024x1024 px, electron multiplier mode and a camera pixel size of 13 $\mu\ m \cdot\ px^{-1}$. The 100x magnification by the objective lens and an additional magnification of 1.2x causes a final image pixel size of 108.33 $nm \cdot px^{-1}$. %nm $\cdot\ px^{-1}$. The processing of the micrographs was performed with the software ImageJ.

Atomic force microscopy (AFM)

AFM measurements were performed on a Dimension Icon AFM with a closed loop (Veeco Instruments Inc., software Nanoscope 9.4, Bruker Corporation). For sample preparation, microgels were dispersed in water and applied to the functionalized glass slide using an *in situ* or spin-coating adsorption method.

Measurements were conducted in a customized liquid cell on a heating stage (Dimension Icon Electrochemistry Chuck, Bruker Corporation) with temperature control (Model 335 Cryogenic Temperature Controller, Lake Shore Cryotronics). The temperature was set to 27 °C and equilibrated for 60 minutes before measurements to ensure thermal stability. Contact stiffness measurements were carried out using the Peak Force QNM and Force Volume modes with modified MSNL-E (Bruker Corporation) tips. These tips have a nominal resonance frequency of 15 kHz in air and a nominal spring constant of 0.1 N/m, with a tip radius of 2 nm and a semi-angle of 23°. Immediately before measurements, the AFM tip was activated by oxygen plasma treatment (PVA TePla plasma system 100) with 1.4 mbar oxygen pressure at 200 W microwave power for 5 minutes to ensure clean and reproducible contact properties.

3.4 Results

3.4.1 Adhesion of microfluidic-synthesized microgels

To investigate microgel interactions with surfaces and their deformation, we applied contact mechanics analysis. Three surface types were tested to examine how surface chemistry affects microgel adhesion:

- Isopropanol-cleaned glass: Standard, relatively hydrophobic surface
- UV-ozone activated glass: More hydrophilic and negatively charged surface
- SLBs: Biomimetic surface simulating cellular membranes

Microgels were deposited on each surface and allowed to equilibrate for 15 minutes. For each surface type, 15-25 individual microgels were analyzed to ensure statistical reliability. The particle radius R remained constant across all measurements at 11.1 ± 0.3 μm, confirming that microgel population is monodispersed and the differences in contact area arise from substrate effects rather than particle size variations.

Spinning disk fluorescence microscopy images revealed systematic differences in microgel deformation depending on surface properties (Fig. 3.2A-C). The fluorescent labeling of the microgels allowed us to visualize both the three-dimensional particle shape and, crucially, the contact area with the substrate. Due to the relatively high hydrophobicity of isopropanol-cleaned glass, substantial deformation occurred, yielding an average contact radius of approximately 4.8 μm. However, after UV-ozone surface activation, deformation decreased significantly, with contact radii around 3.4 μm. The SLBs experiments showed similar trend with contact radii of approximately 2.8 μm.

The mechanical properties of the microgels were determined through osmotic deswelling experiments using dextran 150 kDa. The choice of this large molecular weight polymer is critical: dextran 150 kDa is too large to penetrate the microgel mesh. This approach allows

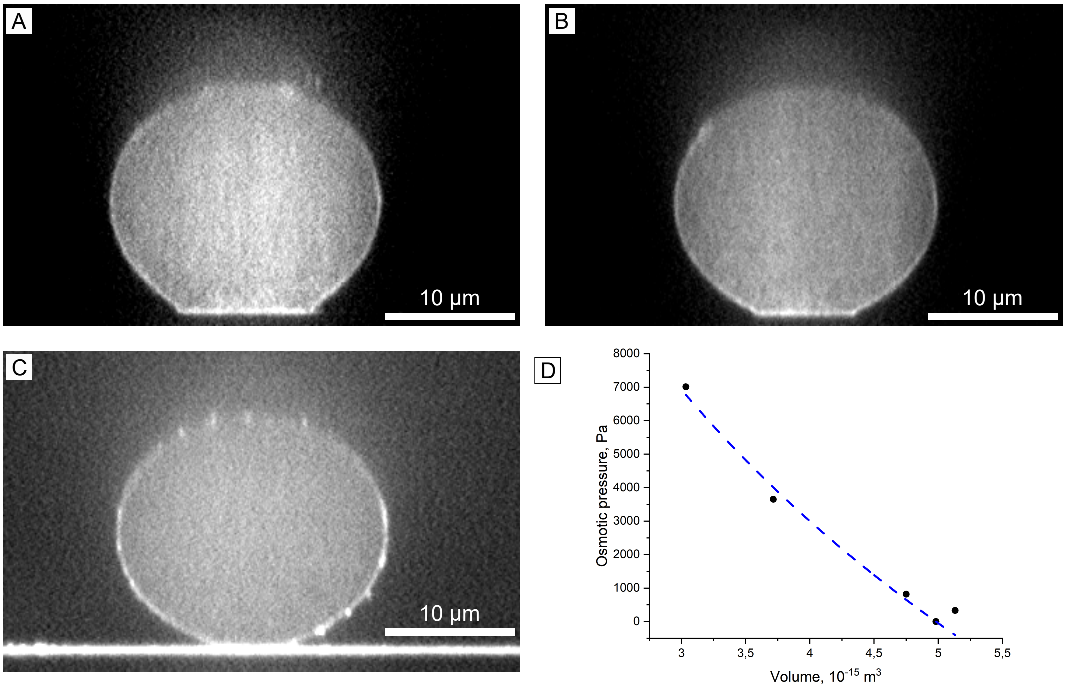

Fig. 3.2 Representative spinning disk microscopy images of microfluidic-synthesized microgels on different substrates: (A) isopropanol-cleaned glass, (B) UV-ozone activated, (C) supported lipid bilayers. Scale bar is 10 μm. (D) Osmotic deswelling experiments with dextran 150 kDa used to determine the bulk modulus of the microgels. Dashed line represents logarithm fitting.

us to probe the microgel as a homogeneous elastic body. The osmotic deswelling curves (Fig. 3.2D) show the relationship between osmotic pressure and microgel volume. The resulting data were analyzed according to the relationship between osmotic pressure and volume change to extract the bulk modulus. Considering bulk modulus constant in range of small deformation, the Eq. 3.2 could be solved as Eq. 3.5:

$$\Pi = -K(ln(V) - ln(V_0)), \tag{3.5}$$

These experiments yielded a bulk modulus of approximately 13.7 kPa. Assuming a Poisson's ratio of 0.38 for the microgels, we calculated the Young's modulus using Eq. 3.4 - 9.9 kPa. Using E adhesion energy was calculated for each surface type (Table 3.1). The adhesion energy W_{adh} represents the thermodynamic work required to separate the microgel from the substrate per unit area.

3.4.2 Adhesion of hollow microgels

To extend our investigation, we selected hollow microgels with a huge cavity (diameter of the silica core used for synthesis is 1200 nm). However, accurate measurement of the contact radius becomes problematic, mostly due to the low contact radius (Fig. 3.3) and the limitations of fluorescence microscopy accompanied with 108 nm pixel size of used camera.

Table 3.1 Adhesion properties of microfluidic-synthesized microgels on different substrates: isopropanol-cleaned glass, ozone/UV activated glass and SLBs. R is the microgel radius , a is a contact radius, and W_{adh} is an adhesion energy.

surface	R [μm]	a [μm]	W_{adh} [J/m^2 ($\times 10^{-4}$)]
isopropanol cleaned glass	11.1±0.3	4.8±0.6	7.3±1.7
ozone/UV activated glass	11.1±0.4	3.4±0.3	2.2±0.4
SLBs	11.1±0.3	2.8±0.3	1.2±0.3

In case of isopropanol-cleaned glass, hollow microgels easily adsorbed after 15 min and their deformation could be observed (Fig. 3.3A,B), while the accurate measurement is hard. In case of ozone/UV activated glass and SLBs after 30 min of incubation many microgels that did not attach on the surface were observed. That correlates with their shape that look like undeformed spheres (Fig. 3.3C,D).

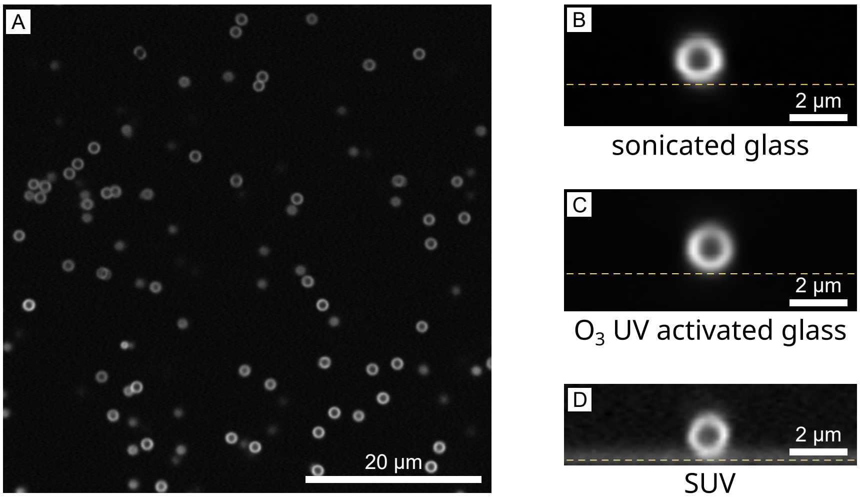

Fig. 3.3 (A) Overview image of hollow microgels adsorbed on the isopropanol-cleaned glass (scale bar: 20 μm). Typical images of individual hollow microgels on: (B) isopropanol-cleaned glass (B), UV-ozone activated glass (C), and supported lipid bilayers (D). Yellow dashed line indicates glass. Scale bars: 2 μm.

However, the deformation of this hollow microgels could be observed but with a different setup. Increasing of osmotic pressure via adding dextran or PEG will cause not the osmotic deswelling but the buckling due to the hollow structure of microgels [97]. In recent work, it was shown the buckling transitions was achieved at 8 *kPa* for dextran 150 kDa.

3.4.3 Adhesion of small microgels on SLBs

To overcome the spatial resolution limitations of fluorescence microscopy, we implemented atomic force microscopy (AFM) measurements. For these experiments, we utilized PNIPAM microgels with 5% cross-linker content (BIS) and 2% of cationic comonomer

N-(3-aminopropyl)methacrylamide hydrochloride (APMH). The experiments were done similar to previous Chapter 2. At first microgels we spin-coated at optimal concentration on ozone/UV activated glass slides and measured in water at 27 °. With Peak Force Tapping mode area of interests were found (Fig. 3.4A,C) and Force spectroscopy measurement were performed for selected individual microgels. Using custom Matlab script, contact stiffness profiles were obtained. For the SLB sample microgels solution was added to *in situ* adsorption (Fig. 3.4B,D).

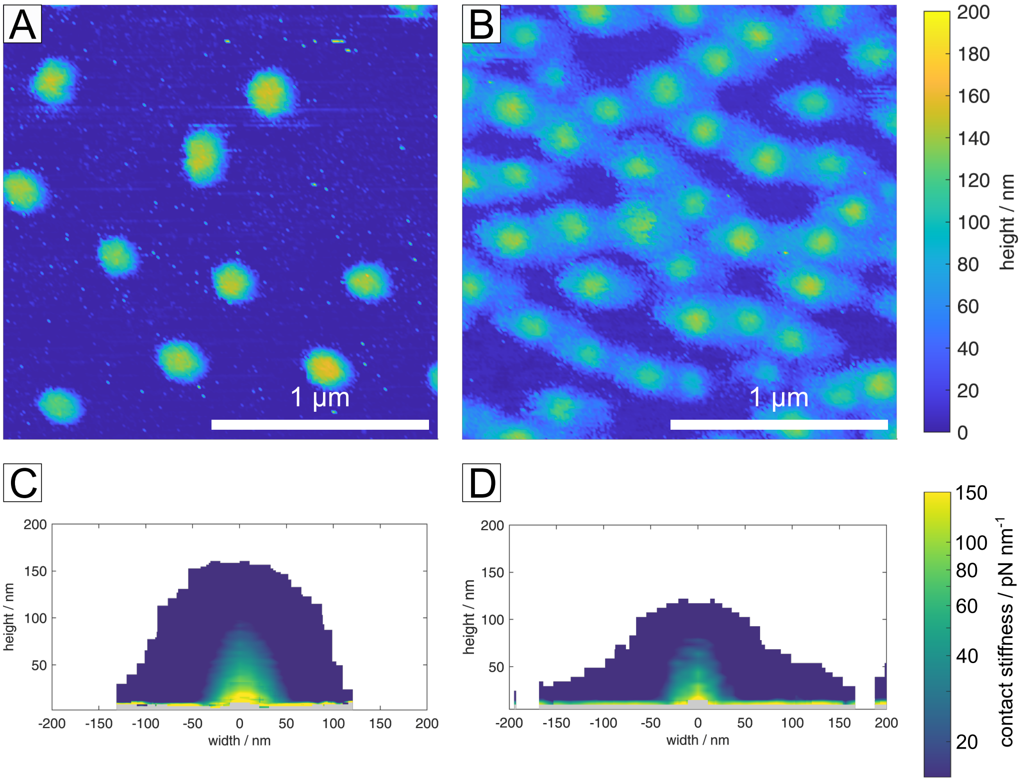

Fig. 3.4 Representative AFM height images of small positively charged 5% microgels deposited on glass (A) and SLBs (B). Scale bars: 1 μm. Averaged contact stiffness profiles through the center of the single microgel on glass (C) and SLBs (D). The color bar is 0-150 pN/nm. Microgels were measured in water at 27 °C.

The AFM experiments revealed extensive flattening of microgels on the SLBs substrate (Fig. 3.4B,D), most likely due to electrostatic interaction between negatively charged lipids and positively charged polymer network. Interestingly, we did not observe a similar degree of spreading in fluorescence images obtained for other small positively charged microgels. This discrepancy likely indicates that fluorescence microscopy cannot visualize the soft, low-density polymer shell due to its low polymer concentration and potentially non-uniform distribution of fluorescent dye within the microgel structure. In contrast, AFM measurements with a sharp tip provide the resolution necessary to detect these subtle structural features.

3.5 Discussion

The adsorption of microgels at solid-liquid and membrane interfaces is governed by a complex interplay of factors, including the chemical nature of both the microgel polymer network and the substrate, electrostatic interactions, and the mechanical properties of the microgels themselves.

One of the most important factors determining microgel adsorption and deformation is the interaction between the polymer chains constituting the microgel network and the surface. Previous studies have demonstrated that the surface chemistry plays a decisive role in the deformation of adsorbed microgels. Recent studies have demonstrated that surface hydrophobicity significantly influences microgel spreading behavior, with enhanced flattening observed on less hydrophilic substrates [104, 105]. *Alvarez et. al.* investigated the deformation of pNIPMAM microgels on hydrophilic and hydrophobic surfaces using super-resolution fluorescence microscopy and molecular dynamics simulations [104]. They showed that microgels deform more strongly on hydrophobic surfaces like n-octadecyltrimethoxysilane and trichloro(1H,1H,2H,2H-perfluorooctyl)silane compared to hydrophilic ones (PEG), which they attributed to the balance between surface tension effects and polymer-surface interactions. Our results with microfluidic-synthesized microgels corroborate these findings, showing a reduction in contact radius on more hydrophilic surfaces. The JKR model was used to describe adhesion properties of microgels at solid substrates and to extract the adhesion energy. This methodology provides clear results; however, further investigation under applied load conditions is warranted to validate the applicability of the theory to microgel deformation [103].

In the case of hollow microgels, insufficient adsorption prevented statistically robust measurements of microgel deformation. The low surface coverage precluded accurate quantitative characterization of particle flattening on the substrate. According to buckling experiments [97], this observation can be explained by the fact that hollow microgels undergo a buckling deformation transition at relatively high pressures, which may not be achieved during adsorption from bulk solution onto the surface. Furthermore, low adhesion energy prevented significant deformation for the majority of hollow microgels on hydrophilic activated glass and SLBs.

The significant advantage of AFM is its capability to characterize microgels that are below or near the resolution limit of conventional fluorescence microscopy. For small microgels, optical diffraction limits pose challenges for accurate size determination. However, this method is more complex and may provide an altered perspective of the microgel structure. For instance, the neck region at the bottom near the surface cannot be investigated properly due to the top-down approach of the tip. Our experiments with 5% small PNIPAM microgels revealed an additional difference in adsorption behavior on SLBs versus glass surfaces. Contrary to results obtained with large microgels, which exhibited less deformation on SLBs, small microgels demonstrated enhanced flattening, potentially attributable to interactions of the soft shell that may be undetected in fluorescence experiments due to low polymer density or absent in microfluidic-synthesized microgels.

These promising results motivated the investigation of anionic microgels, which are generally considered more suitable for biomedical applications due to their reduced cytotoxicity. Unfortunately, several anionic microgel studied in Chapter 4 did not adsorb onto the SLBs due to electrostatic repulsion between the negatively charged microgels and the negatively charged lipid bilayer.

3.6 Conclusions

Interaction of the microgel polymer network with the surface is one of the most important factors affecting deformation behavior. Using microfluidic-synthesized microgels, we demonstrated that hydrophilic surfaces lead to smaller contact areas during deformation, indicating lower adhesion energies. For large microfluidic microgels, fluorescence microscopy successfully enabled quantitative analysis of contact areas and application of JKR theory. In contrast, for small microgels approaching the optical resolution limit, AFM provided essential information about deformation that could not be obtained through fluorescence imaging. Further systematic studies of microgel-SLB interaction mechanisms could inform the rational design of soft microgels systems for drug delivery and other biomedical applications.

Chapter 4

Size and softness synergy in cellular microgel uptake: a force spectroscopy study

4.1 Introduction

In recent decades, nanomaterials have emerged as promising candidates for biomedical applications [109]. These materials, from metallic nanoparticles (NPs) to polymeric carriers, have improved conventional disease treatments by enabling targeted delivery, controlled release, and enhanced therapeutic efficacy. Among the diverse array of nanocarriers, microgels form a unique class. These aqueous cross-linked polymeric particles with tunable size, easy to functionalize porous networks allowing encapsulation, and excellent biocompatibility emerge as versatile platforms for drug delivery [110, 111, 15, 112, 16–18].

To optimize nanomaterial-based delivery systems, rational design requires consideration of multiple parameters. Key considerations include specificity to target tissues, delivery efficiency, and minimization of side effects. These factors are intimately linked to the physicochemical properties of the carriers [113, 114]. The ability to tune such properties has advanced targeted drug delivery, yet there is still a lack of comprehensive understanding of how carrier properties influence their therapeutic efficacy [115].

Previous studies investigating the effect of particle size on cellular uptake have predominantly focused on relatively small NPs < 500 nm in diameter. Due to steric limitations, NPs size often dictates the uptake pathway, generally leading to reduced internalization of larger particles [116]. Most of them are internalized via endocytotic pathways like clathrin-mediated and caveolae-mediated endocytosis [117, 118]. However, this size dependency is not always straightforward – it was demonstrated that extremely small 13 nm gold NPs showed decreased cellular uptake compared to 45 nm gold NPs [119]. Another interesting observation is the synergy of nanoparticles of different sizes on their cellular internalization [120]. It was shown that larger NPs with 100 nm diameter promoted the uptake of 50 nm ones and and vice versa.

Beyond size considerations, particle mechanical properties have emerged as equally critical factors. While size effects are important, particle stiffness has also emerged as a critical parameter influencing cellular uptake [121]. However, the interpretation of the results is complicated due to different cell lines and nature of NPs used in the experiment. Studies have shown that stiffer particles generally demonstrate enhanced uptake by macrophages [122, 123]. For instance, studies with 300 nm gelatin NPs revealed that stiffer particles showed better internalization by dTHP1 and RAW 264.7 macrophages [124].

The reduced uptake of softer particles has been attributed to their ability to deform during the internalization process, which may either complicate membrane passage or determine the endocytotic pathway [125, 126]. At the same time, soft lysozyme-dextran NPs demonstrated deformability, which allowed them to penetrate caveolae sterically inaccessible to hard particles of the same size [127].

While in addition to size and stiffness, other parameters such as surface chemistry, charge, and functional groups influence uptake, our present study focuses on the influence of particle softness and the influence of charges warrant separate investigations [128, 129, 114].

In addition to NPs, microgels represent a distinct and promising class of delivery vehicles that offer several advantages over traditional NPs. These soft, hydrogel-based particles combine the benefits of both hydrogels and colloidal systems, exhibiting exceptional biocompatibility due to their high water content and polymeric nature [130]. Incorporation of different monomers during or post-synthesis allows tailoring pH-, light- or temperature-sensitive properties, adding to their versatility. Moreover, their inherent softness and deformability set them apart from rigid nanoparticles discussed above, potentially enabling unique cellular interaction mechanisms.

Our current knowledge reveals that similarly to rigid nanoparticles, microgel softness and size play a significant role in cellular internalization. Banquy *et al.* demonstrated that the softness of microgels determines their internalization pathway when exposed to macrophages RAW 264.7 [131]. They investigated N,N-diethyl acrylamide and 2-hydroxyethyl methacrylate microgels (90% and 10% respectively) featuring cross-linking densities ranging from 1.7 to 15 mol% and diameters of 150–180 nm. Microgels with lower Young's moduli were internalized through macropinocytosis, while the stiffer ones were taken up via clathrin-mediated endocytosis.

In our previous study, we further illustrated that HEK293T cells take up poly(N-isopropylacrylamide) (PNIPAM)-based microgels within seconds to minutes [132]. Notably, small microgels with 5% and 15% cross-linking density were internalized, and remarkably, with 5% cross-linker content, even microgels with 1 μm diameter were taken up by cells - a size regime where rigid nanoparticles typically show no cellular entry. However, 1 μm size microgels with cross-linking contents of 10–15% did not penetrate the cells, suggesting a complex interplay between size and softness in determining cellular uptake.

In addition to microgels prepared with a dedicated cross-linker, PNIPAM can be synthesized without the addition of a cross-linking agent. Instead, the network forms through self-cross-linking of NIPAM due to transfer reactions [44–46]. The application of these ultra-low cross-linked (ULC) microgels is particularly intriguing due to their remarkably soft properties, which result in diverse behaviors during adsorption and deformation, thus expanding their potential for biological applications [133, 134]. For example, Nellenbach et al. utilized them to mimic platelets [135]. To enhance their blood-clotting function, the authors also modified ULC microgels with anti-fibrin antibodies, reducing the hydrodynamic radius from 1.5 μm to 0.5-0.8 μm. Interestingly, these modified microgels were not internalized by RAW 264.7 cells, but were predominantly observed on the extracellular surface of the cellular membrane.

Given these complex relationships between nanocarrier properties and cellular interactions, precise characterization of microgel mechanical properties is essential for creating designer nanomaterial. Atomic force microscopy (AFM) has emerged as a powerful tool that can be used for elasticity measurements [92], nanorheology [93] and other kinds of soft matter characterization [90, 91]. Force spectroscopy measurements with sharp tip offer nanoscale resolution enabling direct measurement of individual particle properties [136] under physiologically relevant conditions.

Our aim in this work was to employ AFM to investigate the correlation between microgel mechanical properties and their cellular uptake behavior, using HEK293T cells as our model system. These immortalized human embryonic kidney cells combine the practical advantages of an established cell line with behavior more representative of normal human cells compared to cancer-derived lines like (e.g. HeLa). Understanding these relationships will not only advance our fundamental knowledge of soft particle-cell interactions, but also guide the rational design of microgel-based drug delivery systems.

4.2 Materials and Methods

Microgel Synthesis

All conventional microgels were synthesized via precipitation polymerization. The main monomer N-isopropylacrylamide, N,N'-Methylenbis(acrylamide) as a cross-linker, and methacrylic acid as a comonomer, were dissolved in degassed water and introduced into a three-neck round-bottom flask equipped with a mechanical stirrer, reflux condenser, and N_2 inlet. Methacryloxyethyl thiocarbamoyl rhodamine B (MRB) was dissolved in degassed water via sonication and was added to the reaction mixture. Depending on the targeted size, the stirring speed and temperature were set to reaction conditions under $\mathrm{N_2}$ atmosphere.

The reaction was started by adding previously dissolved initiator potassium persulfate to the reaction flask and let to proceed for 4 hours, if not stated otherwise. The reaction mixture was filtrated via glass wool and cooled down to room temperature. Purification was achieved either by three sets of centrifugation and replacement of the supernatant with double-distilled water (for large microgels) or by dialysis (for small microgels). The microgels were lyophilized for storage. See Table 4.1 for additional information.

Table 4.1 Composition of cross-linked microgels. N-isopropylacrylamide (NIPAM) is the main monomer, with methacrylic acid (MAA) as comonomer. N,N'-Methylenebisacrylamide (BIS) served as the cross-linker at varying concentrations, while potassium persulfate (KPS) was used as the thermal initiator. Methacryloxyethyl thiocarbamoyl rhodamine B (MRB) was incorporated as a fluorescent comonomer for tracking purposes. The sample codes indicate the cross-linker content, with concentrations and other parameters detailed in the table. For S15% and L15% the addition of components was performed in a two-step process that marked with (I) and (II). *For L-ULC microgels 0.19 g of acrylic acid (5 mol%) was used instead of MAA.

Paper sample code	S5%	S15%	L5%	L10%	L12%	L15%	L-ULC*
Labjournal sample code	KG-08	KG-11	ST-VO-15	ST-VO-22	ST-VO-16	ST-VO-26	AF-04
NIPAM, g	18.0	0.96 (I) 1.4 (II)	3.8	3.4	3.8	1.3 (I) 1.9 (II)	5.6
MAA, g	1.0	0.062 (I) 0.094 (II)	0.12	0.15	0.15	0.060 (I) 0.090 (II)	0.19
(mol%)	(6)	(8)	(5)	(5)	(4)	(5)	(5)
BIS, g	1.0	0.090 (I) 0.36 (II)	0.28	0.53	0.82	0.16 (I) 0.65 (II)	-
(mol%)	(5)	(15)	(5)	(10)	(12)	(15)	
MRB, g	0.021	0.0016	0.0007	0.0023	0.0007	0.0023	0.0056
SDS, g	1.85	0.11	-	-	-	-	-
KPS, g	0.48	0.071	0.20	0.14	0.20	0.068	0.030
H_2O, ml	1000	130 (I) 20 (II)	250	250	250	200 (I) 50 (II)	250
t, °C	85	80	80	85	80	70	80
Purification	Centrifugation	Centrifugation	Dialysis	Centrifugation	Centrifugation	Centrifugation	Dialysis, Centrifugation

Sample preparation

The freeze-dried microgels were redispersed in water. Microscope slides were cleaned by ultrasonication in isopropanol, then the surface was activated in an ozone oven for 15 minutes. Subsequently, they were coated with polyallylamine hydrochloride (PAH). The samples were then dispensed onto the glass slides and processed either by spin-coating or by *in situ adsorption* at appropriate concentration. For the spin-coating, 120 μL of the mixed microgels solution was dropped onto the glass slide and it was rotated at a speed of 2500 rpm for 30 seconds. For the *in situ* adsorption 120 μL of the mixed microgel solution was applied to a glass slide and left for 1 hour to allow for adsorption. Subsequently, the slide was rinsed several times with 2 mL of Ringer's solution to remove any unabsorbed microgels.

Atomic force microscopy (AFM)

Measurements were performed on a Dimension Icon AFM with a closed-loop (Veeco Instruments Inc., software Nanoscope 9.4 (Bruker Corporation)). The measurements were recorded in the Peak Force QNM mode at 27 °C in Ringer's solution, using MSNL-10-E tip (Bruker) with a nominal resonance frequency of 38 kHz in air and a nominal spring constant of 0.1 N/m (radius: 2 nm, semi angle of the tip: 23°, assumed sample Poisson's ratio 0.3). Acquired data was processed using Nanoscope Analysis and a custom-made MATLAB script [99]. More information can be found in the AFM subsection. Ringer's solution: in mM: 145 NaCl, 10 HEPES, 5 KCl, 1 $CaCl_2$, 1 $MgCl_2$, pH 7.3, osmolarity 300 mOsm.

Cell culture

All experiments were conducted with Human Embryonic Kidney 293T cells (HEK293T cells) (ACC 635, DSMZ, Germany). Cells were cultivated in T75 flasks (Sarstedt AG, Germany) in a cell culture medium, consisting of Dulbecco's Modified Eagle Medium/Ham's Nutrient Mix F-12 + GlutaMAX (DMEM/F-12 + GlutaMAX; Gibco by Life Technologies, Thermo Fisher Scientific, USA) supplemented with 10% fetal bovine serum (FBS; Gibco by Life Technologies, Thermo Fisher Scientific, USA) and 1% penicillin and streptomycin (Pen/Strep; Gibco by Life Technologies, Thermo Fisher Scientific, USA) in humidified atmosphere. For all experiments, cells were used at least 2 days after passaging to ensure proper adherence and habituation of the cells.

Confocal Live-Cell Imaging of Microgel Uptake

Measurements were carried out using an inverted confocal laser scanning microscope (Leica TCS SP8) with HC PL APO 86x NA 1.20 water objective. Imaging was performed at 22 °C. For the internalization kinetics, it was done as following. After recording the baseline fluorescence signal, the microgel solution (0.5 mg/mL) was added and rate of uptake was measured over time. We tested concentrations in the range 0.16 to 1.5 g/L, showing the same general behavior. When low microgel concentrations were used, for S5% microgels complete uptake into cells was observed indicating that the limit of uptake was not reached. At the same time, ULC microgels at low concentrations produced insufficient fluorescent signal due to their extremely low density. Across all microgel types, 0.5 mg/mL was found to be optimal as it provides sufficient fluorescence signal, and saturation of microgel uptake is reached. Cells were imaged for 90 min at 1 frame/min, resulting in a total observation time of 1 h. Subsequently, using FIJI, the cell area excluding the nucleus was segmented for each cell, and the rate of relative fluorescence change (dF/F_0) was fitted using an exponential function with a characteristic time τ [132].

For investigation of microgels distribution after internalization, additional STimulated Emission Depletion (STED) microscopy module (Leica TCS STED X) was used with

775 nm pulsed STED laser. Nuclei and cell membrane were stained using a dye mixture of Hoechst 33342 and CellBrite. Immediately after internalization, the staining solution was washed in and incubated for 15 min at 37 °C. Using the UV-light (Hoechst 33342), 488 nm (CellBrite), 552 nm (rhodamine B) laser lines, the distribution of microgels was recorded.

Dynamic light scattering (DLS)

Microgels were measured in Ringer's solution at high dilution to prevent multiple scattering. The DLS measurements were conducted using an ALV goniometer setup equipped with a HeNe laser (λ = 633 nm), goniometer (ALV/CGS-8F), two avalanche photodiodes (PerkinElmer Inc. SPCM-CD2969), a digital hardware correlator (ALV 5000) and light scattering electronic (ALV/LSE-5003). A thermal bath filled with toluene was used to match the refractive index of the glass cuvettes. Temperature was controlled using a programmable thermostat. Measurements were performed at scattering angles from 30° to 110° in 10° increments. The initial decay rate Γ was derived from a first-order cumulant analysis of the normalized intermediate scattering function $f(q,t)$. The diffusion coefficient D was estimated from the q^2-dependence $\Gamma = Dq^2$, and the hydrodynamic radius R_{hyd} was obtained via the Stokes–Einstein relationship $D = k_B T/(6\pi\eta_s R_{hyd})$, where k_B, η_s, and T are the Boltzmann constant, solvent viscosity, and absolute temperature, respectively [137].

Static light scattering (SLS)

Microgels were measured at 20 °C in Ringer's solution and were highly diluted to prevent multiple scattering. A temperature-regulated sample chamber within a closed goniometer manufactured by SLS-Systemtechnik GmbH was used. Measurements were conducted at a fixed wavelength of 640 nm with a range of 10° to 60° scattering angle using 1° increments. The data underwent background correction by subtracting buffer (solvent) scattering contributions. Intensity standardization was performed using toluene as a reference scattering material. Analysis of the SLS data was performed using MatLab-based FitIt! Software with fuzzy sphere and fuzzy sphere core shell models [138, 139].

4.3 Results and Discussion

In this chapter, we investigated the relationship between microgel mechanical properties and cellular uptake behavior using AFM. We based our investigation on a well-characterized set of microgels that demonstrated varying cellular internalization behaviors in our previous work [132].

4.3.1 Microgel Characterization

We used small and large PNIPAM microgels co-polymerized with MAA with different concentrations of cross-linker. The incorporation of methacrylic acid as a copolymer not only enhances colloidal stability in the presence of salt but also imparts pH sensitivity, presenting potential advantages for the design of delivery agents [24].

Table 4.2 Overview of the microgels used in this study, where α_{max} is the swelling ratio, R_{hyd} is hydrodymanic radius and El. mob is electrophoretic mobility.

Paper sample code	Cross-linker, mol %	MAA, mol %	α_{max}	R_{hyd}(27 °C), nm	El. mob. 10^{-8} $m^2/(Vs)$
L5%	5	5	2.5	427	-0.29
L10%	10	5	1.9	501	-0.27
L12%	12	4	1.9	495	-0.51
L15%	15	5	3	463	-0.27
S5%	5	6	1.5	98	-0.44
S15%	15	8	2.3	127	-0.46

The microgels were synthesized in two size ranges - small (S) and large (L) - with cross-linker concentrations varying from 5% to 15% (Table 4.2). The MAA concentration was selected at approximately 5% (for S15% is slightly higher - 8%). The cross-linker content and MAA concentration are given as molar percentage (mol%) used during synthesis. Initially, the hydrodynamic radius (R_{hyd}) and electrophoretic mobility were measured in Ringer's solution.

For an additional characterization of microgels softness, the maximum swelling ratios α_{max} were measured. The maximum swelling ratio is defined as the ratio between the hydrodynamic radii measured in maximum swollen (low temperature and charged network) and collapsed (large temperature and uncharged network) states. Due to the presence of MAA, maximum swelling was achieved at pH 9 and 20 °C, while maximum deswelling occurred at pH 3 and 50 °C. These measurements already demonstrate that microgels with higher cross-linker content exhibit smaller swelling ratios.

However, the behavior of microgels in Ringer's solution differs from these extreme conditions due to the buffer's osmotic pressure and the charged polymer network at neutral pH (7.3). As shown in Figure 4.1, the temperature-dependent swelling behavior is less prominent, particularly for microgels with high cross-linker content. For large microgels with 5% of cross-linker content, the softer networks still exhibit the characteristic S-shaped temperature response, reaching a plateau at both low and high temperatures with $\alpha = 1.8$. In contrast, large microgels with 12% of cross-linker content show only a slight decrease in size without the S-shaped curve, with $\alpha = 1.2$, indicating their limited responsiveness under physiological conditions.

Throughout this chapter, samples are designated by size (S/L) followed by molar cross-linker percentage, used during synthesis (e.g., S5% indicates small microgels with 5% cross-linker density).

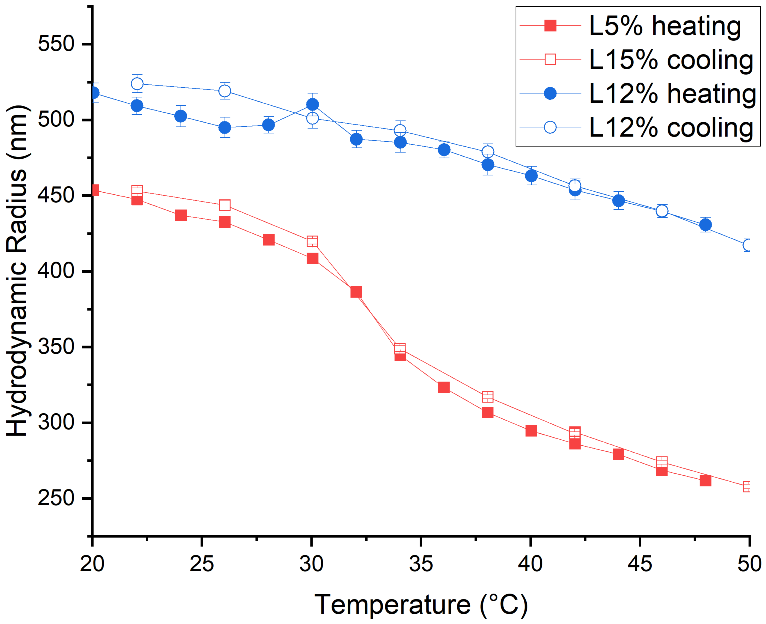

Fig. 4.1 Temperature-dependent DLS measurement of L5% (red) and L12% (blue) in Ringer's solution. The microgel solutions were sequentially heated and cooled.

4.3.2 Confocal live-cell imaging of microgel uptake in HEK293T cells

Previous work revealed a strong dependence of cellular uptake on both microgel size and cross-linking density [132]. In brief, changes in cellular fluorescence intensity ($\Delta F/F_0$) were observed during microgel exposure. Within one hour of microgel exposure, microgel uptake exhibited saturation kinetics in most cells, corresponding to maximum microgel capacity within the experiments. By fitting a monoexponential function to each cell's relative fluorescence intensity profile (Eq. 4.1), the time constant τ was introduced as a quantitative measure of relative cellular uptake kinetics.

$$y(t) = A \times e^{-(t-t_0)/\tau} + C, \tag{4.1}$$

The median time constants are presented in Table 4.3. Small microgels (S5% and S15%) were readily internalized by HEK293T cells, with S5% showing the fastest uptake kinetics. Among larger microgels, only those with the lowest cross-linking density (L5%) achieved cellular entry, albeit at a slower rate than their smaller counterparts. Large microgels with cross-linker content above 10% were not internalized within the experimental timeframe.

To expand these results and establish standardized experimental conditions, we first determined the optimal microgel concentration for cell uptake experiments by considering two parameters. The first parameter that controls the microgel concentration is the internalization kinetics. Experiments show that for S5% microgels at low concentrations

Table 4.3 Overview of the median characteristic times of internalization in seconds

Sample code	S5%	S15%	L5%	L10%, L12%, L15%
median time, s	732	1089	1610	no uptake

(0.16 g/L), fast cellular uptake was observed, indicating that the uptake saturation limit had not been reached under these conditions (Fig. 4.2).

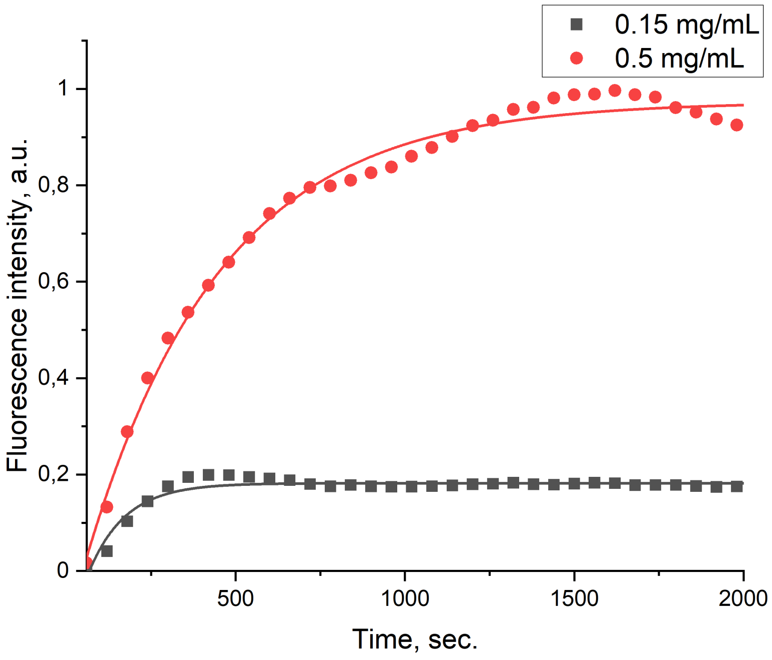

Fig. 4.2 Representative average kinetics of the increase in fluorescence within the cytoplasm of cells for S5% microgels at 0.15 (black) and 0.5 (red) mg/mL.

The second parameter is ensuring sufficient fluorescence signal for reliable quantitative analysis. Using high laser intensity to compensate for weak signals could be cytotoxic to cells and also lead to photobleaching of fluorophores, compromising data quality. This consideration dictates the minimum concentration requirements, particularly for ULC microgels due to their extremely low network density and correspondingly reduced fluorophore content per particle (Fig. 4.3C,D).

Balancing these two parameters across all microgel formulations, a concentration of 0.5 mg/mL was identified as optimal, providing sufficient fluorescence signal while ensuring saturation of microgel uptake for comparative studies between different cross-linker contents and softness properties.

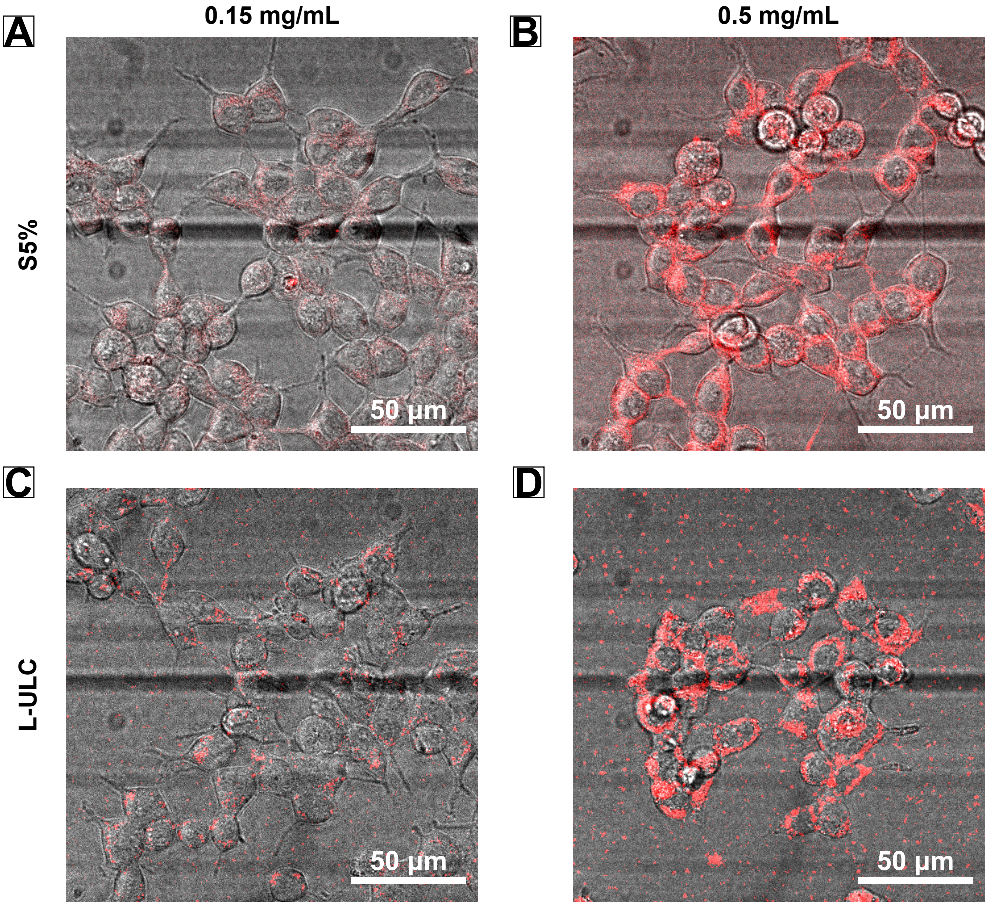

Fig. 4.3 Confocal live-cell imaging of microgel uptake in HEK293T cells after 30 min. Merged images show brightfield (gray) and microgel channel (red). (A) S5% microgels at 0.15 mg/mL; (B) S5% microgels at 0.5 mg/mL; (C) L-ULC microgels at 0.15 mg/mL; (D) L-ULC microgels at 0.5 mg/mL. Scale bar = 50 μm. The contrast of the microgel channel was kept consistent within each microgel type (A-B and C-D) to enable direct comparison of concentration effects.

4.3.3 AFM measurements of microgels in buffer

These distinct patterns of cellular uptake suggested a complex relationship between microgel mechanical properties and their ability to enter cells. To elucidate this relationship, we employed atomic force microscopy (AFM), which allows precise characterization of mechanical properties at the single-particle level under physiologically relevant conditions.

AFM measurements were performed using a Dimension Icon AFM equipped with a closed-loop scanner (Veeco Instruments Inc., software Nanoscope 9.4, Bruker Corporation). All investigations at the solid/liquid interface were conducted in a customized liquid cell mounted on a heating stage (Dimension Icon Electrochemistry Chuck, Bruker Corporation) with precise temperature control (Model 335 Cryogenic Temperature Controller, Lake Shore Cryotronics).

To replicate the extracellular environment, all measurements were conducted in Ringer's solution, maintaining physiological ionic strength and pH (7.3). The temperature was equilibrated at 27 °C for 60 minutes before each measurement session to ensure thermal stability throughout the system. Although this temperature is slightly elevated compared to the 22 °C used in cellular experiments, both temperatures remain well below the volume phase transition temperature (VPTT), that is 32 °C of the PNIPAM-based microgels, ensuring comparable swelling states. Substrates were kept continuously submerged in aqueous solution throughout the entire experimental process to prevent drying artifacts that could alter microgel morphology.

For each individual cantilever used, a standardized preparation and calibration protocol was followed to ensure measurement consistency and minimize systematic errors. Prior to each measurement session, AFM tips were activated by oxygen plasma treatment (PVA TePla plasma system 100) using 1.4 mbar oxygen pressure at 200W microwave power for 5 minutes. This activation renders the tip surface hydrophilic and removes organic contaminants, thereby reducing unwanted adhesion between microgels and the cantilever tip during measurements. Immediately following activation, the tip was used for AFM measurements to maintain optimal surface properties.

Cantilever calibration was performed using a two-step process. First, force-spectroscopy measurements on the bare PAH-coated glass substrate were conducted to determine the cantilever deflection sensitivity from the slope of the linear portion of the deflection-distance curve after the contact point. The tip was then withdrawn from the surface, and thermal noise measurements were performed using the thermal tune function of the Nanoscope software to determine the actual cantilever spring constant via the equipartition theorem. Typical sensitivity values ranged from 60-75 nm/V and spring constants from 0.08-0.12 N/m across different cantilevers, with variations attributed to manufacturing tolerances.

The measurement protocol consisted of two sequential steps designed to optimize both imaging quality and force spectroscopy data acquisition. Initially, characterization was performed using Peak Force QNM mode to assess microgel distribution on the substrate and identify regions of interest for detailed mechanical analysis (Fig. 4.4). The integrated ScanAsyst function was used to automatically optimize feedback parameters, including z-limit control, ensuring stable imaging conditions for the soft microgel samples.

Subsequently, Force Volume mode measurements were conducted to obtain high-resolution mechanical property maps. The measurement parameters were: 192 × 192, force threshold of 5.0 nN to ensure sufficient indentation, ramp rate of 10 Hz, and 3072 samples per force curve. The ramp size was varied from 500-1500 nm depending on the microgel height to ensure adequate indentation depth, while scan size was based on the microgel radius: small microgels (2.0 × 2.0 μm^2), large microgels (4.0 × 4.0 μm^2), and ULC microgels with diameters exceeding 600 nm (up to 6.0 × 6.0 μm^2).

For statistical robustness, measurements were performed on multiple microgels per sample type. A minimum of 8 microgels were analyzed for each microgel variant, with up to 15 microgels measured for the most comprehensive datasets. Individual measurement

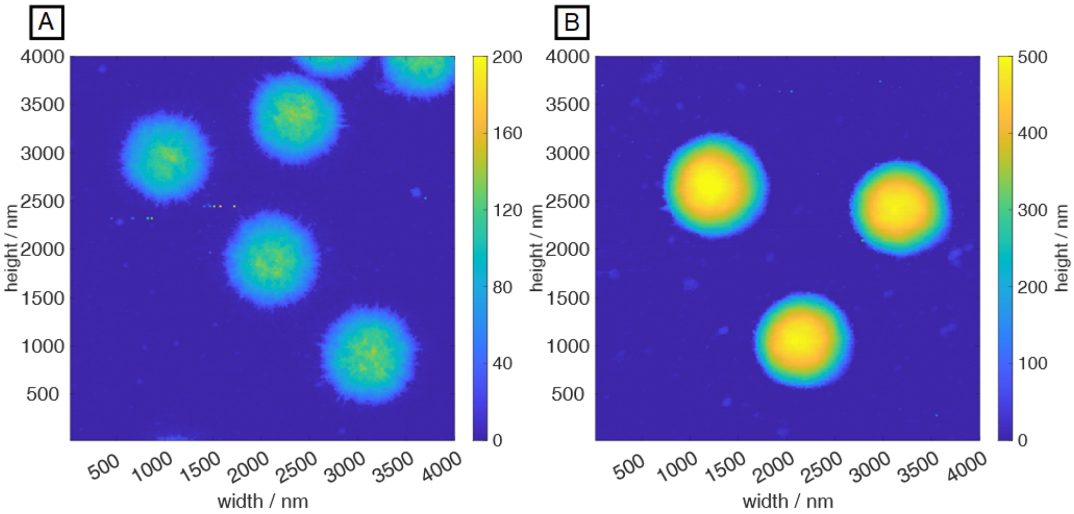

Fig. 4.4 Corrected height image from AFM of microgels L5% (A) and L12% (B) adsorbed by spin-coating on PAH coated glass subtrate in Ringer's solution at 27 °C.

sessions typically analyzed 3-5 microgels per scan area, with multiple scan areas measured per substrate to achieve the target sample sizes. The exception was ULC microgels, which, due to their tendency to spread extensively on the surface and exhibit greater morphological variability, required individual measurements for each particle. Care was taken to select microgels that were well-separated from neighbors and showed no visible defects or aggregation.

Measurement data were extracted using Nanoscope Analysis 1.9 Software (Bruker Corporation) and processed using custom-made MATLAB scripts specifically developed for microgel force-distance curve analysis and contact stiffness calculations. All force-distance curves underwent systematic baseline correction and contact point determination using established algorithms adapted for soft microgel analysis. Contact points were identified using a combination of threshold detection and curve fitting methods to account for the gradual onset of repulsive forces characteristic of soft, deformable particles. The contact stiffness parameter, defined as the local derivative of force with respect to indentation depth (dF/dδ), was calculated to provide contact stiffness microgels profiles. The detailed data processing methodology, including contact stiffness profiles formulation, followed procedures outlined in previous publications [99].

4.3.4 Comparison of spin-coating and in situ adsorption

AFM provides unique capabilities for investigating the mechanical properties of microgels at the nanoscale [93], offering several distinct advantages over conventional bulk characterization methods. Using force volume measurements, we can map the three-dimensional distribution of mechanical properties throughout individual microgel particles, revealing spatial heterogeneities that are inaccessible to ensemble-averaged techniques such as rheometry or dynamic light scattering.

The choice of the AFM probe is crucial for these measurements and determines the type of mechanical information obtained. Large colloidal probes (typically 1-20 μm in diameter) compress the microgel network over extended contact areas, providing information about bulk elasticity and Young's modulus through Hertzian contact mechanics. In contrast, sharp cantilevers can penetrate between polymer chains and network junctions, revealing local mechanical properties at high spatial resolution [136]. The penetration depth and force response depend on the local network density, cross-linking degree, and polymer chain mobility.

In our study, we employed sharp cantilevers to probe the internal structure of the microgels. As the tip penetrates the microgel, the resulting force-distance curves provide detailed information about local resistance to deformation as a function of indentation depth. The first derivative of these curves, designated as contact stiffness (dF/d$_{delta}$), enables us to generate three-dimensional mechanical property maps (Fig. 4.5). This approach is particularly valuable for microgels, which often exhibit radial gradients in cross-linking density due to their precipitation polymerization synthesis mechanism.

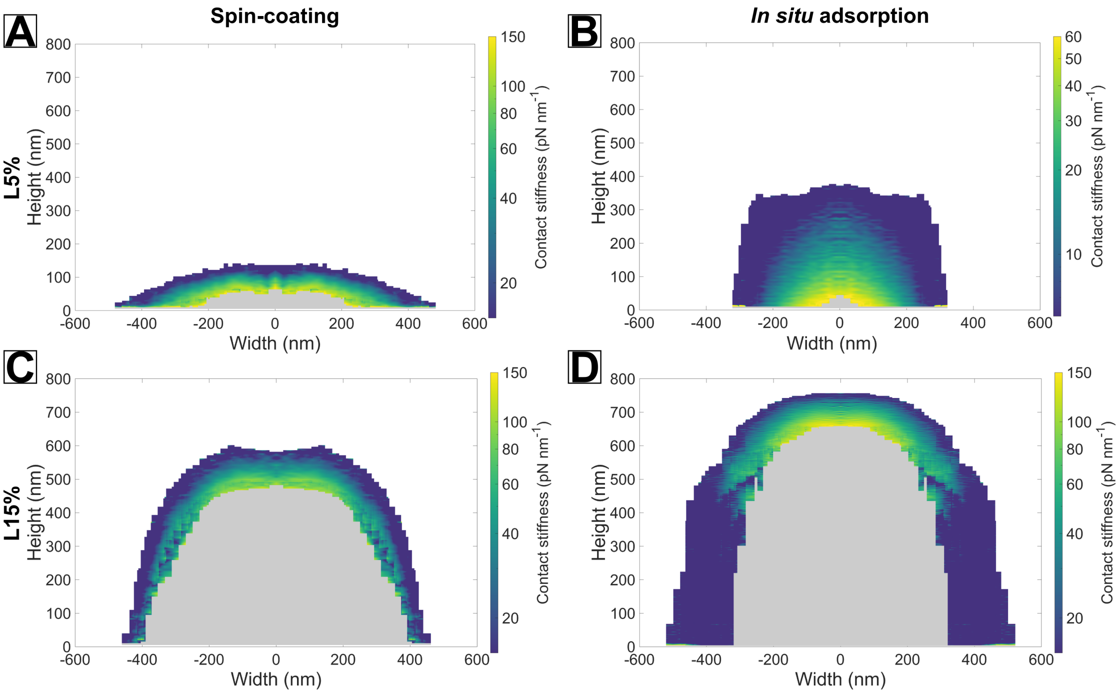

Fig. 4.5 Corresponding contact stiffness profiles through the center of the single microgel, measured in Ringer's solution at 27 °C on a PAH-functionalized glass substrate. Samples were prepared via spin-coating (A) L5%, (C) L15% and via in-situ adsorption (B) L5%, (D) L15%. The color bar is 0-150 pN/nm for (A, C, D), 0-60 pN/nm for (B).

We initially chose two types of large microgels - L5% and L15% - as they have similar hydrodynamic sizes (427 nm and 463 nm respectively, Table 4.2) but exhibit contrasting cellular uptake behavior: L5% was readily internalized by cells with a median uptake time of 1610 seconds, while L15% showed no detectable uptake within the experimental timeframe of 90 minutes.

For the initial comparison, we implemented spin-coating preparation given its several advantages, including precise control over microgel surface density through adjustment of concentration and spinning parameters, and the ability to store samples for measurement in both dry and rehydrated states. Figure 4.5A,C shows the contact stiffness profiles of these two microgel types prepared using spin-coating. Clear differences between the microgels are evident, with L5% showing substantially more flattening and reduced contact stiffness compared to L15%, consistent with their different cross-linking densities. Notably, in all measurements, the central regions remained inaccessible to the AFM tip due to the force threshold set during the experiment, with L15% showing a larger inaccessible region indicative of its higher rigidity. However, both types appeared more compressed than expected, showing reduced height and increased contact stiffness due to deformation artifacts introduced during the drying process.

We subsequently faced a critical experimental challenge that necessitated a change in our sample preparation approach. S5% microgels consistently detached upon rehydration, making reliable AFM measurements impossible.

The difference between L5% and L15% microgels using *in situ* adsorption is shown in Figure 4.5B,D. Several important observations emerge from this comparison. While overall compression was less pronounced compared to spin-coating (heights increased to 350 nm for L5% and 750 nm for L15%), the distinctive mechanical properties of each microgel type were preserved and even more clearly defined. The contact stiffness values were generally lower (maximum 60 pN/nm for L5%, 120 pN/nm for L15%), indicating that the microgels retained more of their native softness.

This challenge led us to implement *in situ* adsorption [133], an alternative approach that allows measurement of all types of microgels without detachment issues. In this method, microgels are allowed to adsorb directly from solution onto the substrate, followed by gentle rinsing to remove unbound particles. While this method is more time-consuming and technically demanding, it introduces fewer structural changes to the microgels, allowing them to maintain a configuration that better represents their native swollen state during cellular experiments.

After selecting the *in situ* adsorption method as our standard approach, we measured additional microgel types including S5%, S15%, L10%, and L12% to establish comprehensive structure-property relationships across our entire microgel library (Figure 4.6). These measurements revealed distinct mechanical signatures across the range of formulations, confirming the ability of our AFM approach to differentiate between microgels with varying cross-linking densities and sizes.

Large microgels with high cross-linker content (L10%, L12%) showed minimal deformation and high contact stiffness values , similar to L15%. The mechanical profiles were characterized by steep stiffness gradients and large inaccessible core regions, indicating limited penetration of the AFM tip into the rigid polymer network. In case of small microgels, S15% also demonstrated minimal deformation while S5% microgels exhibited high extreme softness with substantial deformation even under minimal applied force. The contact stiffness values were around 30 pN/nm across the entire particle cross-section, and the AFM tip could penetrate nearly to the substrate with minimal resistance.

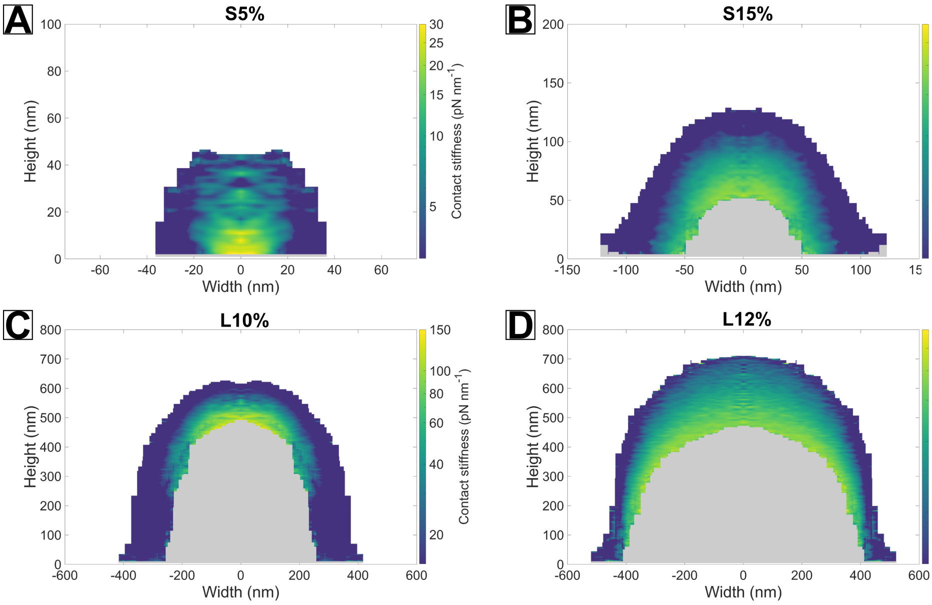

Fig. 4.6 Corresponding contact stiffness profiles through the center of the single microgel, measured in Ringer's solution at 27 °C on a PAH-functionalized glass substrate. Samples were prepared via *in situ* adsorption. (A) S5%, (B) S15%, (C) L10%, (D) L12%.

4.3.5 Analysis of microgels vertical deformation

While contact stiffness profiles provided valuable insights into the spatial distribution of mechanical properties within individual microgels, we aimed to identify additional quantitative parameters that would enable systematic comparison across all microgel types in our library. We selected two parameters for quantitative analysis: vertical deformation and force-distance curve characteristics.

Vertical deformation, defined as the ratio of the height of the surface-adsorbed microgel to its hydrodynamic diameter in bulk solution, provides information about particle softness and the strength of particle-substrate interactions. For an ideally rigid, undeformed sphere adsorbing onto a surface, this ratio would approach 1, indicating minimal shape change upon surface contact. With increasing deformation due to particle softness or stronger surface interactions, this ratio decreases toward lower values. The theoretical minimum approaches 0 for completely flattened particles.

The comparison of vertical deformation revealed distinct patterns that were strongly dependent on the sample preparation method employed. For spin-coated samples, this parameter effectively distinguished between microgels with different cross-linker content (Fig. 4.7A), showing a clear trend where higher cross-linking density resulted in reduced deformation (higher vertical deformation ratios). The spin-coated L5% microgels showed vertical deformation ratios of approximately 0.2, while L15% microgels maintained ratios near 0.7. However, S5% microgels could not be reliably measured using spin-coating due to consistent desorption during the hydration step, limiting the comprehensiveness of this analysis.

For *in situ* adsorbed microgels, the relationship between cross-linking density and deformation became more complex (Fig. 4.7B). While the general trend of softer microgels showing greater deformation was preserved, the absolute values were different. Interestingly, we observed a trend where increasing vertical deformation (i.e., greater flattening) corresponded to decreasing cellular uptake ability across our microgel library. However, this correlation was complicated by size effects that required careful interpretation. S15% microgels, despite showing intermediate internalization times between S5% and L5% (1089 seconds versus 732 and 1610 seconds, respectively), exhibited high vertical deformation similar to non-internalized large microgels. This apparent inconsistency can be attributed to size-dependent surface interaction energies, which typically cause greater deformation in smaller microgels when comparing particles of similar intrinsic stiffness [100].

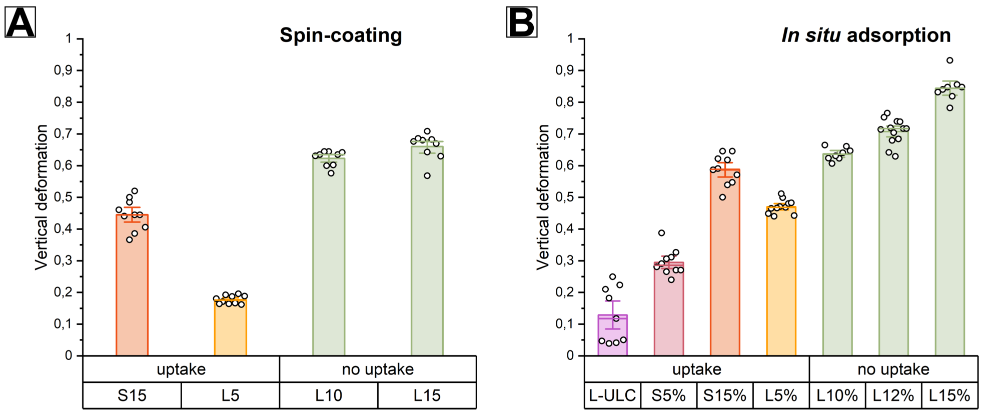

Fig. 4.7 Vertical deformation for microgels, measured in Ringer's solution at 27 °C on a PAH-functionalized glass substrate. Samples were prepared via spin-coating (A) and via *in situ* adsorption (B).

4.3.6 Analysis of force distance curves

While vertical deformation provides useful insights within size-matched groups, we recognized the need for a more comprehensive parameter that could enable meaningful comparisons between microgels of different sizes and overcome the limitations imposed by size-dependent surface interactions. This requirement led us to analyze force-distance curves, which measure the resistance encountered by the AFM tip as it penetrates the polymer network and proved to be particularly informative for characterizing microgel mechanical properties.

Figure 4.8A shows the averaged force-distance curves measured at the apex (center) of each microgel type after *in situ* adsorption. For each microgel type, approximately ten individual microgels were measured, and their force-distance curves were averaged to obtain the representative curves. In these measurements, the zero point represents initial tip-microgel contact, with positive values indicating tip penetration depth. The differences between high and low cross-linked microgels were clear. Under the standardized applied force of 5 nN, the AFM tip penetrated approximately 300 nm into L5% microgels but only 80 nm into L15% microgels.

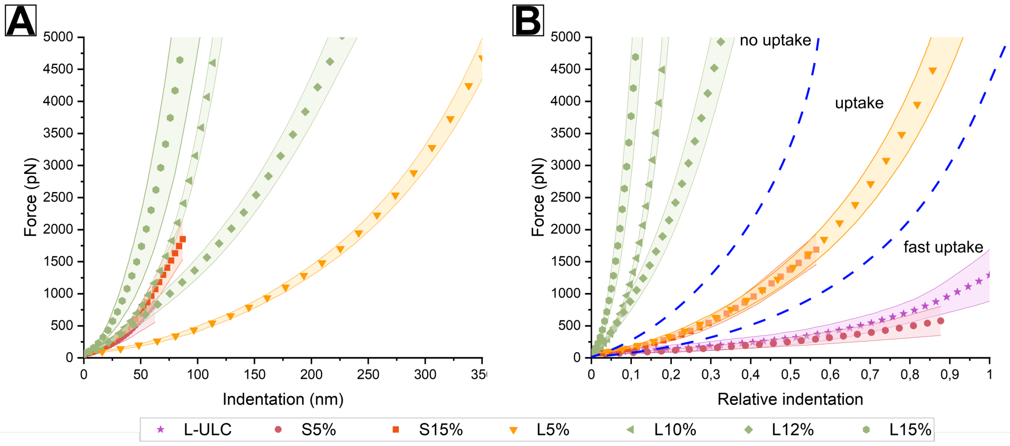

Fig. 4.8 Averaged force-distance curves corrected by the contact-point for the vertical approach of an AFM tip towards microgel's center. Microgels were measured in Ringer's solution at 27 °C on a PAH-functionalized glass substrate after *in situ* adsorption. Data are presented as (A) absolute indentation depth and (B) relative indentation normalized to the height of the adsorbed microgel.

However, direct comparison of absolute penetration depths was complicated by variations in microgel size, as larger particles naturally provide more material volume for tip penetration. We addressed this limitation by normalizing the data, plotting force versus the ratio of indentation depth to the height of the adsorbed microgel – termed "relative indentation" (Fig. 4.8B). This normalization approach effectively removes size-dependent effects and enables direct comparison of intrinsic mechanical properties across the entire microgel library. The normalization revealed a remarkable correlation between mechanical properties and cellular uptake phenotype that was not apparent in the raw force-distance data. The microgels clustered into three distinct groups based on their relative indentation values, with clear boundaries separating different uptake behaviors:

- A "fast uptake" group (rightmost in the plot), comprising S5% microgels with the highest relative indentation and fastest cellular internalization
- An "intermediate uptake" group, including L5% and S15% microgels, showing moderate relative indentation and slower but successful cell entry
- A "no uptake" group (leftmost), containing large microgels with >10% cross-linking, characterized by low relative indentation and no cellular internalization

This correlation between relative indentation and cellular uptake suggests that this normalized mechanical parameter could serve as a predictive indicator for microgel-cell interactions.

4.3.7 Introducing L-ULC microgels

Having established a strong correlation between AFM-measured mechanical properties and cellular uptake behavior across our conventional microgel library, we sought to rigorously test this relationship using a fundamentally different class of microgels that would challenge the boundaries of our predictive framework. We synthesized large ultra-low cross-linked (ULC) microgels using acrylic acid as the ionic comonomer. These microgels represent an extreme case in the softness spectrum, as they are formed through self-cross-linking reactions during precipitation polymerization rather than through the addition of dedicated cross-linking agents like N,N'-methylenebisacrylamide [44–46].

Characterization of these ULC microgels using static light scattering (SLS) revealed their size distribution and internal structure through fuzzy sphere modeling (Fig. 4.9A,B). Remarkably, despite having a radius of 900 nm - far above the size typically associated with efficient cellular uptake - these ULC microgels demonstrated not only successful internalization but the fastest uptake kinetics observed across our entire study, with a median internalization time of 430 seconds (Fig. 4.10A). This uptake rate was even faster than the previously fastest S5% microgels (732 seconds), despite the ULC microgels being nearly an order of magnitude larger in volume.

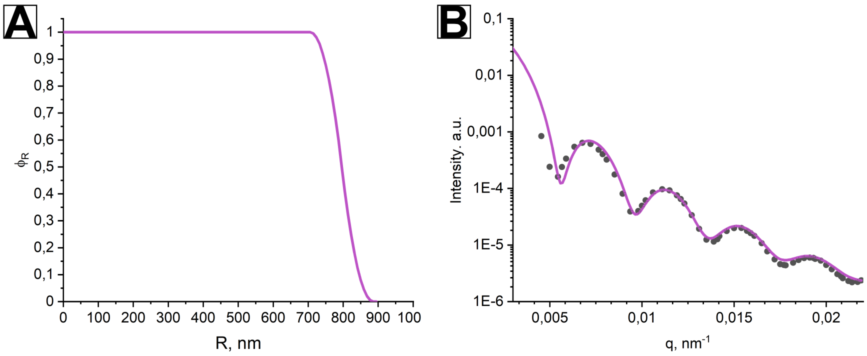

Fig. 4.9 Static light scattering characterization of L-ULC microgels. (A) SLS form factor fitted with fuzzy sphere model at 20 °C in Ringer's solution. (B) Relative radial density profile obtained from fitting.

The rapid internalization kinetics were confirmed through comprehensive confocal microscopy analysis. Fig. 4.10B shows a representative HEK293T cell after 1 hour of incubation with L-ULC microgels (red fluorescence), where additional membrane staining (cyan) was used to clearly delineate the cell boundaries and confirm internalization rather than adhesion on the cell membrane. To provide additional confirmation of internalization and eliminate any ambiguity about particle localization, orthogonal projections from z-stack confocal images were acquired after incubation with L-ULC microgels (Fig. 4.10C,D). In these experiments, the extracellular solution was labeled with a membrane-impermeable dye (green) to provide additional contrast and clearly distinguish between intracellular and extracellular spaces. The orthogonal views (XZ and YZ projections) demonstrate that the large L-ULC microgels were internalized into the cell interior and did not remain adsorbed on the external cell membrane surface.

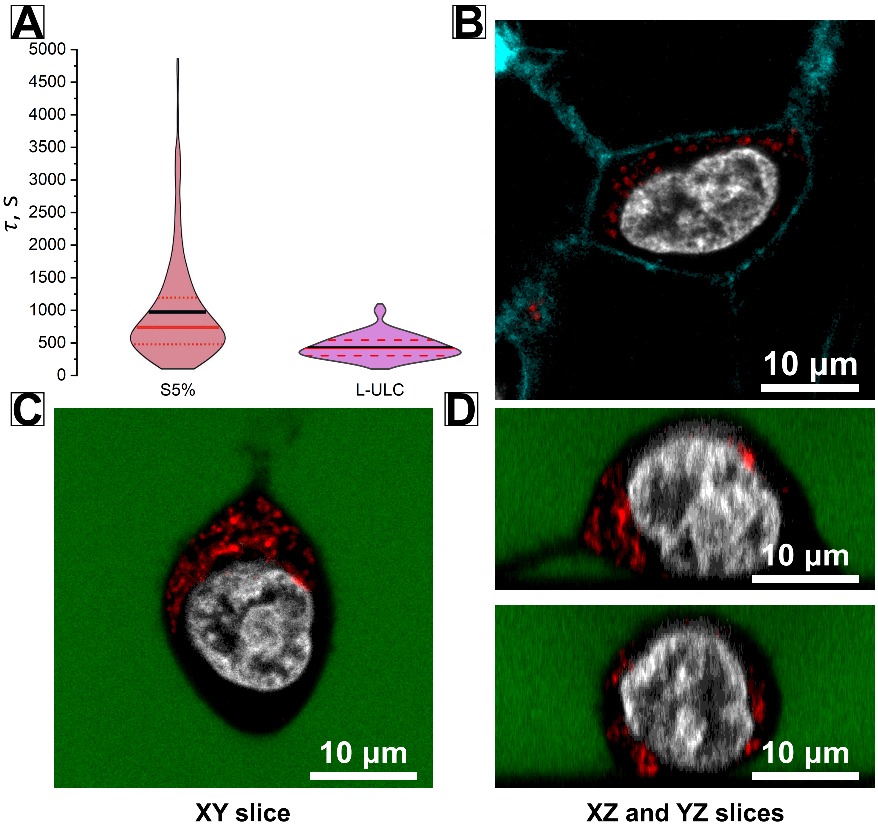

Fig. 4.10 (A) Comparison of the uptake kinetics for S5% and L-ULC microgels. Violin plots internalization time distributions: average (black line) and median (red line), dashed red lines show upper and lower quartiles. Data for S5% adapted with permission from [132]. (B) Typical image of a cell after 1 hour of incubation with L-ULC (red) with additional staining: membrane (cyan) and nucleus (grey). (C,D) - orthogonal projection from Z-stack of a cell after 1 hour of incubation with L-ULC (red) with additional extracellular solution (green) and nucleus (grey) stainings. The scale bar is 10 μm.

To connect these unprecedented cellular behaviors with mechanical properties, we performed comprehensive AFM characterization of ULC microgels (L-ULC). Based on previous work [99], measuring such ultra-soft particles in their fully swollen state presented significant technical challenges, as their extreme deformability typically renders them nearly 'invisible' to conventional AFM imaging modes. However, the combination of their large size (900 nm radius) and negative surface charge enabled successful imaging and mechanical characterization.

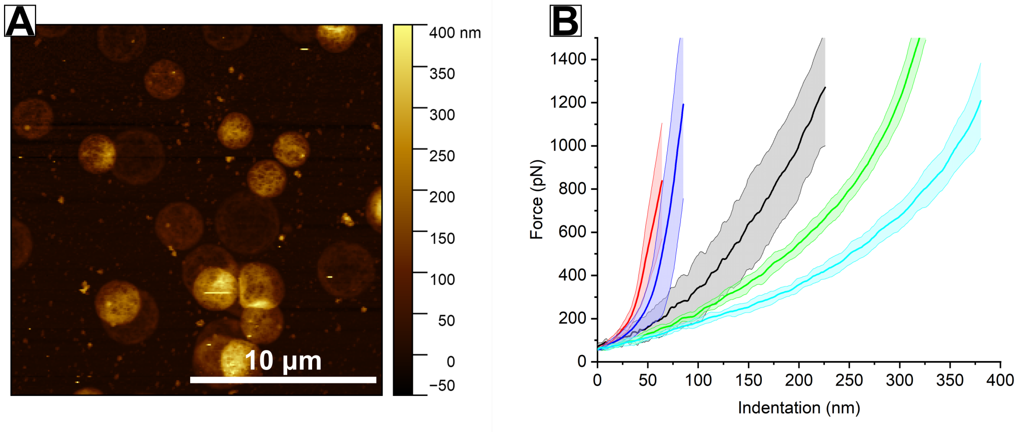

Fig. 4.11 AFM measurement of L-ULC microgels in Ringer's solution at 27 °C on a PAH-functionalized glass substrate after *in situ* adsorption. (A) Height image in scanning mode. (B) Force-distance curves of individual L-ULC microgels corrected by the contact-point for the vertical approach of an AFM tip towards microgel's center.

Initial AFM measurements revealed remarkable heterogeneous surface behavior of L-ULC microgels (Fig. 4.11A), reflecting the exceptional softness of their polymer structure. This heterogeneity represents a fundamental difference from the more uniformly cross-linked conventional microgels studied previously. During adsorption at the glass/water interface, heterogeneous stretching and reorganization of the loosely cross-linked polymeric network occurs, leading to enhanced size polydispersity and morphological diversity [140]. Individual ULC microgels displayed significant variations in their surface-adsorbed conformations, ranging from near-spherical to extensively flattened morphologies. Some particles exhibited extreme flattening, reaching contact radii of up to 2 μm with heights as low as 50 nm, while others maintained more hemispherical shapes with heights approaching 200-300 nm.

This morphological diversity significantly affected the force-distance measurements, resulting in substantial variations between individual microgels (Fig. 4.11B). Despite this variability in absolute measurements, which initially appeared to challenge the utility of AFM characterization for ULC systems, our relative indentation analysis proved remarkably effective in normalizing these size and morphology variations. When the indentation depths were normalized by the local particle height at each measurement location, the resulting relative indentation values showed much more consistent behavior across different ULC microgel conformations. Most remarkably, when plotted on our established mechanical-uptake correlation framework, ULC microgels positioned themselves firmly in the "fast uptake" region of Figure 4.8B, with relative indentation values exceeding 0.9 in many cases. This placement perfectly aligned with their rapid cellular internalization behavior and provided compelling validation of our predictive framework across a much broader range of microgel properties than initially anticipated. This striking correlation between AFM-derived mechanical parameters and cellular uptake kinetics provides compelling support for our analytical framework and suggests its potential predictive value for designing new microgel systems with tailored cellular interaction properties.

4.4 Discussion

Internalization of various compounds is an essential mechanism in cellular life. Depending on their size, shape, softness and surface treatment, nanocarriers can enter cells through different pathways [113, 141]. At the nanoscale (<200 nm), clathrin-dependent and caveolae-dependent pathways typically dominate, while larger objects primarily enter through macropinocytosis or phagocytosis. However, the relationship between size and uptake becomes more complex when considering highly deformable microgels. For example, Banquy et al. showed that the uptake of soft small microgels is significantly reduced after amiloride treatment, which inhibits macropinocytosis. While various pathway-specific inhibitors are commonly used to determine uptake mechanisms, this approach has limitations. Most inhibitors significantly modify cell physiology, potentially causing side effects (e.g., cytotoxicity) and triggering compensatory uptake mechanisms. Genetic approaches, such as knockouts of specific proteins, can provide more definitive pathway identification. However, these advanced biological methods require extensive cell line modification and molecular biology techniques, which extend beyond the scope of our study. Instead, we focused on establishing the fundamental relationship between microgel mechanical properties and cellular uptake, providing a physical framework for future, more detailed biological investigations.

The systematic correlation between AFM-derived mechanical parameters and cellular uptake kinetics reveals fundamental principles governing microgel-cell interactions. Our approach successfully identified three distinct groups of microgels with characteristic uptake phenotypes. The first "fast uptake" group includes both the relatively small and soft S5% microgels and the extremely soft and large L-ULC microgels. Despite their significant size difference, both types demonstrate rapid internalization. AFM measurements reveal that both S5% and L-ULC microgels are exceptionally soft, with the cantilever encountering minimal resistance (not exceeding 2 nN, Figure S1). This suggests that softness, rather than size, plays the dominant role in cellular uptake of these microgels, marking a significant difference from interactions with rigid nanoparticles. Previous studies with small nanoparticles (<200 nm) have shown that increased stiffness typically enhances cellular uptake [122–124], One possible explanation is that soft particles tend to flatten against the cellular membrane, potentially increasing the energy barrier for complete membrane wrapping [125]. However, this mechanical limitation appears less critical for macropinocytosis, where rearrangement of the cytoskeleton forms large vesicles (0.2-5 μm macropinosomes) capable of internalizing substantial volumes.

The second "intermediate uptake" group comprises both stiff small (S15%) and soft large (L5%) microgels. For S15% microgels, successful internalization is not unexpected, as stiffness is not a major limitation for nanoscale objects. However, their increased cross-linking density reduces deformability, resulting in slower uptake compared to S5%. More notably, L5% microgels achieve cellular entry despite exceeding the typical size threshold (>500 nm) for non-phagocytic uptake. This suggests that in this intermediate regime, both size and stiffness modulate uptake kinetics, with increases in either parameter reducing internalization rates.

The third "no uptake" group consists of large microgels with high cross-linking density. Unlike L5%, these microgels exhibit minimal vertical deformation during surface adsorption, indicating limited deformability. This observation suggests that for micron-sized particles, deformability becomes a critical parameter that determines whether cellular internalization is possible at all.

The critical insights into the relationship between microgel softness and cellular uptake were made possible through our specific AFM approach using Force Spectroscopy with a sharp tip. In contrast to large colloidal probes, that are usually used for Young's modulus measurement, small sharp tip reveals local mechanical properties at nanoscale resolution. This method is particularly valuable for ultra-soft microgels like L-ULC, whose adsorption at interfaces is highly sensitive to changes in environmental conditions, resulting in diverse interfacial shapes and patterns [142]. The ability to resolve nanoscale mechanics ensures robust characterization of these responsive systems. Our experiments not only demonstrated a clear correlation between AFM-defined softness and cellular uptake but also revealed the remarkable ability of large ULC microgels (1.8 μm in diameter) to be internalized by cells. To our knowledge, this is the first demonstration of non-phagocytic uptake of nanocarries of this size [114, 117, 143]. As HEK293T are not-phagocytic, only macropinocytosis is possible.

The involvement of specific uptake pathways is particularly interesting for drug delivery applications [129]. Many cancer cell types, including lung, pancreatic, and breast cancer cells, upregulate macropinocytosis to increase nutrient uptake from the tumor microenvironment [144]. Exploiting this pathway could enhance delivery specificity, potentially leading to more efficient treatment with fewer side effects. Additionally, recent studies also have shown that soft nanoparticles have prolonged blood circulation time, ability to penetrate deeper into the tumor and to avoid uptake by macrophages [145–147]. These findings significantly expand the potential biomedical applications of ULC microgels, particularly in targeted drug delivery systems.

4.5 Conclusions

The Force Spectroscopy measurements proved especially powerful, providing quantitative parameters that successfully predicted uptake behavior across our entire range of microgels, from highly deformable to relatively rigid microgels. In case of particularly soft polymer networks, size ceases to play a fundamental role, allowing the uptake of both small and large microgels. Moreover, micron-sized ULC microgels showed the remarkable ability for cellular uptake. In case of increased stiffness, the combination of size and softness begins to play a role, where increasing of either parameter reducing internalization rates. Thus, by manipulating the microgels size and stiffness, the specific features of microgel-cell interactions can be reached. These results will be a useful tool for the future design of therapeutic agents.

Chapter 5

Post-Endocytotic Effects of Microgel Internalization

5.1 Introduction

Microgels are cross-linked polymer networks swollen with water that represent a promising frontier in biomedical applications. Due to their unique features and responsive behavior, many microgel-based systems have been developed for biomedical applications, including drug delivery, biosensing, and tissue engineering. However, the effects of microgel internalization on cell homeostasis and long-term impacts on cellular processes remain poorly understood.

Endocytosis is the process by which cells internalize extracellular materials. Internalization of nanoparticles depends on many features including cell type, particle size, charge, surface chemistry, and stiffness of the nanoagent. In the case of microgels, current results show that softness could define the uptake pathway: macropinocytosis for soft microgels and clathrin-mediated endocytosis for stiffer ones. In our previous research, we studied the size effect on microgel uptake, and in Chapter 4, we demonstrated using atomic force microscopy (AFM) that the combination of softness and size could predict the ability of microgels to be taken up by cells. Remarkably, both small microgels and even 1 μm diameter microgels with 5% of cross-linking were successfully internalized by HEK293T cells. Additionally particularly intriguing were ultra-low cross-linked (ULC) microgels, which despite having diameters exceeding 1.8 μm, demonstrated the fastest cellular uptake kinetics.

At the same time, there is lack of information what happens after microgel uptake. While poly(N-isopropylacrylamide) (PNIPAM)-based microgels show low cytotoxicity [132, 148], these standard methods miss subtle cellular homeostasis changes.

One important part of the cell is the cytoskeleton, which consists of actin filaments, microtubules, and intermediate filaments. These components play critical roles in maintaining cell shape, enabling cell movement, facilitating intracellular transport, and supporting cell division [149]. Internalization of nanoagents can trigger cytoskeletal disruption. While this effect could be exploited as a therapeutic strategy in cancer treatment, it must be strictly avoided when treating healthy cells. It has been shown that some types of rigid nanoparticles could directly interact with cytoskeletal structures. In one study, CuO nanoparticles interacted with actin filaments, causing cytotoxic effects in Arabidopsis root cells [150]. In another study, heating stimulated by near-infrared irradiation of gold nanorods already bound to actin filaments inside HeLa cells led to the loosening of cell junctions between cells [151].

Another important question is endosomal and lysosomal activity following microgel uptake. Understanding where microgels go within the cell could give important hints for the design and functionality of microgel-based therapeutic agents. While for microgels the endosome-lysosome pathway was observed [148], specific formulation modifications can direct particles to non-degradative routes. For example, 50 nm hyperbranched polymers micelles showed ability to endosomal escape [152]. The fate of internalized microgels—whether they remain in early endosomes, progress to late endosomes, or ultimately reach lysosomes has significant implications for drug delivery applications, as the increasingly acidic and enzymatic environment along this pathway can trigger cargo release or affect microgel stability.

In this chapter, we studied how PNIPAM microgels with methacrylic acid (MAA) as a comonomer affect HEK293T cells. Our findings showed that 4 hours of incubation does not affect the actin network, while the microtubule network undergoes some changes, including an increase in filaments straightness and branching level complexity. In terms of endosomal maturation, microgels showed gradual accumulation with more then 80% in lysosomes after 4 hours of incubation. Despite the valuable insights from this study, further experiments should be conducted in the future to fully understand the long-term effects of microgel internalization on cellular homeostasis and to optimize microgel design for specific therapeutic applications.

5.2 Materials and Methods

Microgel Synthesis

In this study small PNIPAM microgels with MAA with 5% of BIS were used. The synthesis is described in Section 4.2.

Cell culture

In this study also HEK293T cells were used, cultivated similar to Section 4.2.

Confocal Live-Cell Imaging of Cytoskeleton structure and Lysosomes Distribution

Measurements were carried out using an inverted confocal laser scanning microscope (Leica TCS SP8) with additional STED module (Leica TCS STED X) and HC PL APO 86x/1.20 water objective. For investigation of microgel post-endocytotic effects, microgel solution (0.5 mg/mL) was added to cells in Ringer solution and incubated for the desired time at 37 °C. Following incubation, cells were prepared for imaging. Single typical cells were identified and imaged using z-stack sequences with white light laser excitation at 561 nm (microgels labeled with rhodamine B), 650 nm (SPY650-Tub or SPY650-FastAct), and 488 nm (Lysoview). All measurements were performed at 22 °C. The acquired image data was subsequently analyzed using Imaris software.

5.2.1 Description of Experimental System

Microgels and Cell Line

Based on our previous studies of microgel-cell interactions [132], we selected PNIPAM microgels with 5 mol% cross-linking density and MAA as comonomer for this investigation (S5% from Table 4.2). These small, soft microgels demonstrated the fastest cellular uptake kinetics, with median internalization times of approximately 732 seconds in HEK293T cells. The incorporation of MAA enhances colloidal stability in physiological conditions.

We continued to use HEK293T cells as our model system, as they represent a well-characterized human embryonic kidney cell line with established properties for various studies. HEK293T cells combine the practical advantages of an immortalized cell line with behavior more representative of normal human cells compared to cancer-derived lines, making them an ideal platform for investigating fundamental microgel-cell interactions.

Advanced Fluorescent Probe Selection for Live-Cell Analysis

Cytoskeletal Dynamics Monitoring. For investigating the impact of microgel uptake on cellular cytoskeletal organization, we employed novel fluorescent probes from the Spirochrome, which offer superior photostability and brightness for live-cell imaging applications. Specifically, we selected:

- **SPY650-Tub:** A far-red fluorescent probe that specifically binds to microtubules with high affinity and minimal cellular toxicity. This probe enables real-time visualization of the microtubule network dynamics during the measurement [153].
- **SPY650-FastAct:** A far-red probe designed for specific labeling of F-actin filaments in living cells [154]. This probe allows for the assessment of actin cytoskeleton reorganization that may occur during microgel internalization.

Membrane Tension Analysis To investigate potential changes in plasma membrane tension during microgel uptake, we implemented the innovative Flipper-TR probe[155]. Flipper probes represent a novel class of mechanosensitive fluorescent membrane probes that respond to changes in membrane tension through alterations in their fluorescence lifetime. Flipper-TR spontaneously inserts into the plasma membrane of cells and is only fluorescent when inserted in a lipid membrane. It senses changes of the organization of lipid bilayer membranes through changes of the twist angle and polarization between the two twisted dithienothiophenes of the mechanophore (Fig. 5.1).

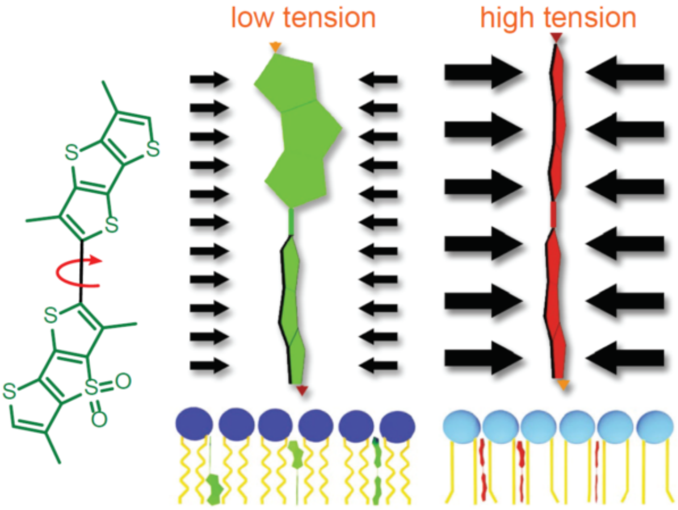

Fig. 5.1 Schematic representation of the Flipper-TR working principle. Under low membrane tension, the probe adopts a twisted conformation with the fluorescent groups oriented at an angle, resulting in shorter fluorescence lifetime (green conformation, left). When subjected to mechanical forces (black arrows) due to increased membrane tension, the molecular backbone planarizes, bringing the fluorescent groups into alignment (red conformation, right).

Lysosomal Trafficking Assessment For tracking the intracellular fate of internalized microgels, we utilized LysoView488 (Biotium): dye with weakly basic amine groups that specifically accumulates in acidic organelles including lysosomes and late endosomes. These pH-sensitive probe (typically pH 4.5-5.5) enables visualization of microgel trafficking through the endolysosomal pathway.

5.3 Results

5.3.1 Impact of Microgels on Actin Cytoskeleton Organization

Our investigation of actin cytoskeleton dynamics revealed minimal structural changes that we can observed following microgel exposure (Fig. 5.2). Time-lapse imaging using SPY650-FastAct showed that the characteristic actin network organization remained largely unchanged during the first hour of internalization. Quantitative analysis of actin filaments density, orientation, and branching patterns was complicated by the lack of sufficient separation of the fibers from each other. There was also no significant rearrangement of actin close to the cell membrane, despite the fact that actin is actively involved in some major endocytosis pathways [143, 156].

Actin staining primarily visualizes polymerized actin filaments near the cell membrane, which are involved in substrate attachment and cell-cell junction formation (Fig. 5.2A, basal plane). While these cortical actin networks exhibit complex, heterogeneous organization that makes quantitative analysis challenging, qualitative assessment revealed no apparent structural changes following microgel uptake. Notably, microgels were not observed to localize within these cortical actin-rich regions, suggesting minimal direct interaction between microgels and the peripheral cytoskeleton.

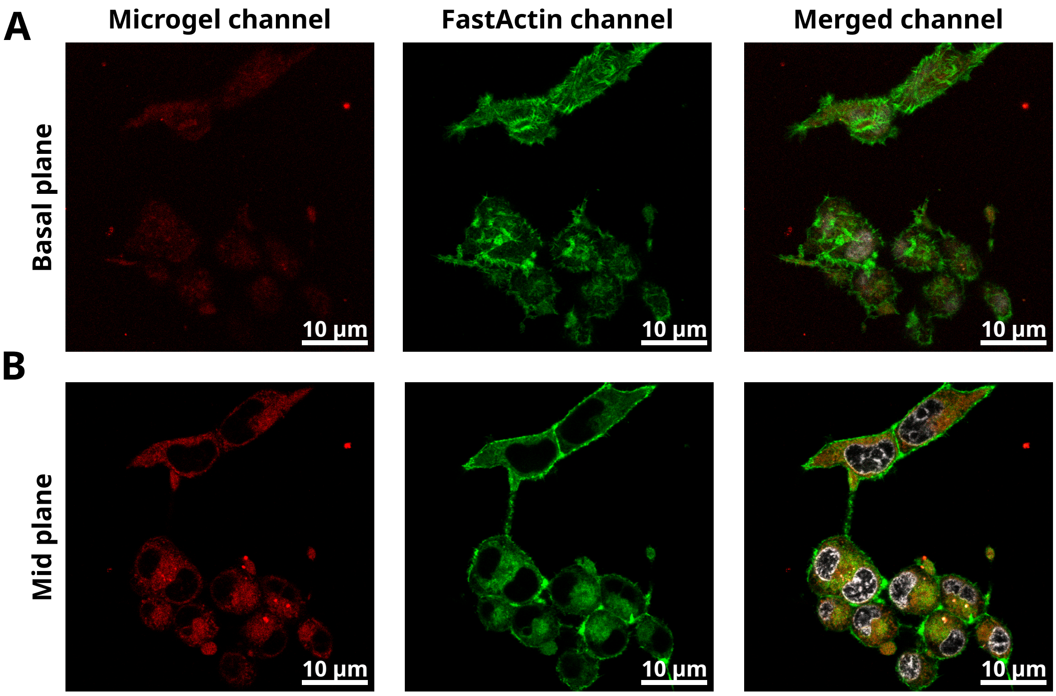

Fig. 5.2 Spatial distribution of actin cytoskeleton and microgels in live HEK293T cells at different Z-planes. Confocal microscopy images showing rhodamine-labeled microgels (red, left column), FastAct-stained actin cytoskeleton (green, middle column), and merged channels (right column) at two representative Z-positions. (A) Basal plane images show cortical actin networks involved in cell adhesion, while microgels appear excluded from these dense actin-rich regions. (B) Mid plane images show intense actin and microgels presence. Merged images that also contain nuclei staining with Hoechst33342 (white), reveal that internalized microgels localize predominantly within cytoplasmic regions containing actin signal. Scale bars: 10 μm.

In the mid-plane Z-section through the cell volume (Fig. 5.2B), two distinct actin populations are visible: intense fluorescence at cell borders corresponding to the cortical actin structures observed in the basal plane, and blurry signal distributed throughout the cytoplasm. This diffuse cytoplasmic signal likely represents a combination of short actin filaments and dynamic filament assembly/disassembly intermediates - a unique feature captured by FastAct dye compared to conventional phalloidin-based actin stains that exclusively bind stable F-actin. Notably, microgels are localized in these cytoplasmic regions containing dynamic actin, which is consistent with the established roles of actin cytoskeleton in endocytosis and endosomal sorting. The preserved organization of the actin network despite substantial microgel presence suggests that microgel uptake does not significantly disrupt cytoskeletal dynamics.

These findings suggest several possible interpretations. First, HEK293T cells may not be the optimal model system for detecting actin-mediated effects of microgel uptake, as they possess less prominent actin structures compared to fibroblasts or other highly motile cells. Alternatively, the preserved actin cytoskeleton integrity could additionally indicate low cytotoxicity of the microgels. This maintenance of normal actin organization despite high uptake levels suggests that the microgels do not significantly disrupt cytoskeletal dynamics or cell mechanical properties

5.3.2 Impact of Microgels on Microtubule Network Organization

In contrast to the actin results, analysis of microtubule organization revealed some measurable changes in response to microgel internalization. In this iteration, we chose to measure the effect after some specific time and not just after adding of microgels to have more resultive effect. Additionally tubulin network remains more distinct and stable shape that could be measured easily.

To investigate potential effects on the microtubule cytoskeleton, cells were incubated with or without microgels for 1.5 and 4 hours, then stained with a tubulin dye and imaged using STimulated Emission Depletion (STED) fluorescence microscopy. This approach allowed simultaneous visualization of the tubulin network structure and microgel localization within cells. Despite achieving superior resolution through STED microscopy, the use of live cells imposed certain experimental constraints. Dynamic cellular processes resulted in continuous movement of cellular compartments during image acquisition (5-10 min per image), requiring careful optimization of acquisition parameters. Additionally, the intensity of the STED depletion laser was necessarily limited to minimize potential phototoxic effects on cell viability. While this approach provided excellent resolution of microtubule structures, the theoretical resolution limit of the technique was not fully realized under these live-cell imaging conditions.

Tubulin network analysis was performed using Imaris software following the workflow illustrated in Fig. 5.3. First, 3D reconstructions were generated from Z-stack images (Fig. 5.3A). The tubulin network was then computationally traced and skeletonized within each reconstructed volume (Fig.5.3B). Finally, quantitative parameters describing network architecture were extracted from these skeletonized structures using the Filament Tracer tool. Analysis was performed on individual cells ($n>6$ per condition), and the resulting parameters were averaged and plotted in Fig. 5.4. The analyzed parameters included:

- **Filament straightness**: the ratio between filament length and the Euclidean distance between filament endpoints, where values closer to 1 indicate straighter filaments.
- **Branch level**: a measure of network branching complexity, with higher values indicating more extensively branched networks.

- **Average length and diameter**: mean values calculated across all filaments within the microtubule network.

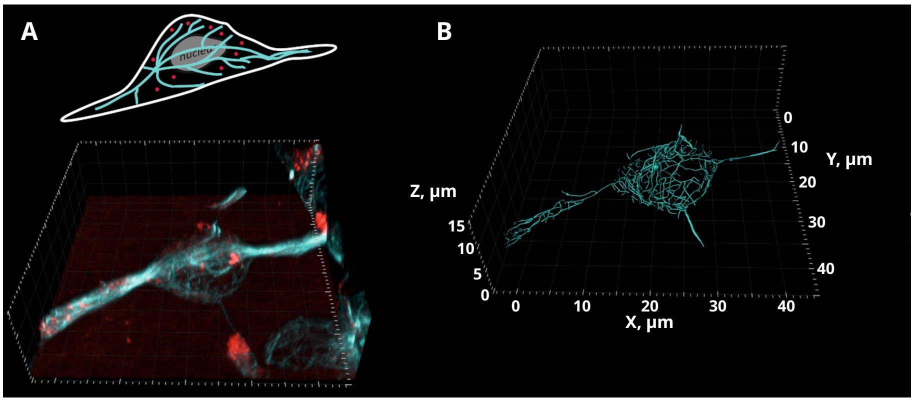

Fig. 5.3 Workflow for microtubule network analysis in HEK293T. (A) Representative 3D reconstruction of a Z-stack STED image showing microtubules (cyan) and internalized rhodamine-labeled microgels (red) within a single cell. (B) Skeletonized microtubule network extracted from the 3D reconstruction using Imaris Filament Tracer, enabling quantitative analysis of network architecture parameters.

The quantitative analysis revealed several trends in microtubule network architecture following microgel uptake, though interpretation is complicated by the inherent heterogeneity within cell populations across all conditions. For branch level (Fig. 5.4A), cells incubated with microgels exhibited an extended distribution toward higher values, suggesting a tendency toward increased network branching. Similarly, filament straightness showed condition-dependent changes (Fig. 5.4B): while control cells displayed considerable variation in straightness values, cells at 4 hours post-uptake showed a narrower distribution shifted toward slightly higher values. The distribution patterns for cells at 1.5 hours resembled those of control cells. Taken together, these observations suggest that microgel uptake may promote both increased network branching and filament straightness.

Average filament diameter also appeared to increase following microgel exposure, though this finding should be interpreted cautiously. Microtubules maintain a relatively constant diameter of approximately 25 nm determined by their structural organization of tubulin dimers. Therefore, the observed variations in measured diameter likely reflect optical limitations of the microscopy technique or sample movement during acquisition rather than true biological changes. Finally, average filament length showed no systematic changes across conditions despite variations in the distribution patterns, indicating that this parameter remains stable regardless of microgel presence.

5.3.3 Lysosomal Colocalization and Intracellular Trafficking

To investigate the intracellular trafficking and lysosomal localization of internalized microgels, colocalization analysis was performed using LysoView488, a pH-sensitive dye

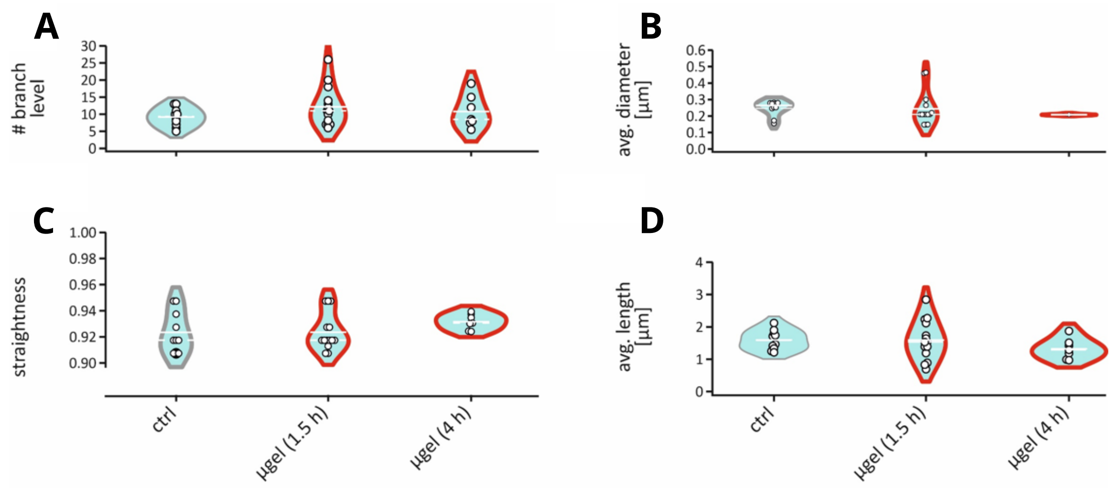

Fig. 5.4 Quantitative analysis of microtubule network parameters in control cells and cells incubated with microgels for 1.5 or 4 hours. Violin plots show the distribution of (A) branch level, indicating network branching complexity; (B) average filament diameter; (C) filament straightness, calculated as the ratio of filament length to end-to-end distance; and (D) average filament length. Each data point represents a single cell (n>6 per condition). Gray violins indicate control cells without microgels (ctrl), while red violins represent cells after incubation with microgel. Horizontal lines within violins indicate mean values (dashed) and median (solid).

that accumulates in acidic compartments and exhibits enhanced fluorescence intensity in lysosomes and late endosomes. Cells were incubated with microgels for 1 or 4 hours, then stained with LysoView488 and imaged. As a reference control, cells were also incubated with fluorescent dextran (10 kDa), a good marker for clathrin-mediated endocytosis and partially macropinocytosis [157].

Following Z-stack acquisition, images were processed using deconvolution algorithms to improve signal-to-noise ratio and spatial resolution. As demonstrated in our previous work, microgels exhibit a punctate distribution pattern within cells, consistent with confinement to individual endosomal compartments. Similarly, LysoView488 localizes to discrete puncta corresponding to lysosomes and acidified late endosomes. Three-dimensional reconstructions were generated from the deconvolved images, and individual fluorescent puncta were identified and segmented as "beads" in both the LysoView488 (blue) and rhodamine (microgel, red) channels using Imaris software (Fig. 5.5).

Colocalization analysis was performed by calculating the percentage of microgel-containing puncta that overlapped with LysoView488-positive compartments. Specifically, the ratio of colocalized microgel beads to the total number of microgel beads was determined for each cell (n>6 per condition) and plotted in Fig. 5.6. The same analytical approach was applied to cells incubated with dextran 10 kDa to enable direct comparison of trafficking kinetics between the two particle types.

The results demonstrated time-dependent differences in lysosomal localization between microgels and dextran. After 1 hour of incubation, microgels showed relatively low lysoso-

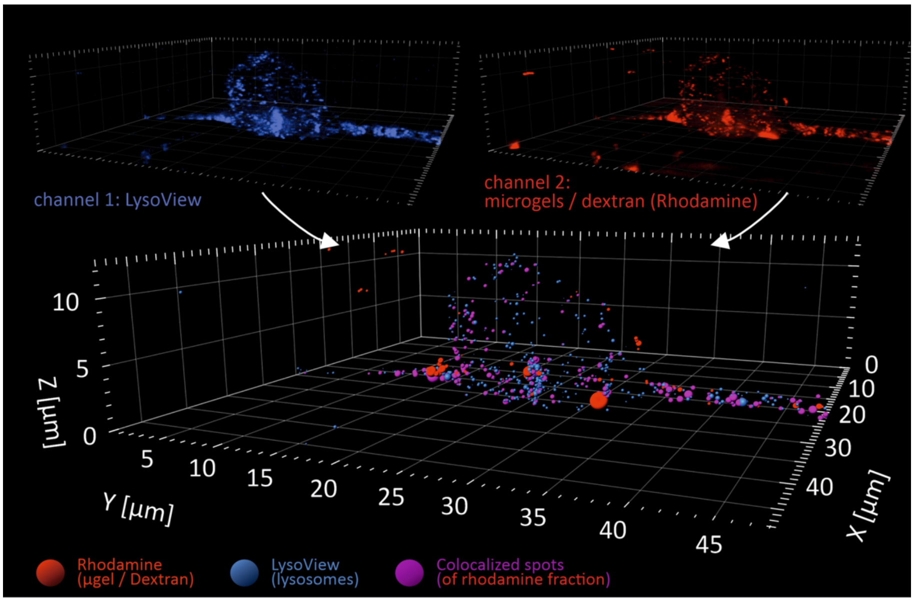

Fig. 5.5 Representative 3D colocalization analysis of microgel and lysosomal compartments in single cell. Top panels show individual channel reconstructions: LysoView488-positive lysosomes (blue, left) and rhodamine-labeled microgels or dextran (red, right). Bottom panel displays the merged 3D reconstruction: microgels/dextran (red), lysosomes (blue), and colocalized puncta (magenta). Spatial dimensions are shown in micrometers along the X, Y, and Z axes.

mal colocalization with a mean value of approximately 35%. This percentage increased dramatically to approximately 75% after 4 hours, indicating progressive trafficking and accumulation of microgels in lysosomes (Fig. 5.6). Despite considerable cell-to-cell variability within each condition, the difference between the two time points was statistically significant, demonstrating a clear temporal trend in microgel trafficking.

In contrast, dextran 10 kDa exhibited different kinetics. After 1 hour of incubation, cells showed high variability in colocalization, ranging from 30% to nearly 80%. However, after 4 hours, the colocalization decreased to approximately 20%, with a narrower distribution. This temporal decrease in lysosomal colocalization can be explained by several mechanisms. First, continued dextran uptake over 4 hours may lead to saturation of lysosomal processing capacity, resulting in accumulation of newly internalized material in earlier endosomal compartments rather than lysosomes. Second, and more importantly, dextran is readily degraded by lysosomal hydrolases, which would reduce the detectable fluorescent signal in lysosomes over time and lower the apparent colocalization ratio. In contrast, PNIPAM microgels cross-linked with BIS are resistant to enzymatic degradation, allowing them to accumulate progressively in lysosomes without being broken down.

These findings provide evidence that internalized microgels are trafficked through the endolysosomal pathway, consistent with endocytotic uptake mechanisms. The temporal progression from partial to extensive lysosomal localization reflects the normal kinetics of endosomal maturation and lysosomal fusion processes.

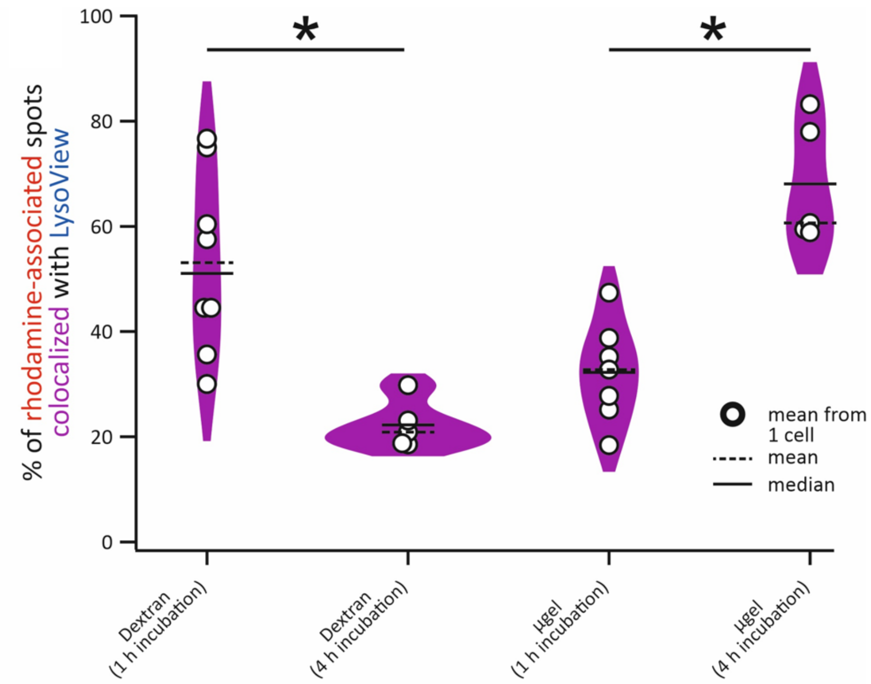

Fig. 5.6 Quantification of microgels/dextran colocalization with lysosomes over time. Violin plots show the percentage of rhodamine-positive spots (to the whole amount) that colocalize with LysoView488-positive compartments after 1 hour or 4 hours of incubation. Each data point represents a single cell (n>6 per condition). Horizontal lines within violins indicate mean values (dashed) and median (solid). Asterisks denote statistically significant differences ($p < 0.05$) between conditions.

5.3.4 Membrane Tension Dynamics During Microgel Uptake

The investigation of membrane tension changes using Flipper probe technology and fluorescence lifetime imaging microscopy (FLIM) presented significant technical challenges [158]. Initial experiments revealed that Flipper probes require highly specific laser conditions for accurate FLIM measurements. Deviation from optimal illumination parameters resulted in rapid cell death, necessitating extensive optimization of the imaging setup. That could be overcome by balancing excitation power and frequency of pulse laser to achieve sufficient signal-to-noise ratio for lifetime measurements while avoiding photodamage.

Following systematic optimization of the experimental conditions, we were able to perform stable FLIM measurements on live HEK293T cells during microgel exposure. However, the results did not reveal statistically significant changes in membrane tension during the microgel uptake process. The fluorescence lifetime of Flipper probes remained constant within experimental error throughout the observation period, suggesting that microgel internalization does not induce detectable alterations in plasma membrane tension.

This finding correlates well with our previous observations that microgels do not accumulate on the plasma membrane surface prior to internalization [132]. The absence of membrane tension changes supports the hypothesis that microgel uptake occurs through rapid internalization mechanisms rather than processes requiring extensive membrane deformation.

5.4 Discussion

The combined results from cytoskeletal analysis, intracellular trafficking studies, and membrane tension measurements provide important insights into the cellular response to PNIPAM microgel uptake and their potential for biomedical applications. The preservation of actin network organization following microgel exposure provides additional evidence supporting the low cytotoxicity of PNIPAM-based microgels. The cytoskeleton is fundamental to numerous cellular processes including cell division, migration, intracellular transport, and mechanotransduction [149]. Disruption of cytoskeletal architecture is a hallmark of many toxic insults and can trigger apoptotic pathways, impair cellular function, and compromise cell viability. The absence of observable actin reorganization or stress fiber disruption in our experiments suggests that microgel internalization does not induce significant mechanical stress or activate cellular stress responses associated with membrane damage or cytoskeletal perturbation.

However, it should be acknowledged that HEK293T cells may not represent the optimal model system for detecting subtle actin-mediated effects. These cells exhibit relatively simple actin architectures compared to highly motile or contractile cell types. Future studies employing cell lines with more prominent and well-defined actin structures (for example, HeLa cells), primary fibroblasts would provide more sensitive assessments of potential cytoskeletal disruption. In contrast to actin, the microtubule network showed measurable changes following microgel uptake, including increased branch level complexity and filament straightness after 4 hours of internalization.

These alterations need careful interpretation. On one hand, the modest nature of these changes suggest that the fundamental organization and functionality of the microtubule network remains intact. The increased branching could reflect an adaptive cellular response to accommodate increased vesicular trafficking demands rather than pathological disruption. On the other hand, given that microtubules serve as the primary highways for long-range intracellular transport—including endosomal and lysosomal trafficking—these structural changes may have functional consequences for cargo distribution and organelle positioning. The progressive accumulation of microgels in lysosomes indicates that microtubule-based transport is indeed actively involved in microgel trafficking. Future studies employing live-cell imaging to track individual microgel-containing endosomes along microtubule networks would provide valuable insights into the dynamics of this process.

The demonstration of progressive lysosomal accumulation (over 75%) has important implications for the rational design of microgel-based drug delivery systems. This trafficking pattern presents both opportunities and challenges depending on the intended therapeutic application.

For applications requiring cytoplasmic drug release, the rapid and extensive lysosomal sequestration represents a significant barrier. The acidic and enzymatically harsh lysosomal environment could prematurely degrade cargo or prevent its release into the cytoplasm [159, 160]. This challenge is particularly relevant for delivery of proteins, peptides, or nucleic acids that require cytosolic access for activity. Future microgel designs should therefore incorporate lysosomal escape mechanisms such as proton sponge effects [161, 162] to facilitate cargo release before complete lysosomal sequestration. Conversely, the predictable lysosomal trafficking could be advantageous for specific applications like delivery of lysosome-targeted therapeutics.

5.5 Conclusions

Taken together, our results demonstrate that PNIPAM microgel uptake does not cause gross disruption of cellular architecture or homeostasis under the examined conditions. The preservation of actin organization and membrane integrity, coupled with only modest microtubule network changes, indicates good biocompatibility at the cytoskeletal level. The predictable lysosomal trafficking pathway provides a foundation for rational microgel design, whether for exploiting lysosomal targeting or engineering escape mechanisms. These findings support the continued development of microgel-based delivery systems while highlighting specific design considerations—particularly regarding lysosomal fate and potential long-term effects on microtubule-dependent processes—that should inform future optimization efforts.

Chapter 6

Future Outlook and Perspectives

The aim of this thesis was to investigate the interfacial behavior of PNIPAM microgels across multiple environments: from solid substrates to biological membranes. As soft and heterogeneous objects, microgels undergo significant deformation during interfacial interactions, making their characterization both challenging and critical for various applications.

The investigation began with atomic force microscopy (AFM) characterization of microgels with diverse architectures adsorbed on solid substrates (Chapter 2). Experiments with hollow microgels revealed their extreme softness due to the internal cavity. Also, these studies demonstrated that sample preparation methods critically affect the final microgel morphology. Spin-coating led to extreme flattening and potential disruption of the polymer network, while the gentler drop-casting method preserved more native structural features. Studies of anisotropic hollow and core-shell microgels confirmed that synthesis history creates persistent mechanical heterogeneity. The templating process results in higher polymer density at rod edges compared to central regions, fundamentally affecting the mechanical landscape of these particles. Additionally, AFM characterization of capillary self-assembly revealed that transfer from the air-water interface to solid substrates can reorganize particle arrangements, challenging the assumption that dip-coating faithfully preserves interfacial structures. This observation warrants careful consideration in future studies of interfacial assembly.

The obtained results demonstrate that AFM is a useful tool capable of characterizing microgels with diverse architectures and shapes. Beyond the types of microgels studied here, AFM could be implemented to investigate more complex geometries and architectures. The technique's ability to map three-dimensional stiffness distributions makes it particularly valuable for studying heterogeneous structures and understanding how mechanical properties relate to both adsorption behavior and cellular interactions.

Chapter 3 examined the contact mechanics of microgel adsorption more quantitatively. Measurements on microfluidic-synthesized microgels demonstrated that reducing adhesion energy decreases both deformation and contact radius, following predictions from Johnson-Kendall-Roberts theory. However, comprehensive validation of this model across wider parameter ranges remains an important future direction. Systematic studies varying cross-linking density, surface chemistry, and adhesion energy would establish whether standard models adequately describe the behavior of these heterogeneous polymer networks or if modifications are needed to account for their internal structure.

Supported lipid bilayers (SLBs) were introduced as biomimetic surfaces for microgel adsorption studies. However, this surface encountered challenges due to electrostatic repulsion between anionic microgels and negatively charged lipids. Future work should address this limitation by incorporating cationic lipids or creating mixed lipid compositions that enable stable microgel adsorption while maintaining membrane-like properties. Such surfaces could simulate interactions with cell membranes more accurately than the PAH-functionalized glass substrates used in Chapter 4. Investigating microgel behavior on SLBs with varying lipid compositions, including functional lipids like cholesterol or sphingomyelin, would provide insights into how membrane properties influence microgel-cell interactions. At the same time, weak interactions between microgels and SLBs could pose experimental challenges for AFM measurements, as particles may detach during scanning.

Chapter 4 established a remarkable connection between AFM-measured mechanical properties and cellular uptake behavior. Despite being measured on glass substrates rather than at cell membranes, AFM-defined softness successfully predicted cellular internalization in HEK293T cells. To address the adhesion limitations observed with SLBs, glass slides functionalized with cationic polyallylamine hydrochloride (PAH) were used, and *in situ* adsorption was employed to minimize deformation artifacts during sample preparation.

The normalized "relative indentation" parameter divided microgels into three distinct groups: fast uptake (highly deformable), intermediate uptake (moderately deformable), and no uptake (rigid). Most remarkably, newly introduced ultra-low cross-linked microgels—despite their large size (>1.8 μm diameter) showed the fastest uptake kinetics (430 seconds median time), demonstrating that softness can overcome traditional size limitations for cellular uptake.

These findings open new directions for rational microgel design. At the same time, the specific endocytotic pathways utilized by different microgel were not the part of this work. Future studies of these mechanisms would enable precise control over cellular entry routes, which could be exploited to optimize cargo delivery and therapeutic efficacy. The cellular experiments in this thesis focused on HEK293T cells and PAH-functionalized glass substrates. Extending these studies to more biologically relevant surfaces and diverse cell types is essential for broader applicability. Also, the ultra-low cross-linked microgels that achieved rapid uptake despite their large size represent an intriguing phenomenon that warrants deeper investigation. Fast internalization and possible ability to be used as a drug cargo make them promising candidates for drug delivery.

However, the cellular implications of particle shape were not explored in this work. Given that anisotropic particles exhibit fundamentally different membrane wrapping dynamics compared to spheres, investigating how rod-shaped microgels interact with cells represents an important future direction. Such studies would reveal whether shape affects uptake efficiency, pathway preference, intracellular trafficking, or therapeutic efficacy.

Chapter 5 extended the investigation to post-internalization effects using S5% microgels as a model system. Analysis of cytoskeletal structures (actin and tubulin networks) and endosomal-lysosomal trafficking revealed that microgel exposure did not cause significant disruption of actin organization, suggesting minimal cytotoxicity. The microtubule network showed small changes in branching complexity and filament straightness, though the functional implications remain unclear. Colocalization studies demonstrated efficient accumulation of microgels in lysosomes (>75% after 4 hours), confirming that internalized microgels follow the canonical endosomal-lysosomal degradation pathway.

In future experiments longer time scales (days to weeks) should be investigated to assess whether observed effects are transient and reversible or they progress into chronic dysfunction. Furthermore, systematic variation of microgel size and chemistry is needed to establish comprehensive structure-activity relationships. While Chapter 4 showed that size and stiffness synergistically affect uptake, the post-internalization consequences of these parameters remain unexplored. Testing multiple types of microgels across diverse cell types would establish whether the biocompatibility observed for S5% microgels in HEK293T cells generalizes to other systems.

Bibliography

[1] Robert Pelton. Temperature-sensitive aqueous microgels. *Advances in colloid and interface science*, 85(1):1–33, 2000.

[2] Yufan Xu, Hongjia Zhu, Akhila Denduluri, Yangteng Ou, Nadia A Erkamp, Runzhang Qi, Yi Shen, and Tuomas PJ Knowles. Recent advances in microgels: from biomolecules to functionality. *Small*, 18(34):2200180, 2022.

[3] Felix A Plamper and Walter Richtering. Functional microgels and microgel systems. *Accounts of chemical research*, 50(2):131–140, 2017.

[4] Mallika Das, Hong Zhang, and Eugenia Kumacheva. Microgels: Old materials with new applications. *Annu. Rev. Mater. Res.*, 36(1):117–142, 2006.

[5] Zhiyong Meng, Michael H Smith, and L Andrew Lyon. Temperature-programmed synthesis of micron-sized multi-responsive microgels. *Colloid and Polymer Science*, 287(3):277–285, 2009.

[6] Matthias Karg, Andrij Pich, Thomas Hellweg, Todd Hoare, L Andrew Lyon, JJ Crassous, Daisuke Suzuki, Rustam A Gumerov, Stefanie Schneider, Igor I Potemkin, et al. Nanogels and microgels: From model colloids to applications, recent developments, and future trends. *Langmuir*, 35(19):6231–6255, 2019.

[7] Karl Kratz, Thomas Hellweg, and Wolfgang Eimer. Structural changes in pnipam microgel particles as seen by sans, dls, and em techniques. *Polymer*, 42(15):6631–6639, 2001.

[8] Imre Varga, Tibor Gilányi, Róbert Mészáros, Genoveva Filipcsei, and Miklós Zrínyi. Effect of cross-link density on the internal structure of poly (n-isopropylacrylamide) microgels. *The Journal of Physical Chemistry B*, 105(38):9071–9076, 2001.

[9] Michael Heskins and James E Guillet. Solution properties of poly (n-isopropylacrylamide). *Journal of Macromolecular Science—Chemistry*, 2(8):1441–1455, 1968.

[10] Markus Stieger, Walter Richtering, Jan Skov Pedersen, and Peter Lindner. Small-angle neutron scattering study of structural changes in temperature sensitive microgel colloids. *The Journal of chemical physics*, 120(13):6197–6206, 2004.

[11] Denise Kleinschmidt, Marta Sofia Fernandes, Matthias Mork, Anna Astrid Meyer, Julian Krischel, Mikhail V Anakhov, Rustam A Gumerov, Igor I Potemkin, Magnus Rueping, and Andrij Pich. Enhanced catalyst performance through compartmentalization exemplified by colloidal l-proline modified microgel catalysts. *Journal of Colloid and Interface Science*, 559:76–87, 2020.

[12] Frédéric Grabowski, Fabian Fink, Walter S Schier, Sven Soerensen, Alexander V Petrunin, Walter Richtering, Sonja Herres-Pawlis, and Andrij Pich. Catalyzed henry reaction by compartmentalized copper-pyrazolyl-complex modified microgels. *Advanced Functional Materials*, 34(40):2403787, 2024.

[13] Qi Feng, Dingguo Li, Qingtao Li, Xiaodong Cao, and Hua Dong. Microgel assembly: Fabrication, characteristics and application in tissue engineering and regenerative medicine. *Bioactive materials*, 9:105–119, 2022.

[14] Dirk Rommel, Matthias Mork, Sitara Vedaraman, Céline Bastard, Luis PB Guerzoni, Yonca Kittel, Rostislav Vinokur, Nikolai Born, Tamás Haraszti, and Laura De Laporte. Functionalized microgel rods interlinked into soft macroporous structures for 3d cell culture. *Advanced Science*, 9(10):2103554, 2022.

[15] Priyanshi Agnihotri, Divya Dheer, Anvi Sangwan, Vysakh C. Chandran, Nimisha A. Mavlankar, Gunjan Hooda, Debabrata Patra, and Asish Pal. Design of multi-responsive and actuating microgels toward on-demand drug release. *Nanoscale*, 16(41):19254–19265, 2024.

[16] Marcus Deloney, Kyra Smart, Blaine A. Christiansen, and Alyssa Panitch. Thermoresponsive, hollow, degradable core-shell nanoparticles for intra-articular delivery of anti-inflammatory peptide. *Journal of Controlled Release*, 323:47–58, July 2020.

[17] Walter Richtering, Irina Alberg, and Rudolf Zentel. Nanoparticles in the Biological Context: Surface Morphology and Protein Corona Formation. *Small*, 16(39):2002162, 2020.

[18] Sarah Boesveld, Yonca Kittel, Yizhao Luo, Alexander Jans, Burak Oezcifci, Matthias Bartneck, Christian Preisinger, Dirk Rommel, Tamás Haraszti, Silvia P. Centeno, Arnold J. Boersma, Laura De Laporte, Christian Trautwein, Alexander J. C. Kuehne, and Pavel Strnad. Microgels as Platforms for Antibody-Mediated Cytokine Scavenging. *Advanced Healthcare Materials*, 12(18):2300695, 2023.

[19] Joanna B Thorne, George J Vine, and Martin J Snowden. Microgel applications and commercial considerations. *Colloid and Polymer Science*, 289(5):625–646, 2011.

[20] Susanne Wiese, Antje C Spiess, and Walter Richtering. Microgel-stabilized smart emulsions for biocatalysis. *Angewandte Chemie*, 125(2), 2013.

[21] Yosuke Horiguchi, Hidetaka Kawakita, Keisuke Ohto, and Shintaro Morisada. Temperature-responsive pickering foams stabilized by poly (n-isopropylacrylamide) nanogels. *Advanced Powder Technology*, 29(2):266–272, 2018.

[22] Stephan Schmidt, Michael Zeiser, Thomas Hellweg, Claus Duschl, Andreas Fery, and Helmuth Möhwald. Adhesion and mechanical properties of pnipam microgel films and their potential use as switchable cell culture substrates. *Advanced Functional Materials*, 20(19):3235–3243, 2010.

[23] IC Barker, JMG Cowie, TN Huckerby, DA Shaw, I Soutar, and L Swanson. Studies of the “smart” thermoresponsive behavior of copolymers of n-isopropylacrylamide and n, n-dimethylacrylamide in dilute aqueous solution. *Macromolecules*, 36(20):7765–7770, 2003.

[24] Shuiqin Zhou and Benjamin Chu. Synthesis and Volume Phase Transition of Poly(methacrylic acid-co-N-isopropylacrylamide) Microgel Particles in Water. *The Journal of Physical Chemistry B*, 102(8):1364–1371, February 1998.

[25] Jérôme J Crassous, Adriana M Mihut, Linda K Månsson, and Peter Schurtenberger. Anisotropic responsive microgels with tuneable shape and interactions. *Nanoscale*, 7(38):15971–15982, 2015.

[26] Hanna JM Wolff, John Linkhorst, Tim Göttlich, Johann Savinsky, Andreas JD Krüger, Laura De Laporte, and Matthias Wessling. Soft temperature-responsive microgels of complex shape in stop-flow lithography. *Lab on a Chip*, 20(2):285–295, 2020.

[27] Frédéric Grabowski, Vladislav S Petrovskii, Fabian Fink, Dan Eugen Demco, Sonja Herres-Pawlis, Igor I Potemkin, and Andrij Pich. Anisotropic microgels by supramolecular assembly and precipitation polymerization of pyrazole-modified monomers. *Advanced Science*, 9(36):2204853, 2022.

[28] Maria I Pieper, Hannah F Mathews, and Andrij Pich. Ionic strength-induced compartmentalization for nanogel-in-microgel colloids. *Small*, 21(9):2410221, 2025.

[29] A Scotti, M Brugnoni, AA Rudov, JE Houston, II Potemkin, and W Richtering. Hollow microgels squeezed in overcrowded environments. *The journal of chemical physics*, 148(17), 2018.

[30] Anne C. Nickel, Andrey A. Rudov, Igor I. Potemkin, Jérôme J. Crassous, and Walter Richtering. Interfacial assembly of anisotropic core–shell and hollow microgels. *Langmuir*, 38(14):4351–4363, 2022.

[31] Anne C Nickel, Timon Kratzenberg, Steffen Bochenek, Maximilian M Schmidt, Andrey A Rudov, Andreas Falkenstein, Igor I Potemkin, Jérôme J Crassous, and Walter Richtering. Anisotropic microgels show their soft side. *Langmuir*, 38(17):5063–5080, 2021.

[32] Wenjing Xu, Andrey Rudov, Alex Oppermann, Sarah Wypysek, Michael Kather, Ricarda Schroeder, Walter Richtering, Igor I Potemkin, Dominik Wöll, and Andrij Pich. Synthesis of polyampholyte janus-like microgels by coacervation of reactive precursors in precipitation polymerization. *Angewandte Chemie*, 132(3):1264–1271, 2020.

[33] Ekaterina Ponomareva, Kirsten Volk, Paul Mulvaney, and Matthias Karg. Surface lattice resonances in self-assembled gold nanoparticle arrays: Impact of lattice period, structural disorder, and refractive index on resonance quality. *Langmuir*, 36(45):13601–13612, 2020.

[34] Sanchita Bhattacharya, Franziska Eckert, Volodymyr Boyko, and Andrij Pich. Temperature-, ph-, and magnetic-field-sensitive hybrid microgels. *Small*, 3(4):650–657, 2007.

[35] R Pelton and T Hoare. Microgel suspensions: Fundamentals and applications. *Fernandez-Nieves, A., Wyss, H., Mattsson, J., Weitz, D., Eds*, 2011.

[36] Andrij Pich and Walter Richtering. Microgels by precipitation polymerization: synthesis, characterization, and functionalization. *Chemical design of responsive microgels*, pages 1–37, 2010.

[37] X Wu, RH Pelton, AE Hamielec, DR Woods, and W McPhee. The kinetics of poly (n-isopropylacrylamide) microgel latex formation. *Colloid and polymer science*, 272(4):467–477, 1994.

[38] Bin Luo, Xiao-Jie Song, Feng Zhang, Ao Xia, Wu-Li Yang, Jian-Hua Hu, and Chang-Chun Wang. Multi-functional thermosensitive composite microspheres with high magnetic susceptibility based on magnetite colloidal nanoparticle clusters. *Langmuir*, 26(3):1674–1679, 2010.

[39] Neetu Singh and L Andrew Lyon. Au nanoparticle templated synthesis of pnipam nanogels. *Chemistry of Materials*, 19(4):719–726, 2007.

[40] Clinton D Jones and L Andrew Lyon. Synthesis and characterization of multiresponsive core- shell microgels. *Macromolecules*, 33(22):8301–8306, 2000.

[41] Satish Nayak, Daoji Gan, Michael J Serpe, and L Andrew Lyon. Hollow thermoresponsive microgels. *Small*, 1(4):416–421, 2005.

[42] Janine Dubbert, Tobias Honold, Jan Skov Pedersen, Aurel Radulescu, Markus Drechsler, Matthias Karg, and Walter Richtering. How hollow are thermoresponsive hollow nanogels? *Macromolecules*, 47(24):8700–8708, 2014.

[43] Chang-Jing Cheng, Liang-Yin Chu, Ping-Wei Ren, Jie Zhang, and Lin Hu. Preparation of monodisperse thermo-sensitive poly (n-isopropylacrylamide) hollow microcapsules. *Journal of colloid and interface science*, 313(2):383–388, 2007.

[44] Jun Gao and Barbara J. Frisken. Cross-Linker-Free N-Isopropylacrylamide Gel Nanospheres. *Langmuir*, 19(13):5212–5216, June 2003.

[45] Jun Gao and Barbara J. Frisken. Influence of Secondary Components on the Synthesis of Self-Cross-Linked N-Isopropylacrylamide Microgels. *Langmuir*, 21(2):545–551, January 2005.

[46] Monia Brugnoni, Anne C. Nickel, Leif C. Kröger, Andrea Scotti, Andrij Pich, Kai Leonhard, and Walter Richtering. Synthesis and structure of deuterated ultra-low cross-linked poly(N-isopropylacrylamide) microgels. *Polymer Chemistry*, 10(19):2397–2405, May 2019.

[47] Jan-Michael Y Carrillo, Elie Raphael, and Andrey V Dobrynin. Adhesion of nanoparticles. *Langmuir*, 26(15):12973–12979, 2010.

[48] Stefan Wellert, Marcel Richter, Thomas Hellweg, Regine von Klitzing, and Yvonne Hertle. Responsive microgels at surfaces and interfaces. *Zeitschrift für physikalische Chemie*, 229(7-8):1225–1250, 2015.

[49] Thomas Salez, Michael Benzaquen, and Élie Raphaël. From adhesion to wetting of a soft particle. *Soft Matter*, 9(45):10699–10704, 2013.

[50] Stephan Schmidt, Thomas Hellweg, and Regine von Klitzing. Packing density control in p (nipam-co-aac) microgel monolayers: effect of surface charge, ph, and preparation technique. *Langmuir*, 24(21):12595–12602, 2008.

[51] Fabrizio Camerin, Miguel Ángel Fernández-Rodríguez, Lorenzo Rovigatti, Maria-Nefeli Antonopoulou, Nicoletta Gnan, Andrea Ninarello, Lucio Isa, and Emanuela Zaccarelli. Microgels adsorbed at liquid–liquid interfaces: A joint numerical and experimental study. *ACS nano*, 13(4):4548–4559, 2019.

[52] Steffen Bochenek, Andrea Scotti, Wojciech Ogieglo, Miguel Ángel Fernández-Rodríguez, M Friederike Schulte, Rustam A Gumerov, Nikita V Bushuev, Igor I Potemkin, Matthias Wessling, Lucio Isa, et al. Effect of the 3d swelling of microgels on their 2d phase behavior at the liquid–liquid interface. *Langmuir*, 35(51):16780–16792, 2019.

[53] Stephan Schmidt, Hubert Motschmann, Thomas Hellweg, and Regine von Klitzing. Thermoresponsive surfaces by spin-coating of pnipam-co-paa microgels: A combined afm and ellipsometry study. *Polymer*, 49(3):749–756, 2008.

[54] Anna Burmistrova and Regine von Klitzing. Control of number density and swelling/shrinking behavior of p (nipam–aac) particles at solid surfaces. *Journal of Materials Chemistry*, 20(17):3502–3507, 2010.

[55] M Friederike Schulte, Andrea Scotti, Monia Brugnoni, Steffen Bochenek, Ahmed Mourran, and Walter Richtering. Tuning the structure and properties of ultra-low cross-linked temperature-sensitive microgels at interfaces via the adsorption pathway. *Langmuir*, 35(46):14769–14781, 2019.

[56] Haylee Bachman, Ashley C Brown, Kimberly C Clarke, Kabir S Dhada, Alison Douglas, Caroline E Hansen, Emily Herman, John S Hyatt, Purva Kodlekere, Zhiyong Meng, et al. Ultrasoft, highly deformable microgels. *Soft matter*, 11(10):2018–2028, 2015.

[57] Gerd Binnig, Calvin F Quate, and Ch Gerber. Atomic force microscope. *Physical review letters*, 56(9):930, 1986.

[58] G Binnig, Ch Gerber, E_ Stoll, TR Albrecht, and CF Quate. Atomic resolution with atomic force microscope. *Europhysics Letters*, 3(12):1281, 1987.

[59] Andrew J Fleming. A review of nanometer resolution position sensors: Operation and performance. *Sensors and Actuators A: Physical*, 190:106–126, 2013.

[60] Stephen A Joyce and JE Houston. A new force sensor incorporating force-feedback control for interfacial force microscopy. *Review of Scientific Instruments*, 62(3):710–715, 1991.

[61] Yang Li and John Bechhoefer. Feedforward control of a closed-loop piezoelectric translation stage for atomic force microscope. *Review of Scientific Instruments*, 78(1), 2007.

[62] Gerhard Meyer and Nabil M Amer. Novel optical approach to atomic force microscopy. *Applied physics letters*, 53(12):1045–1047, 1988.

[63] Jozef Adamcik, Alexandre Berquand, and Raffaele Mezzenga. Single-step direct measurement of amyloid fibrils stiffness by peak force quantitative nanomechanical atomic force microscopy. *Applied Physics Letters*, 98(19), 2011.

[64] Hans-Jürgen Butt, Brunero Cappella, and Michael Kappl. Force measurements with the atomic force microscope: Technique, interpretation and applications. *Surface science reports*, 59(1-6):1–152, 2005.

[65] Rudolf Merkel, Pierre Nassoy, Andrew Leung, Ken Ritchie, and Evan Evans. Energy landscapes of receptor–ligand bonds explored with dynamic force spectroscopy. *Nature*, 397(6714):50–53, 1999.

[66] Brunero Cappella and Giovanni Dietler. Force-distance curves by atomic force microscopy. *Surface science reports*, 34(1-3):1–104, 1999.

[67] T Junno, S Anand, K Deppert, L Montelius, and L Samuelson. Contact mode atomic force microscopy imaging of nanometer-sized particles. *Applied physics letters*, 66(24):3295–3297, 1995.

[68] Bertram Schleicher, Thomas Jung, and Heinz Burtscher. Characterization of ultrafine aerosol particles adsorbed on highly oriented pyrolytic graphite by scanning tunneling and atomic force microscopy. *Journal of colloid and interface science*, 161(2):271–277, 1993.

[69] Yves Martin, Clayton C Williams, and H Kumar Wickramasinghe. Atomic force microscope–force mapping and profiling on a sub 100-å scale. *Journal of applied Physics*, 61(10):4723–4729, 1987.

[70] Thomas R Albrecht, Peter Grütter, David Horne, and Daniel Rugar. Frequency modulation detection using high-q cantilevers for enhanced force microscope sensitivity. *Journal of applied physics*, 69(2):668–673, 1991.

[71] Ricardo Garcıa and Ruben Perez. Dynamic atomic force microscopy methods. *Surface science reports*, 47(6-8):197–301, 2002.

[72] SN Magonov, V Elings, and M-H Whangbo. Phase imaging and stiffness in tapping-mode atomic force microscopy. *Surface science*, 375(2-3):L385–L391, 1997.

[73] Bede Pittenger, Natalia Erina, and Chanmin Su. Quantitative mechanical property mapping at the nanoscale with peakforce qnm. *Bruker application note AN128, Rev. A*, 128:1–12, 2010.

[74] Galja Pletikapić, Alexandre Berquand, Tea Mišić Radić, and Vesna Svetličić. Quantitative nanomechanical mapping of marine diatom in seawater using peak force tapping atomic force microscopy 1. *Journal of phycology*, 48(1):174–185, 2012.

[75] Joseph R Lakowicz. *Principles of fluorescence spectroscopy*. Springer, 2006.

[76] Marvin Minsky. Memoir on inventing the confocal scanning microscope. 1988.

[77] Vineeta Rai and Nrisingha Dey. The basics of confocal microscopy. *Laser scanning, theory and applications*, pages 75–96, 2011.

[78] Michael C Adams, Wendy C Salmon, Stephanie L Gupton, Christopher S Cohan, Torsten Wittmann, Natalie Prigozhina, and Clare M Waterman-Storer. A high-speed multispectral spinning-disk confocal microscope system for fluorescent speckle microscopy of living cells. *Methods*, 29(1):29–41, 2003.

[79] Stefan W Hell. Far-field optical nanoscopy. *science*, 316(5828):1153–1158, 2007.

[80] Volker Westphal and Stefan W Hell. Nanoscale resolution in the focal plane of an optical microscope. *Physical review letters*, 94(14):143903, 2005.

[81] Andrea Scotti, Urs Gasser, Alexander V. Petrunin, Lisa Fruhner, Walter Richtering, and Judith E. Houston. Experimental determination of the bulk moduli of hollow nanogels. *Soft Matter*, 18:5750–5758, 2022.

[82] ZH Farooqi, SR Khan, and R Begum. Temperature-responsive hybrid microgels for catalytic applications: a review. *Materials Science and Technology*, 33(2):129–137, 2017.

[83] Yang Wang, Jin Zheng, Yefei Tian, and Wuli Yang. Acid degradable poly (vinylcaprolactam)-based nanogels with ketal linkages for drug delivery. *Journal of Materials Chemistry B*, 3(28):5824–5832, 2015.

[84] Maxim Dirksen, Carina Dargel, Lukas Meier, Timo Brändel, and Thomas Hellweg. Smart microgels as drug delivery vehicles for the natural drug aescin: Uptake, release and interactions. *Colloid and Polymer Science*, 298(6):505–518, 2020.

[85] Janine Dubbert, Tobias Honold, Jan Skov Pedersen, Aurel Radulescu, Markus Drechsler, Matthias Karg, and Walter Richtering. How hollow are thermoresponsive hollow nanogels? *Macromolecules*, 47(24):8700–8708, 2014.

[86] LS Zha, Yan Zhang, WL Yang, and SK Fu. Monodisperse temperature-sensitive microcontainers. *Advanced Materials*, 14(15):1090–1092, 2002.

[87] Sarah K Wypysek, Silvia P Centeno, Till Gronemann, Dominik Wöll, and Walter Richtering. Hollow, ph-sensitive microgels as nanocontainers for the encapsulation of proteins. *Macromolecular Bioscience*, 23(8):2200456, 2023.

[88] Jean-Christophe Loudet, Arjun G Yodh, and Bernard Pouligny. Wetting and contact lines of micrometer-sized ellipsoids. *Physical review letters*, 97(1):018304, 2006.

[89] H Lehle, E Noruzifar, and M Oettel. Ellipsoidal particles at fluid interfaces. *The European Physical Journal E*, 26(1):151–160, 2008.

[90] Ramsia Geisler, Mohammad A. Hormozi, and Regine von Klitzing. Unveiling the nanoscale world: Exploring surface tension measurements with atomic force nanoindenters. *Current Opinion in Colloid & Interface Science*, 69:101769, February 2024.

[91] Anders Aufderhorst-Roberts, Daniel Baker, Richard J. Foster, Olivier Cayre, Johan Mattsson, and Simon D. Connell. Nanoscale mechanics of microgel particles. *Nanoscale*, 10(34):16050–16061, August 2018.

[92] Yuke Liu, Igor Sokolov, Maxim E. Dokukin, Yongqiang Xiong, and Ping'an Peng. Can AFM be used to measure absolute values of Young's modulus of nanocomposite materials down to the nanoscale? *Nanoscale*, 12(23):12432–12443, 2020.

[93] Sebastian Backes and Regine Von Klitzing. Nanomechanics and Nanorheology of Microgels at Interfaces. *Polymers*, 10(9):978, September 2018.

[94] M Friederike Schulte, Andrea Scotti, Arjan PH Gelissen, Walter Richtering, and Ahmed Mourran. Probing the internal heterogeneity of responsive microgels adsorbed to an interface by a sharp sfm tip: Comparing core–shell and hollow microgels. *Langmuir*, 34(14):4150–4158, 2018.

[95] Jérôme J Crassous, Adriana M Mihut, Erik Wernersson, Patrick Pfleiderer, Jan Vermant, Per Linse, and Peter Schurtenberger. Field-induced assembly of colloidal ellipsoids into well-defined microtubules. *Nature communications*, 5(1):5516, 2014.

[96] Nabanita Hazra, Janik Lammertz, Andrey Babenyshev, Rebecca Erkes, Fabian Hagemans, Chandeshwar Misra, Walter Richtering, and Jérôme J Crassous. Charged hollow microgel capsules. *Soft Matter*, 20(23):4608–4620, 2024.

[97] Fabian Hagemans, Nabanita Hazra, Viktoria D Lovasz, Alexander J Awad, Martin Frenken, Andrey Babenyshev, Olli-Ville Laukkanen, Dominik Braunmiller, Walter Richtering, and Jérôme J Crassous. Soft and deformable thermoresponsive hollow

rod-shaped microgels. *Small*, 21(1):2401376, 2025.

[98] Peter A. Kralchevsky and Kuniaki Nagayama. Capillary interactions between particles bound to interfaces, liquid films and biomembranes. *Adv. Colloid Interface Sci.*, 85(2):145–192, 2000.

[99] M. Friederike Schulte, Steffen Bochenek, Monia Brugnoni, Andrea Scotti, Ahmed Mourran, and Walter Richtering. Stiffness Tomography of Ultra-Soft Nanogels by Atomic Force Microscopy. *Angewandte Chemie International Edition*, 60(5):2280–2287, 2021.

[100] K. L. Johnson, K. Kendall, and A. D. Roberts. Surface energy and the contact of elastic solids. *Proceedings of the Royal Society of London. A. Mathematical and Physical Sciences*, 324(1558):301–313, September 1971.

[101] Boris V Derjaguin, Vladimir M Muller, and Yu P Toporov. Effect of contact deformations on the adhesion of particles. *Journal of Colloid and interface science*, 53(2):314–326, 1975.

[102] Daniel Maugis. *Contact, adhesion and rupture of elastic solids*, volume 130. Springer Science & Business Media, 2000.

[103] Hanqing Wang, Fawad Jacobi, Johannes Waschke, Laura Hartmann, Hartmut Löwen, and Stephan Schmidt. Elastic modulus dependence on the specific adhesion of hydrogels. *Advanced Functional Materials*, 27(41):1702040, 2017.

[104] Laura Hoppe Alvarez, Sabine Eisold, Rustam A Gumerov, Martin Strauch, Andrey A Rudov, Pia Lenssen, Dorit Merhof, Igor I Potemkin, Ulrich Simon, and Dominik Wöll. Deformation of microgels at solid–liquid interfaces visualized in three-dimension. *Nano letters*, 19(12):8862–8867, 2019.

[105] Valentina Nigro, Roberta Angelini, Elena Buratti, Claudia Colantonio, Rosaria D'Amato, Franco Dinelli, Silvia Franco, Francesca Limosani, Rosa Maria Montereali, Enrico Nichelatti, et al. Influence of a solid surface on pnipam microgel films. *Gels*, 10(7):473, 2024.

[106] Fany Di Lorenzo and Sebastian Seiffert. Effect of droplet size in acrylamide-based microgel formation by microfluidics. *Macromolecular Reaction Engineering*, 10(3):201–205, 2016.

[107] Beatrice Ramm, Philipp Glock, and Petra Schwille. In vitro reconstitution of self-organizing protein patterns on supported lipid bilayers. *Journal of Visualized Experiments: JoVE*, (137):58139, 2018.

[108] C Bonnet-Gonnet, L Belloni, and B Cabane. Osmotic pressure of latex dispersions. *Langmuir*, 10(11):4012–4021, 1994.

[109] Sean A. Dilliard and Daniel J. Siegwart. Passive, active and endogenous organ-targeted lipid and polymer nanoparticles for delivery of genetic drugs. *Nature Reviews Materials*, 8(4):282–300, April 2023.

[110] Matthias Karg, Andrij Pich, Thomas Hellweg, Todd Hoare, L. Andrew Lyon, J. J. Crassous, Daisuke Suzuki, Rustam A. Gumerov, Stefanie Schneider, Igor. I. Potemkin, and Walter Richtering. Nanogels and Microgels: From Model Colloids to Applications, Recent Developments, and Future Trends. *Langmuir*, 35(19):6231–6255, May 2019.

[111] Garima Agrawal and Rahul Agrawal. Functional Microgels: Recent Advances in Their Biomedical Applications. *Small*, 14(39):1801724, 2018.

[112] Katja Obst, Guy Yealland, Benjamin Balzus, Enrico Miceli, Mathias Dimde, Christoph Weise, Murat Eravci, Roland Bodmeier, Rainer Haag, Marcelo Calderón, Nada Charbaji, and Sarah Hedtrich. Protein Corona Formation on Colloidal Polymeric Nanoparticles and Polymeric Nanogels: Impact on Cellular Uptake, Toxicity,

Immunogenicity, and Drug Release Properties. *Biomacromolecules*, 18(6):1762–1771, June 2017.

[113] Sulin Zhang, Huajian Gao, and Gang Bao. Physical Principles of Nanoparticle Cellular Endocytosis. *ACS Nano*, 9(9):8655–8671, September 2015.

[114] Mauro Sousa de Almeida, Eva Susnik, Barbara Drasler, Patricia Taladriz-Blanco, Alke Petri-Fink, and Barbara Rothen-Rutishauser. Understanding nanoparticle endocytosis to improve targeting strategies in nanomedicine. *Chemical Society Reviews*, 50(9):5397–5434, May 2021.

[115] Stefan Wilhelm, Anthony J. Tavares, Qin Dai, Seiichi Ohta, Julie Audet, Harold F. Dvorak, and Warren C. W. Chan. Analysis of nanoparticle delivery to tumours. *Nature Reviews Materials*, 1(5):1–12, April 2016.

[116] Fang Lu, Si-Han Wu, Yann Hung, and Chung-Yuan Mou. Size Effect on Cell Uptake in Well-Suspended, Uniform Mesoporous Silica Nanoparticles. *Small*, 5(12):1408–1413, 2009.

[117] Joanna Rejman, Volker Oberle, Inge S. Zuhorn, and Dick Hoekstra. Size-dependent internalization of particles via the pathways of clathrin- and caveolae-mediated endocytosis. *Biochemical Journal*, 377(1):159–169, January 2004.

[118] Ting Wang, Lu Wang, Xiaoming Li, Xingjie Hu, Yuping Han, Yao Luo, Zejun Wang, Qian Li, Ali Aldalbahi, Lihua Wang, Shiping Song, Chunhai Fan, Yun Zhao, Maolin Wang, and Nan Chen. Size-Dependent Regulation of Intracellular Trafficking of Polystyrene Nanoparticle-Based Drug-Delivery Systems. *ACS Applied Materials & Interfaces*, 9(22):18619–18625, June 2017.

[119] Tatsiana Mironava, Michael Hadjiargyrou, Marcia Simon, Vladimir Jurukovski, and Miriam H. Rafailovich. Gold nanoparticles cellular toxicity and recovery: Effect of size, concentration and exposure time. *Nanotoxicology*, March 2010.

[120] Ling Li, Wen-Song Xi, Qianqian Su, Yang Li, Gui-Hua Yan, Yuanfang Liu, Haifang Wang, and Aoneng Cao. Unexpected Size Effect: The Interplay between Different-Sized Nanoparticles in Their Cellular Uptake. *Small*, 15(38):1901687, 2019.

[121] Pratik Gurnani, Carlos Sanchez-Cano, Helena Xandri-Monje, Junliang Zhang, Sean H. Ellacott, Edward D. H. Mansfield, Matthias Hartlieb, Robert Dallmann, and Sébastien Perrier. Probing the Effect of Rigidity on the Cellular Uptake of Core-Shell Nanoparticles: Stiffness Effects are Size Dependent. *Small*, 18(38):2203070, 2022.

[122] Yue Hui, Xin Yi, David Wibowo, Guangze Yang, Anton P. J. Middelberg, Huajian Gao, and Chun-Xia Zhao. Nanoparticle elasticity regulates phagocytosis and cancer cell uptake. *Science Advances*, 6(16):eaaz4316, April 2020.

[123] Xuebin Ma, Xuncheng Yang, Mengqi Li, Jiwei Cui, Peiyu Zhang, Qun Yu, and Jingcheng Hao. Effect of Elasticity of Silica Capsules on Cellular Uptake. *Langmuir*, 37(40):11688–11694, October 2021.

[124] Metin Yildirim, Agnes-Valencia Weiss, and Marc Schneider. The Effect of Elasticity of Gelatin Nanoparticles on the Interaction with Macrophages. *Pharmaceutics*, 15(1):199, January 2023.

[125] Xin Yi, Xinghua Shi, and Huajian Gao. Cellular Uptake of Elastic Nanoparticles. *Physical Review Letters*, 107(9):098101, August 2011.

[126] Ye Li, Xianren Zhang, and Dapeng Cao. Nanoparticle hardness controls the internalization pathway for drug delivery. *Nanoscale*, 7(6):2758–2769, 2015.

[127] Jacob W. Myerson, Bruce Braender, Olivia Mcpherson, Patrick M. Glassman, Raisa Y. Kiseleva, Vladimir V. Shuvaev, Oscar Marcos-Contreras, Martha E. Grady, Hyun-Su Lee, Colin F. Greineder, Radu V. Stan, Russell J. Composto, David M.

Eckmann, and Vladimir R. Muzykantov. Flexible Nanoparticles Reach Sterically Obscured Endothelial Targets Inaccessible to Rigid Nanoparticles. *Advanced Materials*, 30(32):1802373, 2018.

[128] Azzah M Bannunah, Driton Vllasaliu, Jennie Lord, and Snjezana Stolnik. Mechanisms of nanoparticle internalization and transport across an intestinal epithelial cell model: effect of size and surface charge. *Molecular pharmaceutics*, 11(12):4363–4373, 2014.

[129] Vu Thanh Cong, Jacinta L. Houng, Maria Kavallaris, Xin Chen, Richard D. Tilley, and J. Justin Gooding. How can we use the endocytosis pathways to design nanoparticle drug-delivery vehicles to target cancer cells over healthy cells? *Chemical Society Reviews*, 51(17):7531–7559, August 2022.

[130] Andrea Scotti, M. Friederike Schulte, Carlos G. Lopez, Jérôme J. Crassous, Steffen Bochenek, and Walter Richtering. How Softness Matters in Soft Nanogels and Nanogel Assemblies. *Chemical Reviews*, 122(13):11675–11700, July 2022.

[131] Xavier Banquy, Fernando Suarez, Anteneh Argaw, Jean-Michel Rabanel, Peter Grutter, Jean-François Bouchard, Patrice Hildgen, and Suzanne Giasson. Effect of mechanical properties of hydrogel nanoparticles on macrophage cell uptake. *Soft Matter*, 5(20):3984–3991, October 2009.

[132] Victoria K. Switacz, Sarah K. Wypysek, Rudolf Degen, Jérôme J. Crassous, Marc Spehr, and Walter Richtering. Influence of Size and Cross-Linking Density of Microgels on Cellular Uptake and Uptake Kinetics. *Biomacromolecules*, 21(11):4532–4544, November 2020.

[133] M. Friederike Schulte, Andrea Scotti, Monia Brugnoni, Steffen Bochenek, Ahmed Mourran, and Walter Richtering. Tuning the Structure and Properties of Ultra-Low Cross-Linked Temperature-Sensitive Microgels at Interfaces via the Adsorption Pathway. *Langmuir*, 35(46):14769–14781, November 2019.

[134] Ashley C. Brown, Sarah E. Stabenfeldt, Byungwook Ahn, Riley T. Hannan, Kabir S. Dhada, Emily S. Herman, Victoria Stefanelli, Nina Guzzetta, Alexander Alexeev, Wilbur A. Lam, L. Andrew Lyon, and Thomas H. Barker. Ultrasoft microgels displaying emergent platelet-like behaviours. *Nature Materials*, 13(12):1108–1114, December 2014.

[135] Kimberly Nellenbach, Emily Mihalko, Seema Nandi, Drew W. Koch, Jagathpala Shetty, Leandro Moretti, Jennifer Sollinger, Nina Moiseiwitsch, Ana Sheridan, Sanika Pandit, Maureane Hoffman, Lauren V. Schnabel, L. Andrew Lyon, Thomas H. Barker, and Ashley C. Brown. Ultrasoft platelet-like particles stop bleeding in rodent and porcine models of trauma. *Science Translational Medicine*, 16(742):eadi4490, April 2024.

[136] M. Friederike Schulte, Emilia Izak-Nau, Susanne Braun, Andrij Pich, Walter Richtering, and Robert Göstl. Microgels react to force: Mechanical properties, syntheses, and force-activated functions. *Chemical Society Reviews*, 51(8):2939–2956, 2022.

[137] W. Burchard and W. Richtering. Dynamic light scattering from polymer solutions. In M. Pietralla and W. Pechhold, editors, *Relaxation in Polymers*, pages 151–163, Darmstadt, 1989. Steinkopff.

[138] O. L. J. Virtanen, A. Mourran, P. T. Pinard, and W. Richtering. Persulfate initiated ultra-low cross-linked poly(N-isopropylacrylamide) microgels possess an unusual inverted cross-linking structure. *Soft Matter*, 12(17):3919–3928, April 2016.

[139] Otto Virtanen. Ovirtanen/fitit, October 2022.

[140] Andrea Scotti, Steffen Bochenek, Monia Brugnoni, Miguel-Angel Fernandez-Rodriguez, Marie F Schulte, JE Houston, Arjan PH Gelissen, Igor I Potemkin, Lucio Isa, and Walter Richtering. Exploring the colloid-to-polymer transition for

ultra-low crosslinked microgels from three to two dimensions. *Nature communications*, 10(1):1418, 2019.

[141] Joshua J. Rennick, Angus P. R. Johnston, and Robert G. Parton. Key principles and methods for studying the endocytosis of biological and nanoparticle therapeutics. *Nature Nanotechnology*, 16(3):266–276, March 2021.

[142] Haylee Bachman, Ashley C. Brown, Kimberly C. Clarke, Kabir S. Dhada, Alison Douglas, Caroline E. Hansen, Emily Herman, John S. Hyatt, Purva Kodlekere, Zhiyong Meng, Shalini Saxena, Mark W. Spears Jr, Nicole Welsch, and L. Andrew Lyon. Ultrasoft, highly deformable microgels. *Soft Matter*, 11(10):2018–2028, 2015.

[143] Irene Canton and Giuseppe Battaglia. Endocytosis at the nanoscale. *Chemical Society Reviews*, 41(7):2718–2739, March 2012.

[144] Guillem Lambies, Szu-Wei Lee, Karen Duong-Polk, Pedro Aza-Blanc, Swetha Maganti, Cheska M. Galapate, Anagha Deshpande, Aniruddha J. Deshpande, David A. Scott, David W. Dawson, and Cosimo Commisso. Cell polarity proteins promote macropinocytosis in response to metabolic stress. *Nature Communications*, 15(1):10541, December 2024.

[145] Yue Hui, David Wibowo, Yun Liu, Rui Ran, Hao-Fei Wang, Arjun Seth, Anton P. J. Middelberg, and Chun-Xia Zhao. Understanding the Effects of Nanocapsular Mechanical Property on Passive and Active Tumor Targeting. *ACS Nano*, 12(3):2846–2857, March 2018.

[146] Aaron C. Anselmo, Mengwen Zhang, Sunny Kumar, Douglas R. Vogus, Stefano Menegatti, Matthew E. Helgeson, and Samir Mitragotri. Elasticity of Nanoparticles Influences Their Blood Circulation, Phagocytosis, Endocytosis, and Targeting. *ACS Nano*, 9(3):3169–3177, March 2015.

[147] Xiangyu Chen, Shuwei Zhang, Jinming Li, Xiaobin Huang, Haochen Ye, Xuezhi Qiao, Zhenjie Xue, Wensheng Yang, and Tie Wang. Influence of Elasticity of Hydrogel Nanoparticles on Their Tumor Delivery. *Advanced Science*, 9(29):2202644, 2022.

[148] Pratap C Naha, Kunal Bhattacharya, Tiziana Tenuta, Kenneth A Dawson, Iseult Lynch, Amaya Gracia, Fiona M Lyng, and Hugh J Byrne. Intracellular localisation, geno-and cytotoxic response of polyn-isopropylacrylamide (pnipam) nanoparticles to human keratinocyte (hacat) and colon cells (sw 480). *Toxicology letters*, 198(2):134–143, 2010.

[149] Daniel A Fletcher and R Dyche Mullins. Cell mechanics and the cytoskeleton. *Nature*, 463(7280):485–492, 2010.

[150] Honglei Jia, Sisi Chen, Xiaofeng Wang, Cong Shi, Kena Liu, Shuangxi Zhang, and Jisheng Li. Copper oxide nanoparticles alter cellular morphology via disturbing the actin cytoskeleton dynamics in arabidopsis roots. *Nanotoxicology*, 14(1):127–144, 2020.

[151] Yue Wu, Moustafa RK Ali, Bin Dong, Tiegang Han, Kuangcai Chen, Jin Chen, Yan Tang, Ning Fang, Fangjun Wang, and Mostafa A El-Sayed. Gold nanorod photothermal therapy alters cell junctions and actin network in inhibiting cancer cell collective migration. *ACS nano*, 12(9):9279–9290, 2018.

[152] Xianghui Zeng, Yuning Zhang, and Andreas M Nystrom. Endocytic uptake and intracellular trafficking of bis-mpa-based hyperbranched copolymer micelles in breast cancer cells. *Biomacromolecules*, 13(11):3814–3822, 2012.

[153] Grace Y Liu, Shiau-Chi Chen, Gang-Hui Lee, Kritika Shaiv, Pin-Yu Chen, Hsuan Cheng, Shi-Rong Hong, Wen-Ting Yang, Shih-Han Huang, Ya-Chu Chang, et al. Precise control of microtubule disassembly in living cells. *The EMBO journal*,

41(15):e110472, 2022.

[154] Magalie Bénard, Christophe Chamot, Damien Schapman, Alexis Lebon, and Ludovic Galas. Combined flim, confocal microscopy, and sted nanoscopy for live-cell imaging. *Bio-protocol*, 15(4):e5202, 2025.

[155] Adai Colom, Emmanuel Derivery, Saeideh Soleimanpour, Caterina Tomba, Marta Dal Molin, Naomi Sakai, Marcos González-Gaitán, Stefan Matile, and Aurélien Roux. A fluorescent membrane tension probe. *Nature chemistry*, 10(11):1118–1125, 2018.

[156] Marko Kaksonen and Aurélien Roux. Mechanisms of clathrin-mediated endocytosis. *Nature reviews Molecular cell biology*, 19(5):313–326, 2018.

[157] Lei Li, Tao Wan, Min Wan, Bei Liu, Ran Cheng, and Rongying Zhang. The effect of the size of fluorescent dextran on its endocytic pathway. *Cell biology international*, 39(5):531–539, 2015.

[158] Chloé Roffay, Juan Manuel García-Arcos, Pierrik Chapuis, Javier López-Andarias, Falk Schneider, Adai Colom, Caterina Tomba, Ilaria Di Meglio, Katia Barrett, Valentin Dunsing, et al. Tutorial: fluorescence lifetime microscopy of membrane mechanosensitive flipper probes. *Nature Protocols*, 19(12):3457–3469, 2024.

[159] John B Lloyd. Lysosome membrane permeability: implications for drug delivery. *Advanced drug delivery reviews*, 41(2):189–200, 2000.

[160] Chong Qiu, Fei Xia, Junzhe Zhang, Qiaoli Shi, Yuqing Meng, Chen Wang, Huanhuan Pang, Liwei Gu, Chengchao Xu, Qiuyan Guo, et al. Advanced strategies for overcoming endosomal/lysosomal barrier in nanodrug delivery. *Research*, 6:0148, 2023.

[161] Taoran Tian, Tao Zhang, Tengfei Zhou, Shiyu Lin, Sirong Shi, and Yunfeng Lin. Synthesis of an ethyleneimine/tetrahedral dna nanostructure complex and its potential application as a multi-functional delivery vehicle. *Nanoscale*, 9(46):18402–18412, 2017.

[162] Le Liang, Jiang Li, Qian Li, Qing Huang, Jiye Shi, Hao Yan, and Chunhai Fan. Single-particle tracking and modulation of cell entry pathways of a tetrahedral dna nanostructure in live cells. *Angewandte Chemie International Edition*, 53(30):7745–7750, 2014.

List of Figures

List of Tables